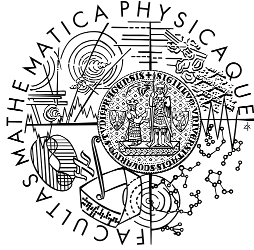

FACULTY
OF MATHEMATICS
AND PHYSICS
Charles University

DOCTORAL THESIS

Jindřich Pipek

Charge transport in semiconductors

Institute of Physics of Charles University

Supervisor of the doctoral thesis: doc. Ing. Eduard Belas, CSc.
Study programme: Quantum optics and Optoelectronics

Prague 2023

I declare that I carried out this doctoral thesis independently, and only with the cited sources, literature and other professional sources. It has not been used to obtain another or the same degree.

I understand that my work relates to the rights and obligations under the Act No. 121/2000 Sb., the Copyright Act, as amended, in particular the fact that the Charles University has the right to conclude a license agreement on the use of this work as a school work pursuant to Section 60 subsection 1 of the Copyright Act.

In Prague, date ....

Author's signature

First, I would like to thank my supervisor, Eduard Belas, for his guidance and help during my study. I am also grateful to Roman Grill for many inspiring discussions and ideas. I would also like to thank Petr Praus for his help with the experimental setup and Marián Betušiak for his help with measurements. I want to thank all members of the Department of Optoelectronics and Magneto-optics for friendly and motivating working environment. Immense gratitude belongs to my parents for their help and encouragement in everything I do.

Title: Charge transport in semiconductors

Author: Jindřich Pipek

Institute: Institute of Physics of Charles University

Supervisor: doc. Ing. Eduard Belas, CSc., Institute of Physics of Charles University

Abstract: This thesis is focused on the study of charge transport in semiconductors. Monte Carlo simulation is combined with the numerical solution of the coupled drift-diffusion equation with Poisson's equation. These numerical simulations of charge transport are applied to experimental data to obtain charge transport parameters of the detector, such as electric field profile, space charge density, defect level energy, capture cross section and concentration, charge carrier drift mobility and diffusion coefficient, and other parameters. Semiconductor samples prepared from semi-insulating GaAs, CdZnTe, and CdZnTeSe single crystals are studied using electrical, spectroscopic, and optical characterization techniques.

Keywords: GaAs, CdZnTe, CdZnTeSe, transient-current technique, electric field, charge transport,

Contents

1 Introduction 3
1.1 Motivation . . . 3
1.2 Studied semiconductors . . . 5
1.2.1 GaAs . . . 5
1.2.2 CdTe, CdZnTe, CdZnTeSe . . . 5
1.3 Crystallographic defects and energy levels . . . 7
1.3.1 Point defects . . . 8
1.3.2 Doping . . . 9
1.4 Ionizing radiation . . . 10
1.5 The goal of this thesis . . . 11

2 Theory of charge transport 13
2.1 Boltzmann transport equation . . . 13
2.2 Drift-diffusion equation . . . 14
2.3 Poisson's equation . . . 15
2.4 Model Assumptions . . . 16
2.5 Fermi level and Quasi-Fermi level . . . 17
2.6 Shockley-Read-Hall model . . . 18
2.6.1 Energy levels classification . . . 19
2.6.2 Trapping and detrapping . . . 20
2.7 Electrical contacts . . . 21
2.7.1 Ideal Ohmic contact . . . 21
2.7.2 Ideal Schottky contact . . . 22
2.7.3 Real metal-semiconductor contact . . . 22
2.8 Shockley-Ramo theorem . . . 24
2.9 Current waveform . . . 24
2.10 Surface recombination . . . 26
2.11 Hecht equation . . . 29

3 Numerical simulations 31
3.1 Solved equations . . . 31
3.2 Numerical methods . . . 32
3.3 Monte Carlo simulation . . . 33
3.3.1 Concept of Monte Carlo simulation . . . 33
3.3.2 Stability of Monte Carlo simulation . . . 36
3.3.3 Examples of Monte Carlo simulations . . . 38

4 Experimental techniques 50
4.1 Transient Current Technique . . . 50
4.2 Spectroscopic measurements . . . 52

5 Results and discussion 53
5.1 GaAs . . . 53
5.1.1 Results . . . 54
5.1.2 Model of the space charge formation . . . 56

5.1.3 Charge collection efficiency 59
5.1.4 Section conclusion 64
5.2 CdZnTe 65
5.2.1 Experiment 66
5.2.2 Simulation of the detector performance at low bias 68
5.2.3 Discussion 70
5.2.4 Section conclusion 79
5.3 CdZnTeSe 80
5.3.1 Results 81
5.3.2 Model 84
5.3.3 Spectroscopic measurements 90
5.3.4 Discussion 90
5.3.5 Section conclusion 94

6 Conclusion **95**

Bibliography **97**

List of Figures **107**

List of Tables **112**

List of Symbols and Abbreviations **113**

List of publications **118**

1. Introduction

1.1 Motivation

Semiconductors play a key role in our everyday lives. They are essential to all modern electronics, such as smartphones and computers. Without semiconductors, there would be no internet, and our society would be much different. Semiconductor technology has a rich history and is now a mature field with many applications in all branches of science. The history of semiconductors starts with the first experiments on the electrical properties of materials in the early 19th century. These experiments were mainly focused on light and temperature sensitivity of resistance and rectification. In the first half of the 19th century, Thomas Johann Seebeck observed the thermoelectric effect [1]. Michael Faraday made important measurements of decreasing the resistance of silver sulfide when it was heated, which was contrary to the behavior of metallic substances [2]. In the second half of the 19th century, Edwin Herbert Hall discovered the deflection of moving charge carriers in an applied magnetic field, the Hall effect [3]. J. J. Thomson's experiment with cathode rays lead to the discovery of electron [4].

A comprehensive explanation of these phenomena required a theory of solid-state physics that was mainly developed during the first half of the 20th century. Photoelectric effect measurements disagreed with classical electromagnetism, which predicted that continuous light with low frequency and high intensity would produce the same electron emission as high-frequency light with low intensity. Experimental results showed instead that electrons are only emitted when the frequency of light is large enough. This discrepancy between theory and experiment led Albert Einstein to propose that a beam of light is not a wave propagating through space but is composed of discrete packets of energy - photons [5]. This and other discoveries eventually led to wave-particle duality and quantum physics, successfully explaining the observed phenomena. In the first half of the 20th century, Felix Bloch published a theory of the movement of electrons through atomic lattices [6]. Alan Herries Wilson proposed the concept of band gap [7]. Boris Davydov developed the model of the p-n junction. Walter H. Schottky and Nevill Francis Mott developed the metal-semiconductor junction and pointed out the importance of minority carriers and surface states on charge transport [8].

Up to this point, most of the applications of semiconductors were resistors, rectifiers, and detectors used in telegraphy and early radios. The key moment was the invention of the transistor by John Bardeen and Walter Houser Brattain while working under William Shockley at Bell Laboratories in 1947 [9]. While the concept of electric current control was not new and was possible by using vacuum tubes or simple mechanical relays, the key advantage of the transistor was its low power consumption and size. The transistor enabled small devices which run with lower power. The list of devices is ever-increasing, from the first practical pocket radio to computers and smartphones with billions of transistors. The advancements in semiconductor manufacturing lead to increasing transistor density leading to even better energy consumption and more powerful devices. This technological revolution continues today.

One of the valuable applications of semiconductor materials is the detection of high-energy X-ray and gamma-ray radiation. Semiconductor detectors can directly convert radiation to an electric current that can be analyzed. This direct conversion allows faster operation and superior energy resolution than other radiation detectors like scintillators. Semiconducting detectors are important for applications in advanced medical imaging systems using lower radiation doses and providing a higher spatial resolution of biological tissue. The early semiconductors used for radiation detection, such as Ge, needed liquid nitrogen cooling because of the small band gap. This limited their application. The need for room-temperature semiconductors led to a search for new materials. These semiconductors should have certain material properties required for high-performance spectrometers with high counting efficiency and good spectral resolution. These properties are [10]:

1. High atomic number, Z, for efficient absorption of radiation.
2. Band-gap energy $E_g > 1.5$ eV for high resistivity ($> 10^9$ Ωcm) and suppression of leakage current at room temperature.
3. Band-gap energy $E_g < 5$ eV, to generate enough electron-hole pairs with small statistical variation ensuring a high signal-to-noise ratio.
4. Large mobility-lifetime product $\mu\tau$, is desired to ensure that carriers generated by radiation in the whole detector volume can be efficiently collected by electrodes.
5. Defect-free homogeneous material with good cross-sectional area and thickness. A large single-crystal volume is required to absorb enough incoming high-energy photons to achieve high sensitivity and efficiency. Low defect density and homogeneity ensure good charge transport.
6. Surfaces with sufficiently high electrical resistivity lowering noise caused by surface conduction.
7. Fabrication of stable contacts which produce no defects, impurities, or barriers to the charge collection process and that can be used to apply a uniform electric field inside the device.

Several new materials with mentioned properties were proposed, and in the second half of the 20th century, the vast expansion of semiconductor technology occurred. Besides group IV semiconductors like Ge and Si, compound semiconductors from groups III-V or II-VI, such as Gallium arsenide (GaAs) or Cadmium telluride (CdTe), were investigated [11, 12, 13].

1.2 Studied semiconductors

1.2.1 GaAs

Gallium Arsenide (GaAs) is III-V compound semiconductor with a direct band-gap, which crystallizes in a zinc-blende structure (see figure 1.1). GaAs has been studied for more than 40 years and has many applications in microwave frequency integrated circuits, solar cells, and laser diodes [14]. The preparation of high-quality detector-grade material was not possible until recently. Semiinsulating (SI) GaAs single crystals compensated by in-diffused chromium (GaAs:Cr) suitable for radiation detection recently appeared and are nowadays a promising X-ray detector material [15, 16]. It overcomes known drawbacks of the liquid encapsulated Czochralski (LEC) SI GaAs, which is significantly debased by EL2 defect [17, 18, 19]. GaAs:Cr exhibits extended electron lifetime and long-term stability at applied bias conserving benefits of SI-GaAs consisting mainly of a relatively high average atomic number (Z = 32), moderate energy band-gap ($E_g = 1.42$ eV) and high electron drift mobility ($\mu_e = 2500$ cm^2/Vs) [20, 21]. One of the key problems for the application of SI GaAs in high-performance radiation detectors is the space charge formation resulting in the internal electric field distortion. A model of the space charge formation and electric field distribution in SI LEC GaAs was presented by McGregor [22] and Kubicki [23]. McGregor included the effect of deep levels refilling at high field, and Kubicki took the leakage current into account. The model was extended by Cola [24], who assumed a spectrum of both shallow and deep levels for electrons and holes and the field-enhanced capture cross-section. Experimentally, the electric field distribution in LEC GaAs was investigated using the transient current technique (TCT) [25, 26, 27]. Due to very short lifetime of generated electrons, they measured current transients, which showed anomalous dependence on applied bias significantly warped by the effects of the associated electronic circuit. Comparison of electric field distribution in LEC GaAs and GaAs:Cr was done by Tyazhev et al. [28] using the Pockels effect. They presented a more homogeneous distribution of an internal electric field in GaAs:Cr compared to LEC GaAs. Selected properties of GaAs are shown in table 1.1.

1.2.2 CdTe, CdZnTe, CdZnTeSe

Cadmium Telluride (CdTe) and Cadmium Zinc Telluride (CdZnTe) are II-VI compound semiconductor with a direct band-gap, which crystallizes in a zinc-blende structure (see figure 1.1). CdZnTe has chemical formula $\mathrm{Cd_{1-x}Zn_xTe}$ where x ≈ 0.1 for material used in this work). The first extensive study of CdTe was published in 1959 by de Nobel [12], where basic electrical, optical, and mechanical properties of CdTe were described. While basic binary CdTe assures high radiation absorption and sufficient band-gap energy, Zn is added to the material to increase the band gap and the resistivity.

CdZnTe is a state-of-the-art material for radiation detection because it has a high atomic number resulting in a high probability of photoelectric effect and high density, giving it a high absorption coefficient, high resistivity, and wide band-gap, which allow CdZnTe to operate at room temperature [29]. Despite recent progress in CdZnTe technology [30], it suffers from several inconvenient problems:

non-unity segregation coefficient of Zn in the range 1.05 to 1.6, depending on the growth method and Zn content [31]; abundant emergence of crystal defects and networks (such as subgrain boundaries); and high concentrations of Te inclusions or precipitates [32, 10]. These issues result in a low yield and high cost of high-quality CZT radiation detectors, which limit their applications. Researchers have tried to solve these issues by improving the crystal-growth process and post-growth annealing, but they still need to mitigate all of these disadvantages [33, 34].

Up until the last decade, CdTe/CdZnTe detectors were not widely commercially available because of their high cost and low yield. Over the last several years, this has changed since improved crystal growth led to higher semiconductor quality and longer carrier lifetime [35, 36, 37]. These advancements allowed for the high-flux operation of X-ray semiconductor detectors in computer tomography and other applications.

Selenium is a very effective element in reducing the complications mentioned above [38, 39]. In addition, the Se segregation coefficient is near unity in the CdTe matrix. The quaternary semiconductor Cadmium Zinc Telluride Selenide (CdZnTeSe) with chemical formula $Cd_{1-x}Zn_xTe_{1-y}Se_y$ where $x \approx 0.1, y \approx 0.04$ for material used in this work) is expected to resolve long-standing problems associated with CZT material. The role of selenium in this semiconductor is [39, 40] (a) strong influence on the Zn segregation coefficient, and thus, better compositional homogeneity; (b) effective solution hardening in arresting subgrain boundaries and their networks; and (c) decreased Te inclusion or precipitate concentration. Hence, high-performance detector-grade CZTS material can be produced at a lower cost [41]. Selected properties of CZT, CZTS, and other semiconductors are shown in table 1.1.

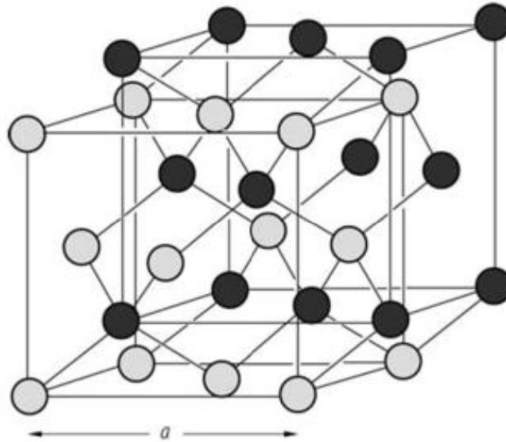

Figure 1.1: Zinc-blende crystal structure [42].

Table 1.1: Properties of semiconductor materials at room temperature. [11, 29, 43, 44, 45]

Material	Band gap (eV)	Resistivity (Ωcm)	Electron mobility (cm^2/Vs)	Hole mobility (cm^2/Vs)	Electron mobility-lifetime product (cm^2/V)	Hole mobility-lifetime product (cm^2/V)
Ge	0.67	50	3900	1900	> 1	> 1
Si	1.12	$< 10^4$	1400	450	> 1	> 1
GaAs	1.42	1×10^8	8500	400	8×10^{-5}	4×10^{-6}
CdTe	1.5	3×10^{10}	1150	110	3×10^{-3}	2×10^{-4}
CdZnTe †	1.572	1×10^{10}	1000	50	1×10^{-2}	5×10^{-5}
CdZnTeSe‡	1.52	1×10^{10}	1000	50	3×10^{-3}	5×10^{-4}

† Exact composition $Cd_{0.9}Zn_{0.1}Te$ ‡ Exact composition $Cd_{0.9}Zn_{0.1}Te_{0.96}Se_{0.04}$

1.3 Crystallographic defects and energy levels

A crystal is a solid material with its constituents (atoms, molecules, ions) forming an ordered structure - a crystal lattice that extends in all directions. Ideal crystal without defects is infinite and at temperature $\mathcal{T} = 0$ K. At non-zero temperatures, deviations from the ideal distribution of atoms occur, and several defect forms. Every crystal has a surface which is a type of defect. Crystallographic defects are interruptions in the crystal lattice and act as scattering centers for charge carriers. These defects pose one of the most severe problems in semiconductor manufacturing. Even a small concentration of defects (less than 1 part in billion) can have a large effect on semiconductor properties [9]. Prevention and suppression of defects are important areas of active study. The presence of defects in semiconductors leads to the formation of energy states inside the band gap. These energy states can be divided into two groups. The first is shallow levels, weakly localized states with activation energies E_t typically on the order of thermal energy $k_B\mathcal{T}$. Shallow states form lattice perturbations without significant detrimental influence on the material. The second group is deep levels with E_t significantly greater than $k_B\mathcal{T}$. Deep levels form more significant perturbations to the lattice close to the defect. The wave function of the trapped charge carrier (electron or hole) is much more localized. Deep levels present an enormous problem to semiconductor operation and impact charge collection efficiency acting as electron (hole) traps or recombination centers. This depends on their position in the band gap and the ratio of their capture cross-sections σ_e/σ_h, where $\sigma_e(\sigma_h)$ is the electron (hole) capture cross-section. Defects also influence electric conductivity, diffusion, plastic deformation, mechanical strength, and color. Crystallographic defects can be sorted into [46]:

1. Point defects (vacancies, interstitial defects, substitution defects)
2. Line defects (dislocations)

3. Surface (planar) defects (material surface, grain boundaries, stacking fault)
4. Bulk defects (Three-dimensional macroscopic) such as pores, cracks, voids (small regions where there are no atoms, and which can be thought of as clusters of vacancies), precipitates (clusters of impurities or constituting atoms in second phases)

In this thesis, only point defects are studied. The influence of line, planar, and bulk defects is out of the focus of this thesis.

1.3.1 Point defects

Point defects occur only at or around a single lattice point. A limit for how small a point defect has to be is not explicitly defined. However, these defects usually involve a few missing or extra atoms [46]. Point defects can be split into native defects and extrinsic defects. Native defects are due to atomic imperfections in the material. There are three types of native defects: vacancies, interstitials, and antisites. Vacancies are atomic sites where a host atom in an ideal crystal structure is missing [47]. For example, a Cd vacancy (V_{Ca}) in CdTe refers to an imperfection due to a missing Cd atom from its site in the crystal lattice. Interstitials are caused by positioning additional host atom in normally unoccupied positions. Antisites are atomic sites that are formed in compound crystals. They shape up when the lattice atom is substituted by its compound counterpart. Point defects in binary compound semiconductor AB are shown in figure 1.2. For example, Cd_{Te} (Cd antisite) refers to a Cd atom occupying a Te site in the crystal. For example, Cd_i refers to a Cd atom present inside the unit cell away from its actual atomic site in the crystal. There are also complexes of native defects, such as the Frenkel pair, which forms when an atom that leaves its place in a lattice (forming a vacancy) becomes an interstitial by getting into a nearby location. Frenkel pair is a stoichiometric defect that does not change the overall stoichiometry of the compound. Thermodynamics of defects equilibrium which is established according to specific external conditions (temperature, partial pressure of the gas phase of one of the semiconductor components), can be studied using formation energy and distribution of defects energy levels inside band gap [9]. Several experimental techniques to study shallow and deep levels, such as Hall effect measurements, photoluminescence (PL), deep level transient spectroscopy (DLTS), or transient current technique (TCT), can be used [48]. Identifying the defect by its observed energy level is difficult [46]. Besides native defects, there are also extrinsic defects, which are caused by impurities (foreign atoms) in the crystal. There are two types of extrinsic defects: substitutional and interstitial. Complexes of intrinsic and extrinsic defects exist. They can have distinct properties and behaviors compared to individual intrinsic or extrinsic defects. More details about defect complexes are in [49].

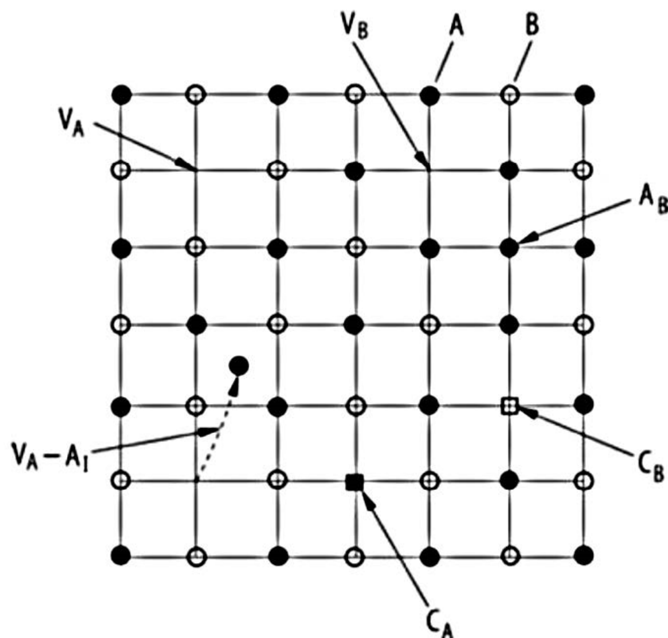

Figure 1.2: Point defects in binary compound semiconductor AB. C_A and C_B are impurity atoms at places of atom A and B. V_A, V_B are vacancies. A_B is antisite defect. $V_A - A_I$ is the Frenkel pair [50].

1.3.2 Doping

The intentional introduction of impurities into a semiconductor to modify its properties is called doping. It is widely used to produce semiconductor devices such as diodes or transistors [9]. Dopant atoms can be classified as donors if their introduction into the semiconductor forms an n-type region (a region with an excess of mobile electrons compared to intrinsic semiconductor) or acceptors if their introduction forms a p-type region. In the case of CdTe, the main dopants are In and Cl, which act as donors, and acceptor dopants is phosphorus [29]. High-quality semiconductor radiation detectors require a high mobility-lifetime product of electrons, high atomic weight, and high resistivity to reduce dark current. The former property can be achieved in CdTe by self-compensation of intrinsic point defects during crystal growth [51]. Native defects play an important role by limiting the p- or n-type conductivity in semiconductors [52] and can be achieved by extrinsic doping [53]. Understanding the effects of self-compensation in CdTe is a still area of active research [51]. For CdTe, group IV elements can be used as extrinsic dopants to achieve a semi-insulating material [53]. However, these impurities typically introduce deep levels in the band gap. They can act as non-radiative Shockley-Read-Hall recombination centers with a detrimental effect on the detector performance [54]. This is not a case of chlorine or indium doping of CdTe, which results in a high-resistive material with good carrier transport properties suitable for radiation detection [55]. The exact origin of the compensation mechanism and its effect on electric properties is not well understood and remains an open issue [56].

1.4 Ionizing radiation

Ionizing radiation is any radiation whose quanta have sufficient energy to ionize atoms or molecules by detaching electrons from them. Ionizing radiation can be sorted to [57]:

1. Alpha particles (two protons and two neutrons bound together into a particle identical to a helium nucleus)
2. Beta particles (high energy, high-speed electrons or positrons)
3. Gamma radiation (high energy photons from the radioactive decay of atomic nucleus)
4. X-ray (high energy photons with energy higher than ultraviolet (UV))
5. Neutron radiation (free neutrons emitted from nuclear fusion, fission, radioactive decay, within particle accelerators or particle interactions with cosmic rays)

X-rays can be sorted by energy into soft (photon energy < 10 keV) or hard X-rays with (photon energy > 10 keV). By method of generation, X-rays can be sorted into:

1. Characteristic X-ray emission - electromagnetic radiation produced when outer-shell electron fill a vacancy in the inner shell of an atom. The emission spectrum consists of discrete lines at specific energies corresponding to the energy difference between the involved electron energy levels. Since these levels are unique to each element, the emitted radiation is characteristic of each element.
2. Bremsstrahlung - electromagnetic radiation emitted by fast-moving charged particles when they are slowed down by passing through matter. The energy which charged particle loses in the process is emitted as a photon. The energy depends on the speed of the charged particle and is independent of the target material.

Ionizing radiation can interact with matter either directly or indirectly. Direct ionization is caused by Coulomb interaction between charged particles. Indirect ionization is caused by particles with no electric charge (photons and neutrons), whose interaction with atoms produces directly ionizing particles or initiates a nuclear transformation [57].

1.5 The goal of this thesis

This thesis is mainly focused on the study of charge transport and its effects on semiconductor radiation detector performance. GaAs, CdZnTe, and CdZnTeSe are studied by several electro-optical and spectroscopic experimental techniques to obtain detector transport properties such as carrier drift mobility, lifetime, electric field profile, and detector polarization. One of the goals is to expand on the Monte Carlo simulation and combine it with the numerical solution of coupled drift-diffusion equation with the Poisson's equation. This combination results in a significant speed-up of simulation and allows the fitting of experimental data to obtain transport properties. Another goal is to use Monte Carlo simulations to fit experimental data to get charge transport properties and gain insight into underlying processes.

In Chapter 1, studied semiconductors are introduced together with crystallographic defects and ionizing radiation. In Chapter 2, the overview of the transport equations, electrical contacts, and generation-recombination model is described. Important terms which are used in numerical simulations and experimental measurements are defined. In Chapter 3, about numerical simulations, the solved equations are presented together with numerical methods to solve them. Monte Carlo simulation and its combination with the numerical solution of coupled Poisson's equation together with the drift-diffusion equation is described. The stability of Monte Carlo simulation with examples of Monte Carlo simulation is presented. Experimental techniques are described in Chapter 4.

Chapter 5, where the main experimental results are shown and discussed, is divided into three parts corresponding to the studied semiconductor material.

In the first part, the electron-transport properties of GaAs are studied using a laser-induced transient-current technique with pulsed and DC bias. The formation of non-standard space charge caused by the appearance of both negatively and positively charged regions in DC-biased sensors is revealed. Using Monte Carlo simulations of current transients, we determined electron lifetime and electron drift mobility. We developed and successfully applied a theoretical model based on fast hole trapping in the system with spatially variable hole conductivity to describe measured effects.

In the second part, the polarization phenomena in the CdZnTe radiation detector induced by high-flux X-ray excitation under low applied bias are studied using several techniques. Semi-insulating CdZnTe crystals fabricated into pixelated sensors and integrated into radiation detection modules have demonstrated a remarkable ability to operate under rapidly changing X-ray irradiation environments. Such challenging conditions are required by all photon-counting-based applications, including medical CT, airport scanners, and non-destructive testing. However, maximum flux rates and operating conditions differ in each case. We investigate the possibility of pursuing the detector at the high-flux X-ray irradiation at a low electric field satisfactory for maintaining good counting operation. Electric field profiles obtained from Pockels effect measurement in the detector affected by the high-flux polarization are numerically simulated. The defect model that consistently depicts the polarization is obtained by solving coupled drift-diffusion and Poisson's equations.

Subsequently, the charge transport is simulated, and collected charge, includ-

ing the construction of the X-ray spectrum, is calculated for a commercial 2 mm thick pixelated CdZnTe detector with 330 μm pixel pitch used in spectral Computed Tomography applications. The effect of allied electronics on the quality of the spectrum is studied, and the setup optimization for improvement of the spectrum shape is suggested.

In the third part, the electron- and hole-transport properties in CdZnTeSe crystals are studied using a laser-induced transient-current technique with pulsed and DC bias. The internal electric field profile and velocity of surface recombination are determined by Monte Carlo simulations of electron and hole transient currents combined with a numerical solution of the drift-diffusion equation coupled with Poisson's equation. A simple technique for evaluating surface recombination directly from measured current waveforms without the need for numerical simulation is developed and experimentally tested. The formation of a positive space charge, originating from hole injection combined with a recombination level, is found. We observe a significant position dependence of the lifetime of electrons and holes in DC bias due to hole injection. The experiment is successfully fitted by a simple model dominated by a single deep recombination level.

These experimental results, together with numerical simulations and presented models, prove that Monte Carlo simulations combined with the numerical solution of coupled Poisson equation together with the drift-diffusion equation can reveal many interesting and important information about charge transport in semiconductors.

2. Theory of charge transport

2.1 Boltzmann transport equation

To describe charge transport in semiconductors, one can start by describing the statistical behavior of a thermodynamic system out of equilibrium. The semi-classical approach to this is based on the Boltzmann transport equation [58]:

$$\frac{\partial f}{\partial t} + \vec{v_g} \cdot \nabla_{\vec{r}} f - \frac{\vec{F}}{\hbar} \cdot \nabla_{\vec{k}} f = \left(\frac{\partial f}{\partial t}\right)_{col}, \tag{2.1}$$

where $\vec{r}$ is position, $\vec{k}$ is the momentum, $f(\vec{r}, \vec{k}, t)$ is distribution function (Fermi-Dirac distribution in equilibrium), $\vec{v_g}$ is the group velocity, $\vec{F} = -e\left[\vec{\mathcal{E}} + \vec{v_g} \times \vec{B}\right]$ is the Lorentz force, e is positive elementary charge, $\vec{\mathcal{E}}$ is electric field intensity, $\vec{B}$ is magnetic flux density. The distribution function depends on time, position, and momentum. The right side of (2.1) is collision term $\left(\frac{\partial f}{\partial t}\right)_{col}$, which takes into account scattering phenomena and can be defined as:

$$\begin{aligned}\left(\frac{\partial f}{\partial t}\right)_{col} = \sum_{\vec{k'}} \Big[& W(\vec{k'}, \vec{k}) f(\vec{r}, \vec{k'}, t)(1 - f(\vec{r}, \vec{k'}, t)) - \\ & W(\vec{k}, \vec{k'}) f(\vec{r}, \vec{k}, t)(1 - f(\vec{r}, \vec{k}, t))\Big],\end{aligned} \tag{2.2}$$

where $W(\vec{k}, \vec{k'})$ is the transition probability between the momentum states $\vec{k}$ and $\vec{k'}$, $\left[1 - f(\vec{r}, \vec{k'}, t)\right]$ is the probability of non-occupation for a momentum state $\vec{k'}$. The collision term is the only part of the Boltzmann transport equation that quantum mechanics describes. Other parts are classical, from which we get a semi-classical description of charge transport. The equation (2.1) is valid under these assumptions [58]:

1. Effective mass approximation (quantum effects due to periodicity of crystal)
2. Point-like particles
3. Instantaneous collisions
4. No memory effects (independence of initial conditions)
5. Single particle approximation (no correlation between particles)
6. Statistical description for a large number of particles
7. Born approximation for collisions (the scattering potential is small compared to the kinetic energy of the incident particle)

Except for simple cases, the Boltzmann transport equation has no general analytical solutions, and numerical methods must be used to obtain the solution. Phonons or defects in the material provide the dominant scattering mechanisms.

Both scattering mechanisms depend on the temperature. Collision term (2.2) can be simplified under relaxation time approximation:

$$\left(\frac{\partial f}{\partial t}\right)_{col} \approx -\frac{f - f_0}{\tau_{rel}}, \tag{2.3}$$

where f_0 is the local equilibrium distribution function, τ_{rel} is microscopic relaxation time, which is related to electron mobility μ_e via

$$\mu_e = \frac{e}{m_e^*}\langle\tau_{rel}\rangle, \tag{2.4}$$

where m_e^* is electron effective mass, $\langle\tau_{rel}\rangle$ is mean value of relaxation time.

2.2 Drift-diffusion equation

The solution of the Boltzmann transport equation (2.1) is complicated. Therefore, simpler approaches are often used. The drift-diffusion current equations can be derived directly from the Boltzmann transport equation [59]. Drift-diffusion equation (DDE) for electrons is

$$\vec{j_e} = e\mu_e n\vec{\mathcal{E}} + eD_e\nabla n + eS_e\nabla\mathcal{T}, \tag{2.5}$$

where the first part is a drift term caused by the external electric field, the second is a diffusion term due to the gradient of electron concentration in conduction band n, and the third is a diffusion term due to the gradient of absolute temperature $\mathcal{T}$, $\vec{j_e}$ is electron current density, D_e is the diffusion coefficient for electrons, S_e is the Seebeck coefficient for electrons. The diffusion coefficient is related to mobility by the Einstein relation

$$D_e = \frac{k_B\mathcal{T}}{e}\mu_e, \tag{2.6}$$

where k_B is Boltzmann constant [60]. Seebeck coefficient is defined as

$$S_e = \frac{k_B n}{e}\mu_e. \tag{2.7}$$

To get analogical equations for holes we let $e \to -e$, $\mu_e \to -\mu_h$ and obtain drift-diffusion equation for holes

$$\vec{j_h} = e\mu_h p\vec{\mathcal{E}} - eD_h\nabla p - eS_h\nabla\mathcal{T}, \tag{2.8}$$

where p is hole concentration in valence band, $\vec{j_h}$ is hole current density, D_p is the diffusion coefficient for holes, S_p is the Seebeck coefficient for holes. The diffusion coefficient and Seebeck coefficient for holes are

$$D_h = \frac{k_B\mathcal{T}}{e}\mu_h, \tag{2.9}$$

$$S_h = \frac{k_B p}{e}\mu_h. \tag{2.10}$$

The sum of electron and hole current densities is equal to the total density of electric current inside the semiconductor at any point

$$\vec{j} = \vec{j_e} + \vec{j_h}. \tag{2.11}$$

The semiconductor conductivity σ is related to electron and hole mobility by equation

$$\sigma = e(n\mu_e + p\mu_h), \tag{2.12}$$

and semiconductor resistivity ϱ is related by equation

$$\varrho = \frac{1}{\sigma} = \frac{1}{e(n\mu_e + p\mu_h)}. \tag{2.13}$$

If the temperature is constant, the diffusion term due to the gradient of temperature is zero and the drift-diffusion equations (2.5) and (2.8) simplify to

$$\vec{j_e} = e\mu_e n\vec{\mathcal{E}} + eD_e\nabla n, \tag{2.14}$$

and

$$\vec{j_h} = e\mu_h p\vec{\mathcal{E}} - eD_h\nabla p. \tag{2.15}$$

To solve the kinetics of charge carriers, we can use the continuity equation for electrons

$$\frac{\partial n}{\partial t} = \frac{1}{e}\nabla \cdot \vec{j}_e + G_e - U_e \tag{2.16}$$

and for holes

$$\frac{\partial p}{\partial t} = -\frac{1}{e}\nabla \cdot \vec{j}_h + G_h - U_h, \tag{2.17}$$

where G_e and G_h are generation rates, U_e and U_h are the recombination rates for electrons resp. holes. These equations represent the conservation of electric charge.

2.3 Poisson's equation

To solve the charge transport in semiconductor with the presence of space charge, the Poisson's equation must be used [59]:

$$\Delta\phi = -\frac{e\rho}{\varepsilon}, \tag{2.18}$$

ϕ is electrostatic potential, ρ is the space charge density, ε is semiconductor electrical permittivity, which is related to vacuum permittivity ε_0 and semiconductor relative permittivity ε_r

$$\varepsilon = \varepsilon_0\varepsilon_r. \tag{2.19}$$

The electric field connected to space charge density via the Gauss law [61]

$$\nabla \cdot \vec{\mathcal{E}} = \frac{e\rho}{\varepsilon_0\varepsilon_r}, \tag{2.20}$$

where electric field $\vec{\mathcal{E}}$ is related to electrostatic potential via

$$\vec{\mathcal{E}} = -\nabla\phi. \tag{2.21}$$

The total space charge density inside the semiconductor is given by sum

$$\rho = p - n - N_A^- + N_D^+, \tag{2.22}$$

where N_A^- is the density of ionized acceptors, and N_D^+ is the density of ionized donors.

2.4 Model Assumptions

One can use certain symmetries and approximations to simplify equations of charge transport. When the detector is rectangular with two planar opposite electrodes with a distance L, which is much less than the size of the electrodes, one can treat the detector as one dimensional (1D) and use only one spatial coordinate labeled throughout the text as x-coordinate. When the detector is irradiated either by X-ray or light, we assume that the irradiated area is near the center of the electrode and is small enough that the electric field across the area is homogeneous and perpendicular to it. Described detector geometry is shown in figure 2.1. Another assumption is that the drift mobility μ is not dependent on space, time, and electric field. This corresponds to small perturbations of the equilibrium state in low fields to prevent velocity saturation and hot carrier effects. Another assumption is that the detector is homogeneous with position-independent permittivity ε. Electrons (holes) are considered non-interacting, and the photogenerated charge is small, so its contribution to the internal electric field is negligible. Several useful functions are needed in analytical solutions of simple cases of drift-diffusion equation. They are $\delta(x)$ is the Dirac delta function. For the simplification of later used formulas, we define the boxcar function

$$\chi_{[0,x_1]}(x) = \Theta(x) - \Theta(x - x_1) = \begin{cases} 1 & 0 \leq x \leq x_1 \\ 0 & \text{otherwise,} \end{cases} \tag{2.23}$$

where $\Theta(x)$ is the Heaviside unit step function

$$\Theta(x) = \begin{cases} 0 & x < 0 \\ 1 & x \geq 0. \end{cases} \tag{2.24}$$

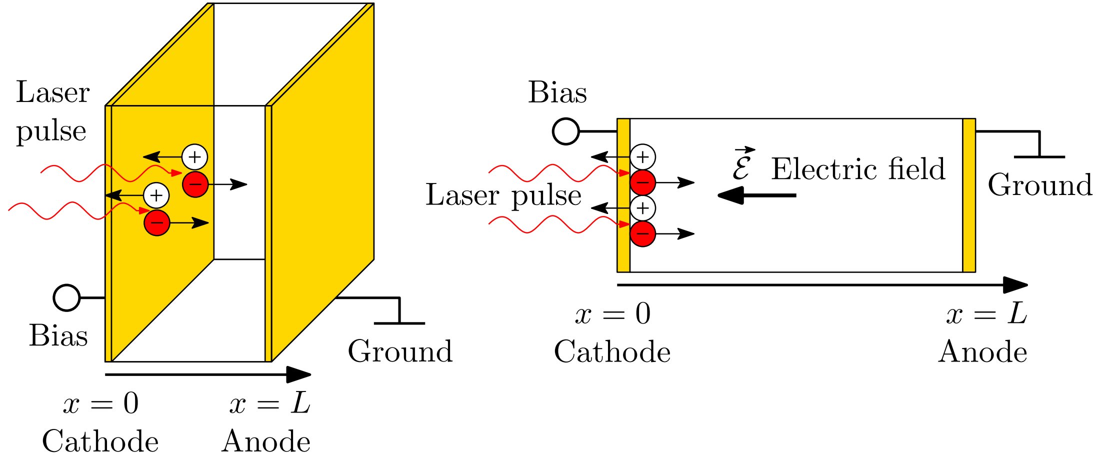

Figure 2.1: **Left**: Scheme of the detector with two planar electrodes, which are depicted with gold color. **Right**: 1D model of the detector, where electrons and holes can move only along the x-axis. The vertical dimension is only for the visualization of electrons and holes.

2.5 Fermi level and Quasi-Fermi level

When the detector is in thermodynamic equilibrium, the charge probability density is given by Fermi-Dirac distribution

$$f_n(E) = \frac{1}{1 + \exp\left(\frac{E-E_F}{k_B \mathcal{T}}\right)}, \tag{2.25}$$

where E_F is the Fermi level. In the case of non-degenerated densities when the Fermi level lies more than $3k_B\mathcal{T}$ below the conduction band, equation (2.25) can be simplified to Boltzmann distribution

$$f_n(E_C) = \exp\left(\frac{E_F - E_C}{k_B \mathcal{T}}\right), \tag{2.26}$$

and electron density is given by

$$n = N_C \exp\left(\frac{E_F - E_C}{k_B \mathcal{T}}\right), \tag{2.27}$$

and similarly for holes

$$p = N_V \exp\left(\frac{E_V - E_F}{k_B \mathcal{T}}\right), \tag{2.28}$$

where E_C resp. E_V is the energy of conduction resp. valence band ($E_C = E_V + E_g$), E_g is band-gap energy, N_C resp. N_V is the effective density of states in the conduction (valence) band given by

$$N_C = 2\left(\frac{2\pi m_e^* k_B \mathcal{T}}{h^2}\right)^{\frac{3}{2}} \tag{2.29}$$

$$N_V = 2\left(\frac{2\pi m_h^* k_B \mathcal{T}}{h^2}\right)^{\frac{3}{2}}. \tag{2.30}$$

The condition on non-degeneracy holds when $n \ll N_C, p \ll N_V$. When carriers are outside equilibrium, distribution with one Fermi level for electrons and holes can no longer be used to describe carrier statistics, but it is useful to define a quasi-Fermi level for electrons E_{Fe} and holes E_{Fh} to describe carrier statistics not far from equilibrium

$$n = N_C \exp\left(\frac{E_{Fe} + e\phi - E_C}{k_B \mathcal{T}}\right) \tag{2.31}$$

$$p = N_V \exp\left(\frac{E_V - e\phi - E_{Fh}}{k_B \mathcal{T}}\right). \tag{2.32}$$

Term $-e\phi$ represents electron potential energy, which has to be included in electron (hole) energy in equations (2.31) and (2.32). Now $n = n(x,t)$ and $p = p(x,t)$ are both generally time and position-dependent. Carrier distributions with quasi-Fermi level can never depart too far from thermodynamic equilibrium in time scales of practical interest, i.e., scattering time $\ll$ time scales of studied effects. This means that carriers undergo many collisions and attain thermal

quasi-equilibrium with crystal lattice and among themselves very quickly [9]. If we take derivative of (2.31) with respect to x we get

$$\frac{\partial n}{\partial x} = \frac{n}{k_B \mathcal{T}} \left(\frac{\partial E_{Fe}}{\partial x} + e \frac{\partial \phi}{\partial x} \right), \tag{2.33}$$

By plugging (2.33) into (2.14) with (2.21) in 1D we get

$$j_e = \mu_e n \frac{\partial E_{Fe}}{\partial x} \tag{2.34}$$

and similarly for holes

$$j_h = \mu_h p \frac{\partial E_{Fh}}{\partial x}. \tag{2.35}$$

The equations (2.34) and (2.35) state that the gradient of the quasi-Fermi level is the unifying driving force for carrier flow. It is important to note that outside thermodynamic equilibrium $E_{Fe} \neq E_{Fh}$. Multiplying (2.31) and (2.32) we get

$$np = n_i^2 \exp\left(\frac{E_{Fe} - E_{Fh}}{k_B \mathcal{T}} \right), \tag{2.36}$$

where n_i is intrinsic carrier density

$$n_i = N_C N_V \exp\left(-\frac{E_g}{k_B \mathcal{T}} \right) \tag{2.37}$$

and obtain three cases for local net recombination rate valid at any position

1. $E_{Fe} > E_{Fh} \implies np > n_i^2 \implies$ Net generation
2. $E_{Fe} < E_{Fh} \implies np < n_i^2 \implies$ Net recombination
3. $E_{Fe} = E_{Fh} \implies np = n_i^2 \implies$ Concentrations in thermal equilibrium

2.6 Shockley-Read-Hall model

Shockley-Read-Hall (SRH) model describes the trap-assisted generation and recombination of electric charge in semiconductors. Recombination of electrons and holes is a process by which both carriers annihilate each other [54]. Non-radiative recombination occurs primarily through trap-assisted recombination and has a detrimental effect on semiconductor detector performance. Understanding and preventing charge trapping is essential for developing high-quality radiation detectors. SRH model for one energy level in band gap with concentration N_t and energy E_t can be described by a set of rate equations [62]

$$\frac{\mathrm{d}n}{\mathrm{d}t} = G - U_e \tag{2.38}$$

$$\frac{\mathrm{d}p}{\mathrm{d}t} = G - U_h \tag{2.39}$$

$$\frac{\mathrm{d}n_t}{\mathrm{d}t} = U_e - U_h, \tag{2.40}$$

where n_t is electron concentration on center, G is the rate of charge carriers generation. The simplified scheme of a semiconductor with one deep level E_t is shown in figure 2.2. The electron recombination rate is

$$U_e = \sigma_e \nu_e \left[(N_t - n_t)n - n_t n_1 \right], \tag{2.41}$$

and hole recombination rate is

$$U_h = \sigma_h \nu_h \left[n_t p - (N_t - n_t)p_1 \right], \tag{2.42}$$

where σ_e, σ_h are electron (hole) capture cross-sections, ν_e, ν_h are electron (hole) thermal velocities given by

$$\nu_e = \sqrt{\frac{8k_B\mathcal{T}}{\pi m_e^*}}, \tag{2.43}$$

$$\nu_h = \sqrt{\frac{8k_B\mathcal{T}}{\pi m_h^*}}, \tag{2.44}$$

and n_1 and p_1 are electron (hole) density in case of Fermi level E_F being set at the center energy E_t (see equations (2.27), (2.28)) and are given by

$$n_1 = N_C \cdot \exp\left(\frac{E_t - E_C}{k_B\mathcal{T}}\right) \tag{2.45}$$

$$p_1 = N_V \cdot \exp\left(\frac{E_V - E_t}{k_B\mathcal{T}}\right). \tag{2.46}$$

The sum of electron and hole concentration on the center is equal to the concentration of the center N_t

$$N_t = n_t + p_t, \tag{2.47}$$

from which we can only operate with n_t and obtain p_t. If the system is in equilibrium, then the n_t is

$$n_t = \frac{N_t}{\exp\left(\frac{E_t - E_F}{k_B\mathcal{T}}\right) + 1}, \tag{2.48}$$

where Fermi-Dirac distribution is used since the condition of non-degeneracy is generally not valid for E_t.

2.6.1 Energy levels classification

Energy levels can be classified by capture cross-section to

1. Recombination center ($\sigma_e \approx \sigma_h$)
2. Electron trap ($\sigma_e \gg \sigma_h$)
3. Hole trap ($\sigma_e \ll \sigma_h$)

By distance from conduction band to shallow ($E_C - E_t \approx k_B\mathcal{T}$) or deep ($E_C - E_t \gg k_B\mathcal{T}$) electron trap and for holes to shallow ($E_t - E_V \approx k_B\mathcal{T}$) or deep ($E_t - E_V \gg k_B\mathcal{T}$) hole trap. Energy levels below the Fermi level are mostly filled by electrons and act as hole traps. Energy levels above the Fermi level are mostly empty and act as an electron trap. The nature of levels near the Fermi level is more complicated [62].

2.6.2 Trapping and detrapping

Lets assume case of electron trap with $\sigma_h \ll \sigma_e$, then we get $U_h \approx 0$ and if $G = 0$ equations (2.38) and (2.40) become

$$\frac{\mathrm{d}n}{\mathrm{d}t} = -U_e \tag{2.49}$$

$$\frac{\mathrm{d}n_t}{\mathrm{d}t} = U_e \tag{2.50}$$

If we substitute (2.41) into (2.49) and (2.50) we get the final kinetic equations for electron trap

$$\frac{\mathrm{d}n}{\mathrm{d}t} = -\frac{n}{\tau_T} + \frac{n_t}{\tau_D} \tag{2.51}$$

$$\frac{\mathrm{d}n_t}{\mathrm{d}t} = -\frac{n_t}{\tau_D} + \frac{n}{\tau_T}, \tag{2.52}$$

where τ_T is trapping time

$$\tau_T = \frac{1}{(N_t - n_t)\sigma_e \nu_e} \tag{2.53}$$

and τ_D is detrapping time

$$\tau_D = \frac{1}{N_C \sigma_e \nu_e} \exp\left(-\frac{E_t - E_C}{k_B \mathcal{T}}\right) \tag{2.54}$$

The scheme of trapping and detrapping processes is shown in figure 2.3. Analogous equations can be obtained for holes. Detrapping time does not depend on trap filling, and in the case of a nearly empty trap ($n_t \ll N_t$) we get constant trapping time.

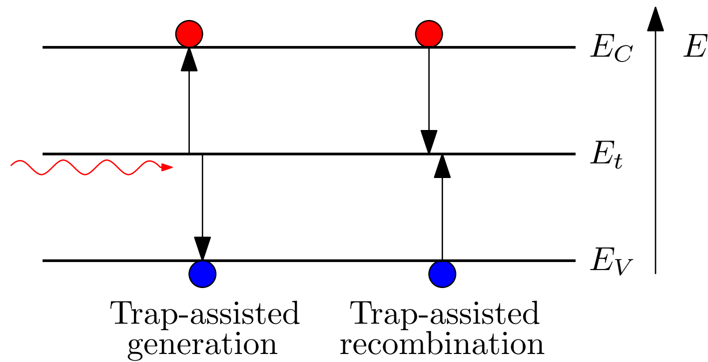

Figure 2.2: The Shockley-Read-Hall model of generation and recombination processes.

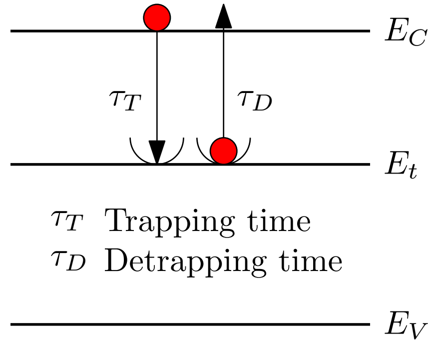

Figure 2.3: Trapping and detrapping.

2.7 Electrical contacts

Electrical contacts and their preparation have, together with material parameters (see section 1.1) critical impact on detector quality [60]. There are two basic metal-semiconductor contact types: Ohmic contact and rectifying Schottky contact. Ohmic contacts do not restrict the current flow depending on direction. Schottky contacts contain potential barriers in the metal-semiconductor interface, which generate a space charge region inside the semiconductor. Space charge restricts the free carrier injection in one direction and prevents current flow in the opposite direction. Potential barriers determine the type of electric contact. They can form when semiconductor and metal work function differs or in the presence of surface states or oxide layer. Electrical contacts affect detector polarization. Schottky contacts generally enhance the polarization effects, whereas Ohmic contacts suppress polarization. The basic theory of electrical contacts will be demonstrated on n-type semiconductor (for p-type semiconductor the inequality sign is the opposite). The band diagram of separated metal and semiconductor is in figure 2.4, where E_{FM} is the Fermi level of metal, E_{FS} is the Fermi level of semiconductor, Φ_M is work function of the metal, Φ_S is work function of semiconductor, $\Phi_K = \Phi_M - \Phi_S$ is contact potential, E_0 is rest energy of an electron in a vacuum and χ is semiconductor electron affinity.

2.7.1 Ideal Ohmic contact

In the case of ideal Ohmic contact, the flow of electrons is not restricted in any polarity of the applied voltage. This happens when the metal work function is less than or equal semiconductor work function, i.e., $\phi_M \leq \phi_S$ (which in the 2.5 figure causes the energy band to bend downwards, where the band diagram of an ideal Ohmic contact on an N-type semiconductor is shown). Electrons can pass in both directions between the metal and the semiconductor. In this case, the volt-ampere (V-A) characteristic satisfies Ohm's law and is linear for both polarities of the [60]. The band diagram of flat-band Ohmic contact for $\phi_M = \phi_S$, which represents ideal contact that neither blocks nor injects carriers into the semiconductor, is shown in figure 2.6. The band diagram of an ideal injecting Ohmic contact is shown in figure 2.5, E_F is the Fermi level equal for the metal and semiconductor at thermodynamic equilibrium, Φ_B is the height of

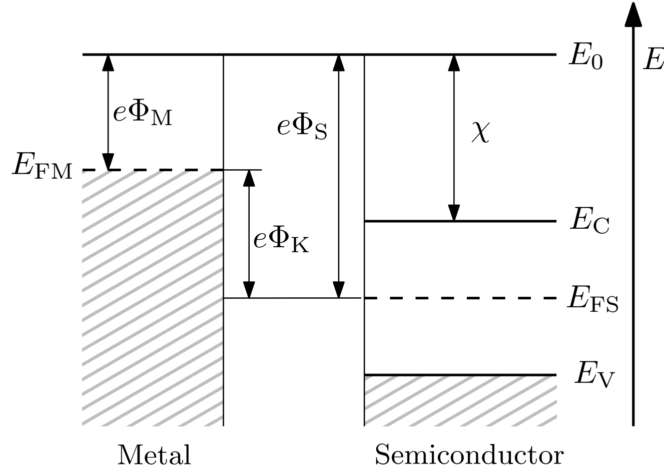

Figure 2.4: Band diagram of separated metal (left) and semiconductor (right) for $\Phi_M < \Phi_S$ [60].

the potential barrier between the metal and semiconductor, V_D is the diffusion voltage. The height of the potential barrier Φ_B is given by the relation [60]

$$e\Phi_B = e\Phi_M - \chi. \tag{2.55}$$

2.7.2 Ideal Schottky contact

In the case of ideal Schottky contact, the flow of electrons is restricted by the potential barrier caused by space charge presence. This happens when the metal work function is greater than the semiconductor work function, i.e., $\phi_M > \phi_S$ (which in the figure 2.7 causes the energy bands of the semiconductor to bend upwards), a potential barrier (Schottky barrier, whose height Φ_B is affected by the Schottky effect see [60]) is formed by the presence of an immobile space charge in the space charge region of width w. Suppose we apply a voltage to the Schottky contact with a positive potential on the semiconductor. In that case, the diffusion current from the semiconductor will be suppressed due to the change in the band structure. The total current will be given only by the small drift current formed by the e-h pairs created in the space charge region in the semiconductor. This state is under reverse bias. Suppose we apply a voltage to the Schottky contact with a positive potential on the metal and a negative potential on the semiconductor. In that case, the width of the space charge region is reduced, and thus the potential barrier is lowered. This allows electrons to pass from the semiconductor into the metal by the emission-diffusion process [60]. This state is under forward bias. The situation is analogous to a p-type semiconductor, except that the sign of the polarity of the applied voltage is reversed. The band diagram of an ideal Schottky contact on an n-type semiconductor is shown in Figure 2.7. For the height of the potential barrier Φ_B, the same relation as (2.55) holds.

2.7.3 Real metal-semiconductor contact

The types of contacts mentioned before are only approximations of the real metal-semiconductor contact. They are valid for an infinite crystal or a region of a finite

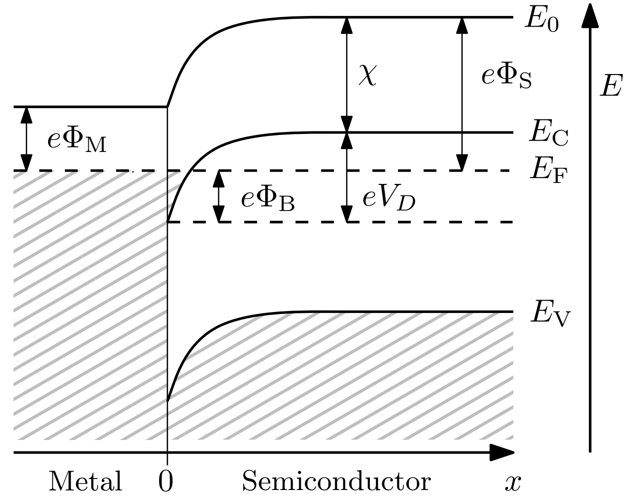

Figure 2.5: Band diagram of injecting Ohmic contact [60, 63].

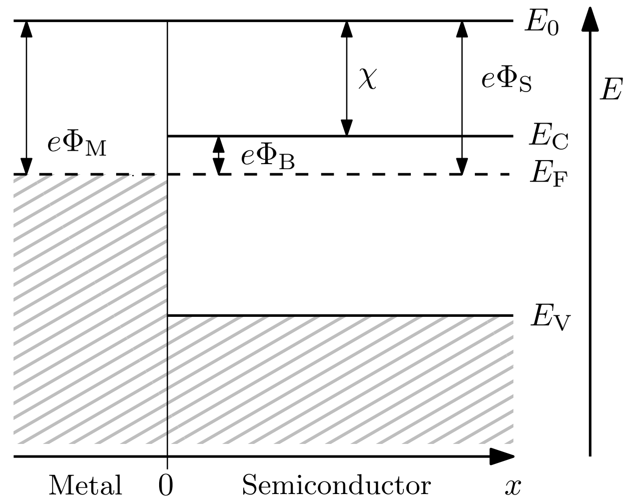

Figure 2.6: Band diagram of flat-band Ohmic contact [63].

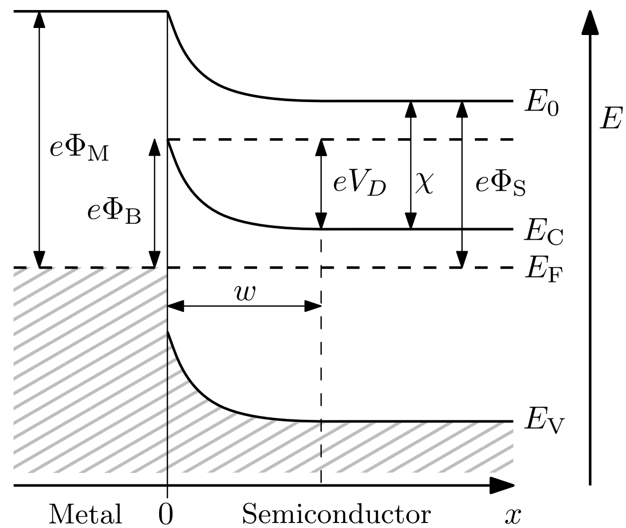

Figure 2.7: Band diagram of Schottky contact [60, 63].

crystal far from the surface. The region close to the surface has different physical properties than the rest of the crystal, firstly because atoms are absorbed from the surroundings, and secondly because the material is not chemically inert and a layer of chemical reaction products (e.g., oxides) can form. This layer has, in most cases, the semi-insulating properties of [60]. Another factor is the presence of surface states, which are electron states on the surface of the material that arise as a result of a sharp transition between the material (solid) and the surrounding environment (see section 1.3). These states cause changes in the material's band structure and associated changes in the material properties at the surface. The presence of surface states makes it impossible to determine the type of contact from knowledge of the work function alone. It is important to note that in the case of intrinsic semiconductors or compensated high resistivity semiconductors, the classification of electrical contacts is more difficult [63]. The issue of contacts is discussed more in [60].

2.8 Shockley-Ramo theorem

The Shockley-Ramo theorem is a method to calculate electric current induced by moving electric charges in the vicinity of an electrode. It is based on the concept of current induction due to instantaneous electrostatic flux change on the electrode rather than the charge passing through it per second. [64]. When elementary charge e moves a distance Δx between two parallel electrodes, in a direction parallel to the electric field, it induces a charge ΔQ at the electrodes, that is given by [65]

$$\Delta Q = e\frac{\Delta x}{L}, \tag{2.56}$$

where L is the distance between electrodes. The total induced current $I(t)$ is the time derivative of (2.56) summed over all drifting carriers

$$I(t) = \frac{Q(t)v(t)}{L}, \tag{2.57}$$

where Q is the moving charge and v is the velocity of the moving charge. The equation (2.57) is a special case of a more general Shockley-Ramo theorem for more complex contact configuration [64]. In general 1D case, the induced current on the collecting electrode can be calculated using

$$I(t) = Q(t)v(t)E_W(t), \tag{2.58}$$

where weighting field E_W is the electric field associated with the collecting electrode at unit potential and all other electrodes at zero potential [66]. For detector with two planar electrodes separated by distance L, the weighting field is constant $E_W = \frac{1}{L}$, this corresponds to equation (2.57). More information about weighting field and other electrode configuration is in [66, 67].

2.9 Current waveform

In this thesis, the key experimental data are transient currents from which numerical simulations will determine transport parameters. Current waveform (CWF)

is time-dependent current signal. This section shows an example of CWFs for a detector with constant applied bias U with one deep electron trap level with trapping time τ_T (see subsection 2.6.2), no diffusion, and no space charge. For electrons under mentioned conditions, the equation (2.14) becomes

$$\frac{\partial n(x,t)}{\partial t} = -v_0 \frac{\partial n(x,t)}{\partial x} - \frac{n(x,t)}{\tau_T}, \tag{2.59}$$

where $v_0 = \mu_e \mathcal{E}_0$ is electron drift velocity, $\mathcal{E}_0 = U/L$ is constant electric field inside detector. The general solution of (2.59) is

$$n(x,t) = n_0(x - v_0 t) \exp\left(-\frac{t}{\tau_T}\right) \chi_{[0,t_r]}(t), \tag{2.60}$$

where $n_0(x) = n(x, t = 0)$ is the initial charge distribution, $\chi_{[0,t_r]}(t)$ assures charge collection outside detector. Electron cloud $n(x,t)$ drifts through the detector with its center $x_C(t) = v_0 t$ moving with constant drift velocity, until the cloud arrives at the collecting electrode $x_C(t_r) = L$ in time t_r called the transit time, which is in our case is $t_r = L/v_0$. Scheme of the detector and electron cloud are shown in the left part of figure 2.8. Using equation (2.57) and (2.60) we obtain CWF

$$I(t) = \frac{Q_0}{t_r} \exp\left(-\frac{t}{\tau_T}\right) \chi_{[0,t_r]}(t). \tag{2.61}$$

The CWF in (2.61) represents exponential decay of charge carriers in bulk, more details in [68]. In the case of a short excitation pulse that generates charge carriers near under cathode, the generated holes are immediately collected, and only electrons drift through the bulk. Electron CWFs are shown in the right part of figure 2.8, where normalized CWFs for several values of τ_D are shown. More complicated CWFs require numerical solutions of equation (2.14) and will be shown later in this thesis.

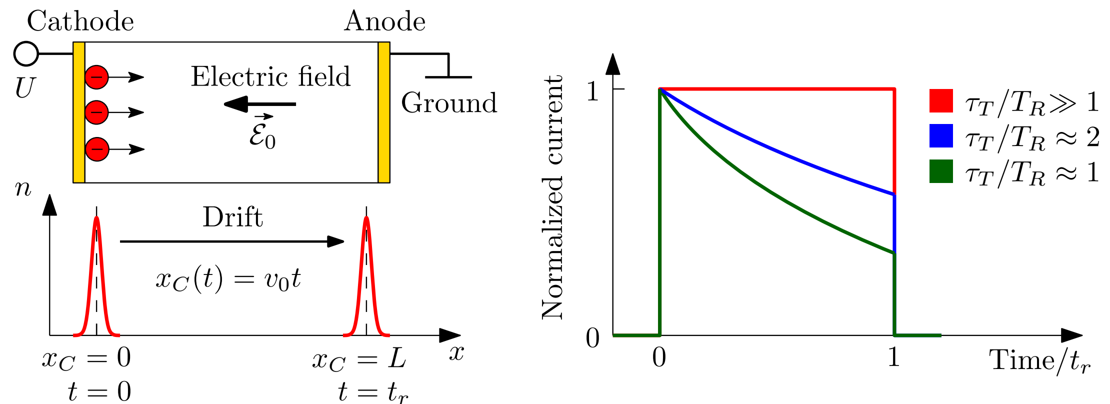

Figure 2.8: **Left**: Detector scheme and electron cloud at two times $t = 0$ and $t = t_r$. **Right**: Normalized current waveforms for several values of trapping time τ_T. Negligible trapping (red) shows ideal charge transport with no losses. Other curves show exponential decay current waveforms. At time $t/t_r = 1$ the electron cloud is collected and current stops.

2.10 Surface recombination

Every detector has a surface layer that has different properties from bulk. This results in surface states and defects that can recombine charge and thus affect charge transport. Surface recombination depends on many surface properties and is usually described using a phenomenological model based on surface recombination velocity s [69, 70]. Surface recombination velocity defines the probability of charge carriers generated inside the surface layer to enter the bulk p_{bulk} [69]. This can be written for electrons as

$$\frac{p_{bulk}}{1 - p_{bulk}} = \frac{v_0}{s}, \tag{2.62}$$

where $v_0 = \mu_e \mathcal{E}_0$ is electron drift velocity in surface layer, $\mathcal{E}_0$ is electric field in surface layer. The initially photogenerated charge Q_{00} in the surface layer partially recombines, rest of the charge Q_0 enters the bulk

$$Q_0 = Q_{00} \frac{1}{1 + \frac{s}{\mu_e \mathcal{E}_0}}. \tag{2.63}$$

Scheme of detector with surface layer with thickness $x_s \ll L$ is shown in figure 2.9. For the detector with applied bias U and no space charge, the electric field is constant ($\mathcal{E}(x) = \mathcal{E}_0 = \frac{U}{L}$). The equation (2.63) can be rewritten into

$$Q_0 = Q_{00} \frac{1}{1 + \frac{sL}{\mu_e U}}. \tag{2.64}$$

The equation (2.64) saturates the initial charge $Q_0(U)$ to the value Q_{00} as the bias U increases. This is shown in figure 2.10, where the ratio of charge entering the bulk from surface $Q_0(U)/Q_{00}$ is shown for several values of s and detector thickness $L = 0.2$ cm. At bias zero, the ratio $Q_0(U)/Q_{00}$ is zero except for the case with no surface recombination ($s = 0$). As bias increases, the ratio $Q_0(U)/Q_{00}$ saturates to one marking negligible recombination. Surface recombination occurs for only a short time when charge carriers drift through a thin surface layer. Only the amplitude of the measured current waveform is decreased compared to a much longer drift time through bulk for the typical detector length. Comparison of normalized CWF with and without SR for two values of applied bias (U and $U/2$) is shown in figure 2.11. Without SR, normalized CWF by corresponding bias have a common envelope (bottom left). With SR, there is a separation between CWFs (bottom right). This represents a simple method to determine the presence of surface recombination [71].

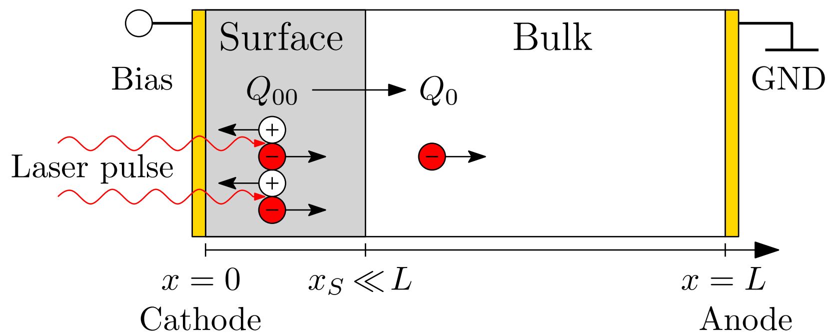

Figure 2.9: Detector with surface layer and bulk. The surface layer is much thinner than the bulk. Photogenerated charge Q_{00} is initially partially recombined, and only part Q_0 enters the bulk.

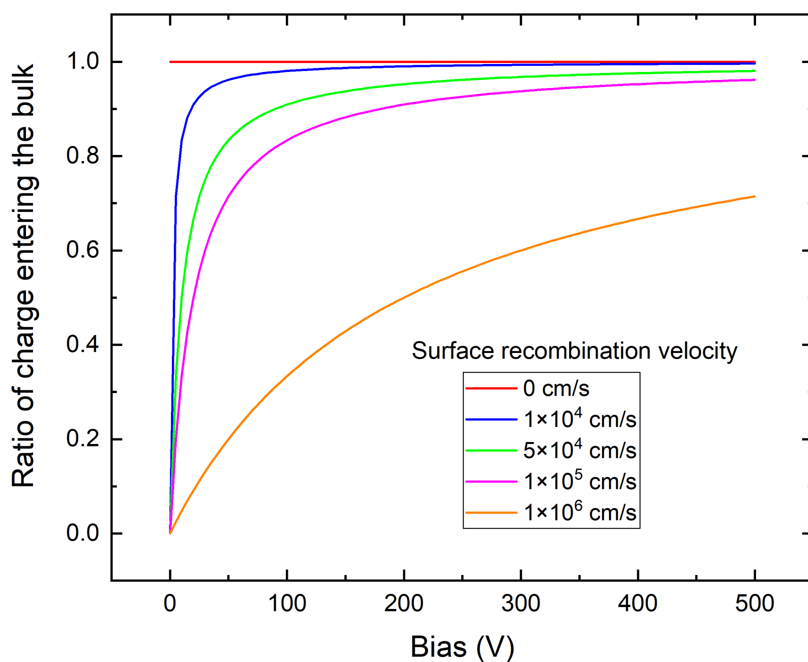

Figure 2.10: Bias dependence of ration of charge entering the bulk from the surface layer for different values of surface recombination velocity.

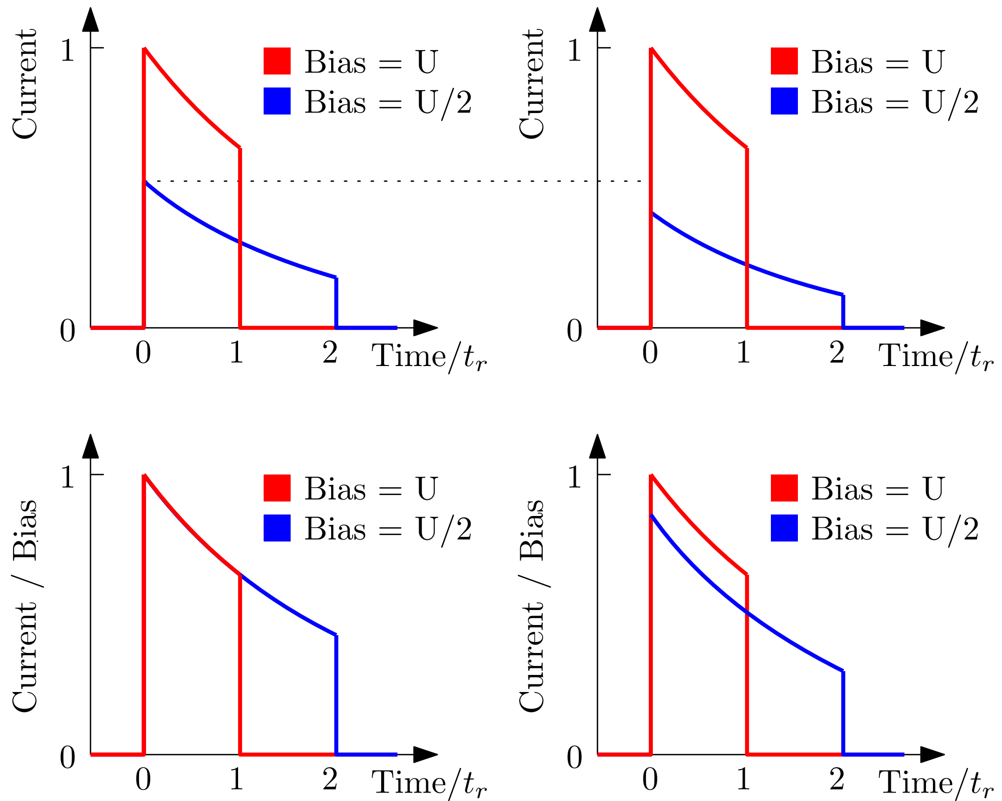

Figure 2.11: **Top left**: Current waveforms for the detector without surface recombination. **Top right**: Current waveforms for the detector with surface recombination. **Bottom left**: Current waveforms normalized by respective bias for detector without surface recombination. **Bottom right**: Current waveforms normalized by respective bias for a detector with surface recombination.

2.11 Hecht equation

The general expression for charge collection efficiency (CCE) for charge $Q(x_0)$ produced at the position x_0 inside the detector is obtained according to [23, 72]:

$$\begin{aligned} CCE(x_0) = \frac{1}{L}\Bigg[\int_{x_0}^{L} \exp\left(-\int_{x_0}^{x} \frac{\mathrm{d}x'}{\mu_e \tau_e \mathcal{E}(x')} \right) \mathrm{d}x + \\ + \int_{0}^{x_0} \exp\left(-\int_{x}^{x_0} \frac{\mathrm{d}x'}{\mu_h \tau_h \mathcal{E}(x')} \right) \mathrm{d}x \Bigg]. \end{aligned} \tag{2.65}$$

This formula comprises two parts: the first is for electrons, and the second is for holes. Bias is set so the cathode is at $x = 0$ and the anode is at $x = L$. The detector scheme with the generated charge at position x_0 by incident radiation is shown in figure 2.12. To obtain the total CCE, we need to integrate $CCE(x)$ over the whole detector bulk

$$CCE = \int_0^L \frac{Q(x)}{Q_0} CCE(x)\mathrm{d}x, \tag{2.66}$$

where total generated charge Q_0 is

$$Q_0 = \int_0^L Q(x)\mathrm{d}x. \tag{2.67}$$

The general equation for CCE (2.66) can be simplified in several useful cases. The first case is when there is a constant electric field inside the detector and a constant lifetime for electrons and holes, then $CCE(x)$ can be simplified to

$$CCE(x) = \frac{\mu_e \tau_e U}{L^2}\left(1 - \exp\left(\frac{xL - L^2}{\mu_e \tau_e U}\right)\right) + \frac{\mu_h \tau_h U}{L^2}\left(1 - \exp\left(\frac{-xL}{\mu_h \tau_h U}\right)\right). \tag{2.68}$$

If the charge is generated near under cathode $Q(x) = Q_0\delta(x)$, then hole contribution is negligible and only electron part in (2.68) remains, from (2.66) we get the final expression

$$CCE(U) = \frac{\mu_e \tau_e U}{L^2}\left(1 - \exp\left(\frac{-L^2}{\mu_e \tau_e U}\right)\right), \tag{2.69}$$

which is a commonly known form of the Hecht equation for one-carrier type (electrons) [73]. If the initial charge is generated by an incoming high energy particle such as a gamma photon with energy E_γ, then the initial charge is equal to

$$Q_0 = e\frac{E_\gamma}{E_p}, \tag{2.70}$$

where E_p is e-h pair creation energy. Mentioned equations allow us to obtain $\mu\tau$ product by fitting experimentally measured dependency of CCE on bias $CCE(U)$. Experimental dependence $CCE(U)$ can be obtained from measured spectra (see section 4.2), where we use the ratio of position of maximum count for bias U over the limit of the position of maximum count for large bias. Hecht equation (2.69) contains besides L only one material parameter $\mu\tau$. In the case of strongly absorbed radiation near under cathode, surface recombination may distort the

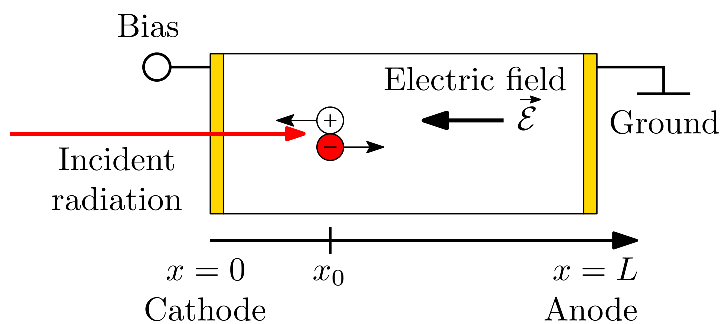

Figure 2.12: The detector scheme with generated charge at position x_0 by incident radiation.

evaluation of the Hecht equation by introducing bias dependence of the initial generated charge that gets into the bulk from the surface layer. In this case, it is impossible to separate the surface recombination from charge losses inside bulk using (2.69), and a more powerful technique needs to be used. This is also the case when one wants to separately evaluate μ and τ. More advanced methods such as L-TCT (see section 4.1) can distinguish surface recombination from charge losses inside bulk and the effect of electric field (see section 2.10). The lifetime τ is in the context of the detector with a deep trap equal to trapping time τ_T.

3. Numerical simulations

3.1 Solved equations

In this section, the studied drift-diffusion equation coupled with the Poisson equation will be analyzed. Let us write all the equations needed to study charge transport in 1D:

$$\frac{\partial n}{\partial t} = \frac{1}{e}\frac{\partial j_e}{\partial x} - \sum_i U_{ei} + I_{bb} - U_{bb} \tag{3.1}$$

$$\frac{\partial p}{\partial t} = -\frac{1}{e}\frac{\partial j_h}{\partial x} - \sum_i U_{hi} + I_{bb} - U_{bb} \tag{3.2}$$

$$j_e = -e\mu_e n \frac{\partial \phi}{\partial x} + eD_e \frac{\partial n}{\partial x}, \tag{3.3}$$

$$j_h = -e\mu_h p \frac{\partial \phi}{\partial x} - eD_h \frac{\partial p}{\partial x}. \tag{3.4}$$

$$\frac{\partial n}{\partial t} = U_{ei} - U_{hi} \tag{3.5}$$

$$U_{ei} = \sigma_{ei}\nu_{ei}\left[(N_{ti} - n_{ti})n - n_{ti}n_{1i}\right], \tag{3.6}$$

$$U_{hi} = \sigma_{hi}\nu_{hi}\left[n_{ti}p - (N_{ti} - n_{ti})p_{1i}\right], \tag{3.7}$$

$$U_{bb} = c_{bb}(np - n_i^2), \tag{3.8}$$

$$\frac{\partial^2 \phi}{\partial x^2} = -\frac{e\rho}{\varepsilon_0 \varepsilon_r}, \tag{3.9}$$

where index i represents i-th energy level, I_{bb} is interband light-induced generation rate, U_{bb} is net band-to-band recombination rate, c_{bb} is interband coupling constant (around 10^{-11} cm^2 [74]), n_i is intrinsic carrier density, other parameters were introduced at section 2.6. In continuity equation (3.1) and (3.2), the gradient in 3D was replaced by a partial derivative in 1D. In drift-diffusion equations (3.3) and (3.4), gradient was replaced by partial derivative with respect to x, and the electric field was replaced by potential using (2.21). To preserve charge neutrality of the bulk in the thermodynamic equilibrium, the space charge density ρ that which enters the Poisson's equation (3.9) must satisfy

$$\rho = p - p_{00} - (n - n_{00}) - \sum_i \left(n_{ti} - n_{t00i}\right), \tag{3.10}$$

where 00 index represents equilibrium values. Mentioned equations (3.1)-(3.10) represent a system of coupled nonlinear partial differential equations with no general analytical solution besides simple cases. There are, in general, three possible choices of variables:

1. Natural variable formulation (ϕ, n, p)
2. Quasi-Fermi level formulation (ϕ, E_{fn}, E_{fp}) see section 2.5
3. Slotboom formulation (similar to Quasi-Fermi level formulation where the electrostatic potential is included into Quasi-Fermi level, details in [75])

Normally, the quasi-Fermi level formulation is preferred in steady state simulation, and the natural variables n and p in transient simulation [75]. In this section, the natural variable formulation was used. The initial conditions for the system of equations (3.1)-(3.10) comprise initial values for the occupation of each energy level $n_{ti}(x, 0)$, initial electron and hole concentration $n(x, 0), p(x, 0)$. The boundary conditions are given by applied bias U and band bending at interface $\phi_B(0), \phi_B(L)$ (electrical contacts) and their form is $\phi(0) = \phi_B(0) - U$ and $\phi(L) = \phi_B(L)$, where L is the detector thickness.

3.2 Numerical methods

Numerical solution of equations (3.1) through (3.10) is, in general, not possible to obtain directly in one step. Instead, a nonlinear iterative method has to be used [75]. In this section, a basic overview of such a method will be shown. There are two popular methods for solving coupled systems of nonlinear partial differential equations using discretization. First is Gummel's iteration method [76], and the second is Newton's method [77]. Determining which method is more optimal for the solution is rather complicated since it depends on details related to the particular device under study. To improve numerical stability and speed of convergence, it is important to correctly choose variables in which the equations are solved [75]. Such choices of variables were mentioned in the last section 3.1. In practice, it is helpful to use normalized units and rescaled values to avoid numerical overflow caused by the limits of precision of digital decimal representation. This makes algorithms more efficient and reliable. Numerical simulations in this thesis are sorted into two categories by time scale

1. Fast dynamics (In the 10-10000 ns time scale, describing the propagation of the excited charge following the photon absorption)
2. Slow dynamics (In the range of μs-hours, describing the charge redistribution on defect levels leading to the charging of the detector bulk and the appearance of polarization)

Fast dynamics uses a more precise scheme, but it requires small time steps and is thus impractical in simulations at minutes or hours time scale. More details about fast dynamics in [75, 78, 79]. Slow dynamics with non-equilibrium trap occupancy was solved in [62, 80], where drift-diffusion and Poisson's equations were solved numerically in one dimension. In this thesis program based on this technique is used to simulate charge transport in a detector under various conditions, such as continuous light, X-ray, or laser pulse illumination with different biases. These numerical simulations are applied to fit experimental data and obtain detector parameters such as drift mobility, electric field profile, space charge distribution, and energy parameters of energy levels. The solution of fast dynamics can often

be simplified and, under certain conditions (that will be mentioned later in this thesis), sped up by using Monte Carlo simulations that are more stable and faster.

3.3 Monte Carlo simulation

3.3.1 Concept of Monte Carlo simulation

The numerical simulation of charge transport equations using discretization techniques was described in the previous chapter 3.2. The main disadvantage of these techniques is the potential numerical instabilities in solutions. They can emerge during iterative steps when the time step or mesh size is not small enough. Decreasing the time step and the mesh size makes the simulation more precise and stable. However, the evaluation time rapidly increases, and the simulation becomes computationally intensive, thus preventing practical usage. To mitigate these problems, we can use Monte Carlo (MC) simulation, based on random number generation, to simulate charge transport. MC simulation has inherent numerical stability because it relies on random sampling and statistical methods rather than solving complex equations or performing iterative calculations. MC simulation is a powerful numerical technique widely used in many fields due to its numerical stability and ability to handle complex systems [65, 81]. In this thesis, one-dimensional MC simulation of the motion of photogenerated charge carriers developed in [82] is improved to include the SRH model and arbitrary electric field profile. This MC simulation is based on the phenomenological concept shown in [83]. The simulation is based on splitting the total photogenerated charge Q_0 in the detector into $\mathcal{N}$ superparticles that have charge

$$q = \frac{Q_0}{\mathcal{N}}. \tag{3.11}$$

These superparticles move under an applied electric field and can be in either a free state or a trapped state. Superparticle with index i that is in free state moves at calculation time t_k from position $x_i(t_k)$ during time step Δt into position

$$x_i(t_k + \Delta t) = x_i(t_k) + \Delta x_i, \tag{3.12}$$

where distance Δx_i is given by

$$\Delta x_i = \mu \mathcal{E}(x_i(t_k))\Delta t + u, \tag{3.13}$$

here u represents diffusion offset randomly sampled from the distribution

$$\mathcal{P}(u) = \frac{1}{\sqrt{4\pi D \Delta t}} \exp\left(-\frac{u^2}{4D\Delta t}\right), \tag{3.14}$$

where D is the diffusion coefficient given by the Einstein relation (2.6). Repeated application of offset u results in the broadening of carrier cloud approximating diffusion. Superparticles that are trapped do not move $\Delta x_i = 0$. Superparticles can simulate either electrons or holes, which defines their corresponding values of transport parameters, i.e., drift mobility and diffusion coefficient. If $x_i + \Delta x_i \geq L$ or $x_i + \Delta x_i \leq 0$, the superparticle is collected on an electrode and no longer contributes to the simulation. To include surface recombination into MC simulation,

we use equation (2.63) to calculate Q_0 in (3.11). This simplifies and speeds up MC simulation compared to [83] by removing the surface region from the calculation and requiring only one region - the bulk. Equation (3.13) represents discretization of drift-diffusion equation (2.14) for constant temperature. Superparticles that drift ($\Delta x_i \neq 0$) contribute to total induced current

$$I(t_k) = \sum_{i=1}^{\mathcal{N}} \frac{q\Delta x_i}{L\Delta t}, \tag{3.15}$$

where the Shockley-Ramo theorem (see section 2.8) is used. To simulate charge trapping and detrapping, the SRH model is used (see section 2.6). To calculate the probability p_F that a free superparticle at time t_k remains free for additional time Δt is

$$p_F(\Delta t) = \exp\left(-\frac{\Delta t}{\tau_T}\right), \tag{3.16}$$

where τ_T is the total trapping time given by

$$\frac{1}{\tau_T} = \sum_{J=1} \frac{1}{\tau_{TJ}}, \tag{3.17}$$

where τ_{TJ} is the trapping time of the J-th trap level. If the superparticle is trapped at time t_k, then the probability of it remaining trapped for additional time Δt is

$$p_{DJ}(\Delta t) = \exp\left(-\frac{\Delta t}{\tau_{DJ}}\right), \tag{3.18}$$

where τ_{DJ} is detrapping time of J-th trap level. Trapping and detrapping time corresponds to SRH trap parameters via equations (2.53) and (2.54). The direct transition between trap levels is not assumed. The new state of the superparticle is determined according to its current state and trapping/detrapping probability. This procedure is repeated until the required duration of the simulation is reached. More details about trapping and detrapping probability calculation are in [84]. We assume the photogenerated charge is small enough not to significantly influence the internal electric field (testing probe charge). This allows us to separate the simulation of long-term detector polarization from short-transient effects. Because the charge is small, trap level occupancy does not change during MC simulation (but is position dependent). Since shallow levels do not significantly contribute to space charge, their effect can only be included in MC simulation and not in long-term polarization simulation. The only effect included in long-term simulation is effective mobility caused by shallow traps. Effective mobility directly results from charge carriers being trapped for some time and then detrapped. If this occurs many times in the studied time frame, then charge carrier drift with effective mobility [84]

$$\mu_{eff} = \mu \frac{\tau_T}{\tau_T + \tau_D}. \tag{3.19}$$

This decoupling of shallow traps from long-term simulation speeds up the simulation, allowing practical usage of long-term simulations. The electric field is obtained from the long-term simulation described in section 3.2.

The basic concept of Monte Carlo simulation is shown in figure 3.1, where the detector cross section is shown in two time steps. First time $t = 0$ where photogenerated carriers are near under the electrode. Second is time t_k, where carriers drifter through the bulk, some get trapped in deep level (marked green), and free carriers are marked red. In figure 3.2, CWF corresponds to simulation in 3.1, the CWF shows typical exponential decay of current after initial spike corresponding to photo generating short pulse, the end of CWF has diffusion broadening around transit time, which marks the arrival of the center of carrier cloud.

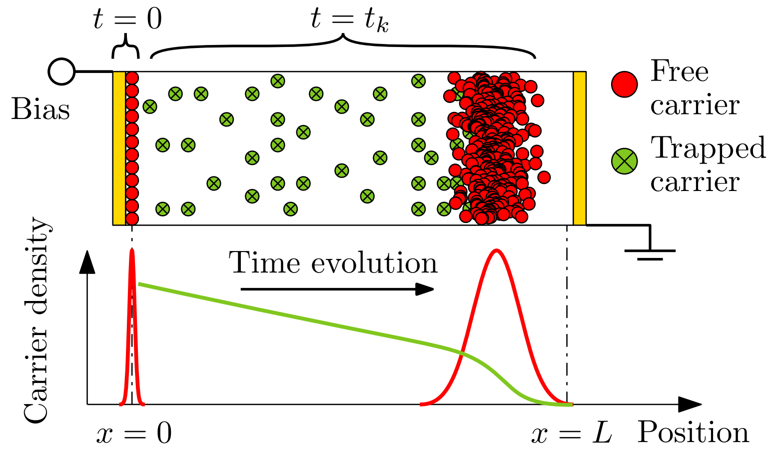

Figure 3.1: Basic concept of Monte Carlo simulation.

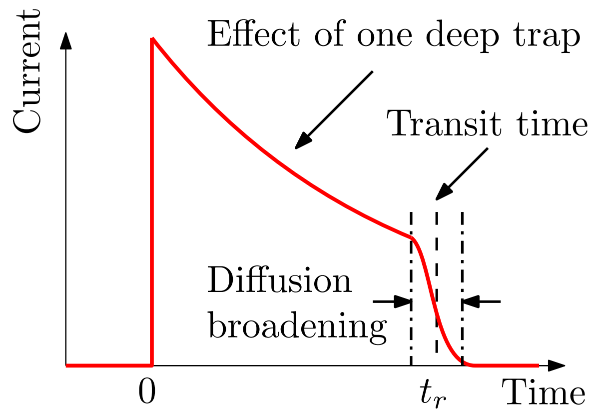

Figure 3.2: Simulated current waveform of detector with one deep electron trap.

3.3.2 Stability of Monte Carlo simulation

In this section, the stability and dependence of MC simulation on the time step and the number of superparticles will be shown. MC simulation's inherent numerical stability is caused by random sampling and statistical methods rather than solving complex equations or performing iterative calculations. It is remarkable how simulation with even a few superparticles gives a rather good simulation result. In figure 3.3, there is the dependence of simulated MC electron CWFs for a detector with $L = 0.2$ cm, $U = 200$ V, $\tau_T = 1$ μs with no space charge, for an increasing number of superparticles from 1 to 5000, it can be seen that for one superparticle (red), the current stops at time $t = 140$ ns, before the transit time $t_r = 200$ ns, this is caused by trapping of superparticle on the deep trap, and since there is only one superparticle in the simulation, the current stops. For 8 and 32 superparticles (blue and green curves), the general exponential decay shape starts to emerge, and transit time is almost correct. For as little as 128 superparticles, the general exponential decay is close to the exact solution with visible noise given by the low number of superparticles where even small fluctuations in trapped particles generate significant noise. For more than 2000 superparticles (lime and orange curves almost overlap), the CWF has the correct shape and almost no visible noise. This demonstrates the main advantage of MC simulation, which is fast convergence to correct values as the number of simulated particles increases. In the case of small signals under which the internal electric field is not disturbed by the drifting charge, the superparticles do not interact with each other. The simulation can be run in parallel, either on CPU or GPU, to significantly shorten the time needed to finish the simulation. More details about small and large signals and how to include the effect of large signals in MC simulation are in [85, 86].

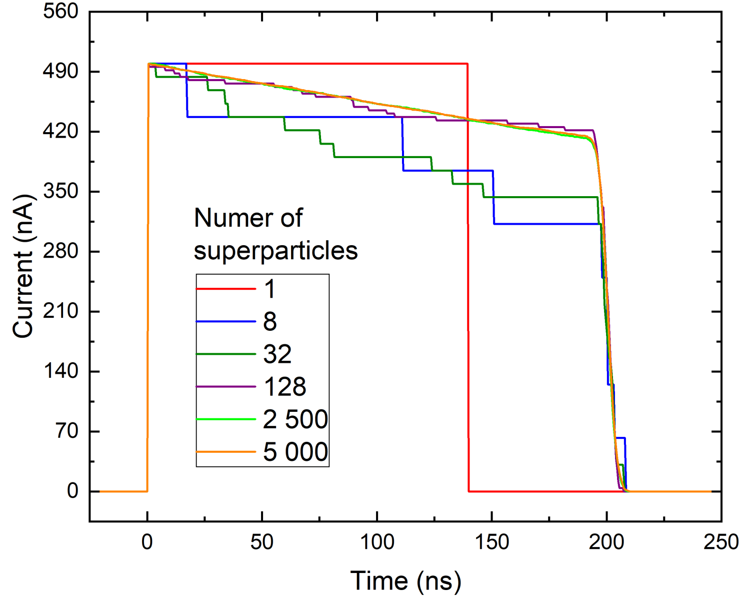

Figure 3.3: Dependence of MC simulation on the number of super particles.

MC simulation is sensitive to time step size. The effect of varying time step size on simulation with 5000 superparticles and with parameters mentioned previously in this section is shown in figure 3.4, where time step size from 1 ns to 100 ns is shown. If the time step $\Delta t \ll$ than any time parameter in simulation such as τ_T, τ_D, t_r, then the simulation is valid, this condition is fulfilled for $\Delta t < 5$ ns in shown simulation. If the time step size increases, the number of steps decreases, and each particle drifts on each step a larger distance, thus worsening the spatial resolution. The lower number of steps also affects diffusion since many diffusion offsets are needed to simulate diffusion properly (see equation (3.14)). The exact choice of the number of particles and time step size depends on the studied problem and is not easily generalized.

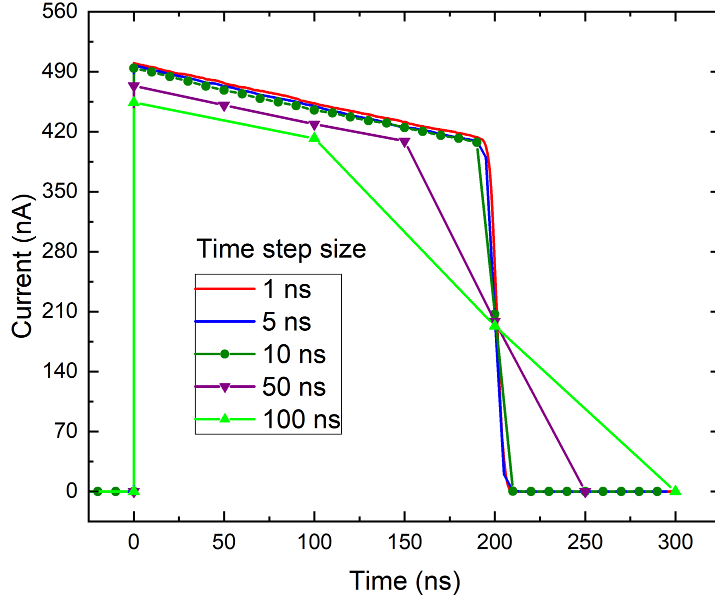

Figure 3.4: Dependence of MC simulation on time step size. It can be seen that time step shorter than 10 ns is needed to simulate CWF correctly. CWF for 50 ns (purple) and 100 ns (lime) have decreased amplitude to better show discrete steps.

3.3.3 Examples of Monte Carlo simulations

In this section, basic examples of detector polarization and resulting CWFs will be shown. A typical example is CZT detector polarization at room temperature $\mathcal{T} = 295$ K. We simulate a detector with one deep electron trap level with concentration $N_t = 1.0 \times 10^{11}$ cm^{-3}, $\sigma_e = 1.0 \times 10^{-13}$ cm^2, $E_t = E_C - 0.775$ eV. The trap is located on the Fermi level, which is set to the middle of band gap $E_F = E_C - E_g/2, E_g = 1.55$ eV (see figure 3.5). Detector thickness $L = 0.2$ cm. Electron and hole drift mobility $\mu_e = 1000$ cm^2/Vs, $\mu_h = 80$ cm^2/Vs. We use two electrical contact configurations. The anode is always flat-band Ohmic with no band bending. In the first case, the cathode is blocking Schottky contact with band bending +150 meV, and in the second case, the cathode is injecting Ohmic contact with band bending −90 meV. In the first case, electron depletion in the detector results in positive space charge accumulation. In the second case, electron injection leads to electron accumulation on the trap level, forming a negative space charge. The band diagram of the first case of electrical contacts is in figure 3.6, and the second is in figure 3.7. The simulation is based on the numerical solution of coupled drift-diffusion equation with the Poisson's equation (see section 3.2), from which the electric field, space charge density, trap occupancy, quasi-Fermi levels are obtained. These parameters enter the MC simulation, which yields the CWFs.

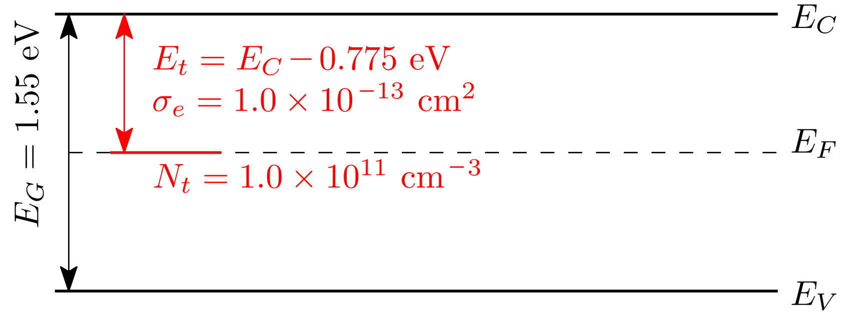

Figure 3.5: Band diagram of electron trap level used in simulation.

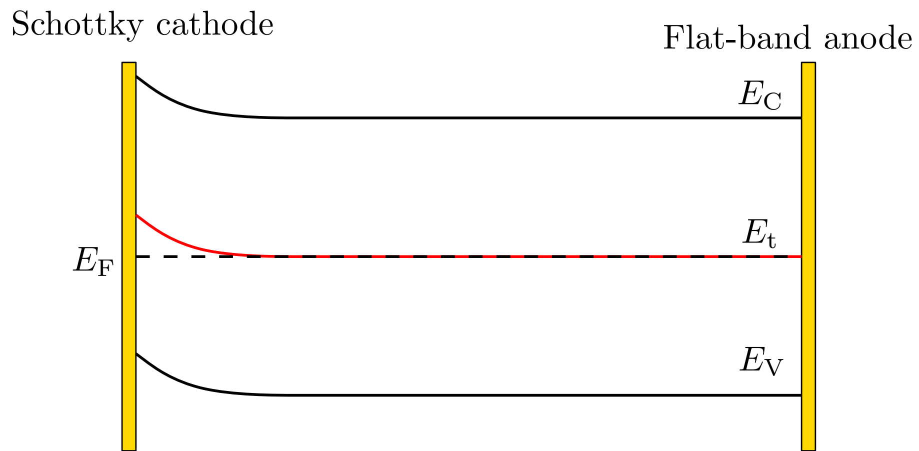

Figure 3.6: Band diagram of the detector with flat-band anode and depleting Schottky cathode.

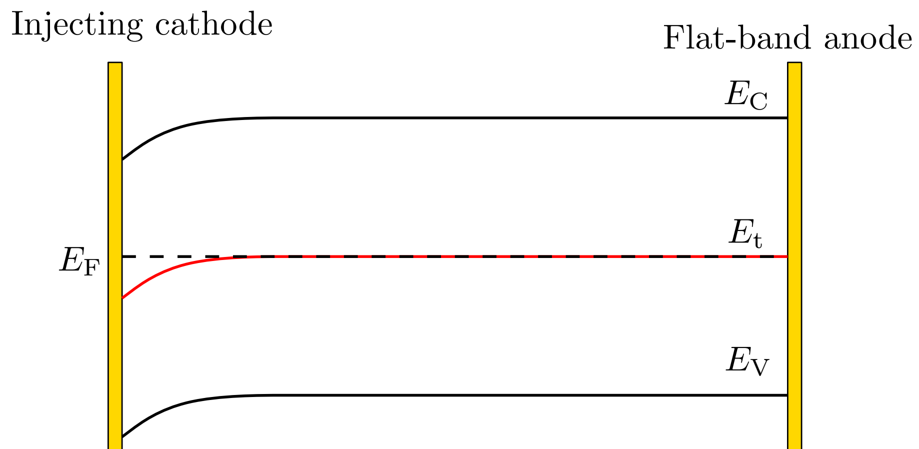

Figure 3.7: Band diagram of the detector with flat-band anode and injecting Ohmic cathode.

3.3.3.1 Electron depletion

In this part, electron depletion resulting from Schottky cathode with band bending +150 meV is simulated (see figure 3.6). The simulated electric field for electron depletion is shown in figure 3.8, where electric field for applied continuous DC bias in the range 50 − 500 V is shown. The electric field has the largest magnitude at the cathode and decreases towards the anode. For biases lower than 170 V, there is a inactive layer inside the detector which is the area where the electric field is almost zero. For biases greater than 170 V, the electric field is large enough to overcome the positive space charge, and complete depletion of the detector occurs. The corresponding space charge is shown in figure 3.9, where a nearly constant space charge is present in the whole detector for biases greater than 170 V, and for lower biases, the space charge drops to zero in the inactive layer. The time evolution of the electric field for bias 50 V is shown in figure 3.10. The detector without bias is not polarized and has no space charge. Shortly after the bias is applied, the detector starts to polarize, and the electric field warps. At the time around 3 s, the electric field at the anode is almost zero, and the inactive layer forms. After that, the inactive layer expands until the trap is depleted, and the inactive layer stabilizes after 30 s. The space charge is shown in figure 3.11, where it can be seen that the space charge increases first in the whole detector until the inactive layer forms, and then the space charge increases only in the depleted part of the detector and decreases in the inactive layer. The waves in space charge, visible for time 4, 8, 15 s, are caused by inactive layer discharging of previous space charge under almost zero electric field, at time greater than 15 s, the waves disappear and inactive layer stabilizes. It is useful to define mean space charge density ρ_{mean} as

$$\rho_{mean} = \frac{1}{L}\int_0^L \rho(x)\mathrm{d}x, \tag{3.20}$$

where $\rho(x)$ is space charge density at position x. Evolution of mean space charge density ρ_{mean} inside detector is shown in figure 3.12, where saturation of mean space charge is visible. CWFs for the DC bias are shown in figure 3.13, where charge trapping and electric field cause almost exponential current decay. For biases greater than 170 V, the CWFs have visible finite transit time, and for lower biases, the electron cloud never reaches the anode because of the inactive layer presence. This is important for the experimental evaluation of CWFs from which the electric field and space charge density is obtained by fitting CWFs with MC simulation. The time evolution of CWFs for bias 50 V is shown in figure 3.14. Shortly after applying bias 50 V, the current waveform decays only because of charge trapping since the electric field is almost constant in the non-polarized detector. As the time after applying the bias increases CWFs decay faster until the transit time disappears at 3 s after the bias is applied. This was observed and studied in [37, 83, 87].

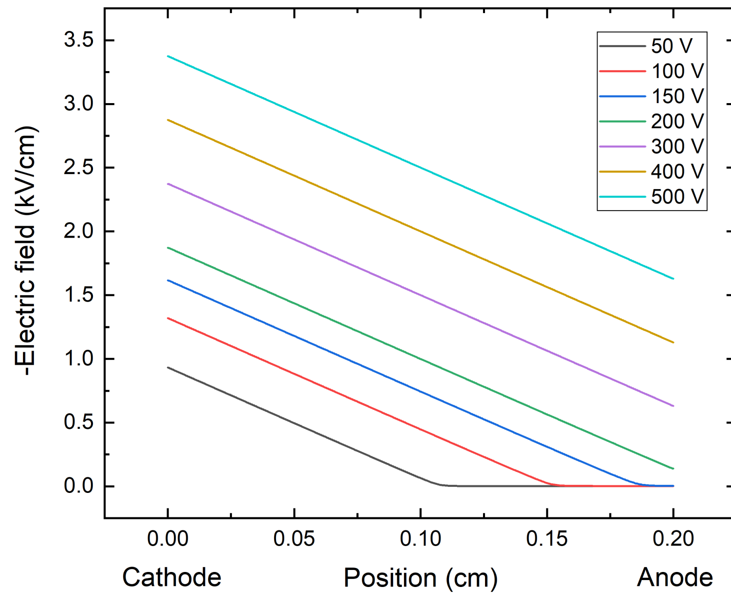

Figure 3.8: Electric field profile for detector with electron depletion under different DC biases.

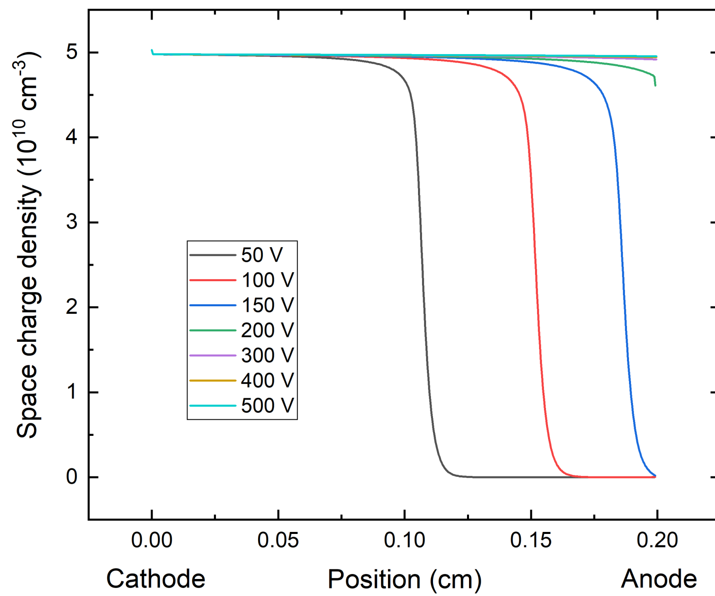

Figure 3.9: Space charge density for detector with electron depletion under different DC biases.

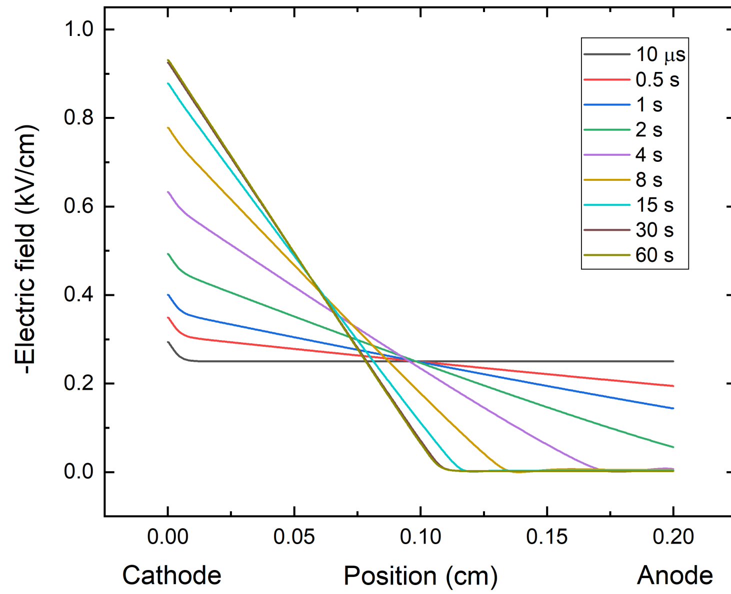

Figure 3.10: Time evolution of electric field profile for detector with electron depletion for bias 50 V.

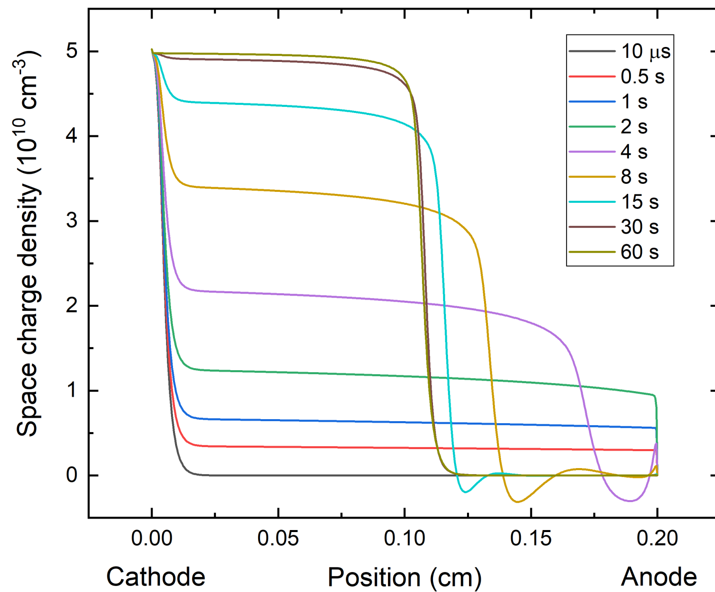

Figure 3.11: Time evolution of space charge density for detector with electron depletion for bias 50 V.

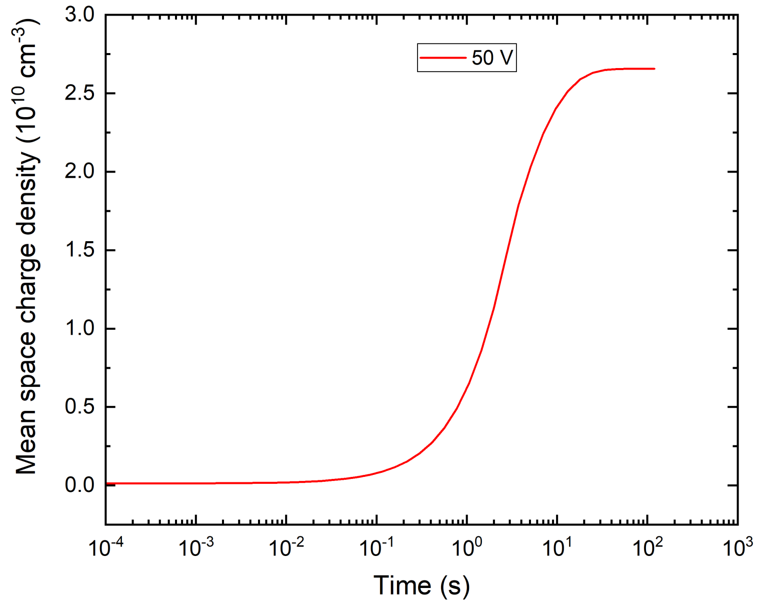

Figure 3.12: Time evolution of the mean space charge density for the detector with electron depletion for bias 50 V.

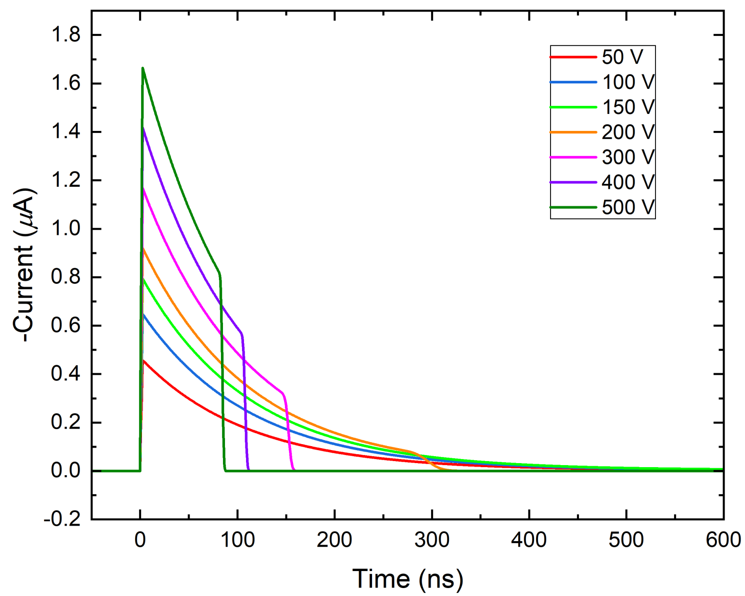

Figure 3.13: CWFs for detector with electron depletion for several DC biases.

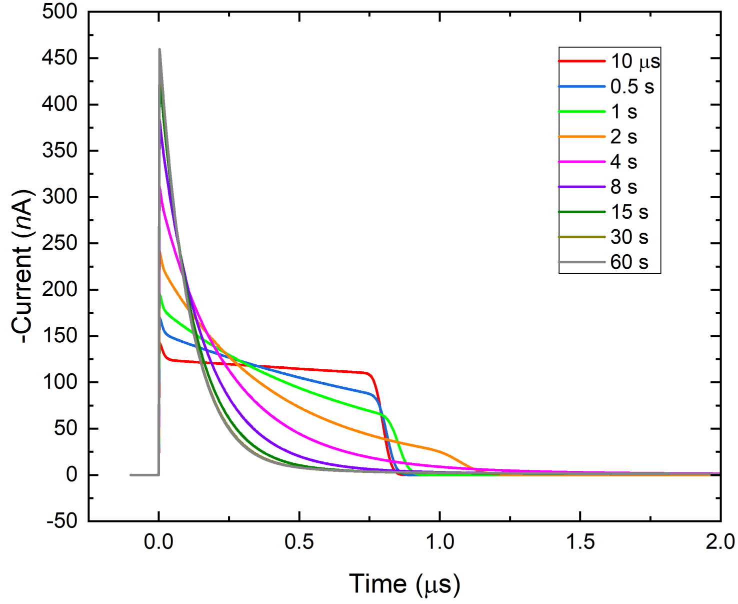

Figure 3.14: Time evolution of CWFs for detector with electron depletion for bias 50 V.

3.3.3.2 Electron injection

In this part, electron injection resulting from injecting Ohmic cathode with band bending -90 meV is simulated (see figure 3.7). The simulated electric field for electron injection is shown in figure 3.15, where electric field for applied continuous DC bias in the range $50 - 500$ V is shown. The electric field has the largest magnitude at the anode and decreases towards the cathode. For biases lower than 200 V, the electric field starts to bend near the cathode because of the space charge limited current regime in which the electric field self-limits the injection that causes the negative space buildup. More details about space charge limited currents are in [87]. This leads to stable, almost zero bias under the cathode. For biases greater than 300 V, the electric field is large enough to overcome space charge, and an almost constant space charge is formed inside the detector, which corresponds to almost linear electric field profile in figure 3.15 for biases $>$ 300 V. The corresponding space charge is shown in figure 3.16, where the space charge has maximum amplitude under the cathode and decreases towards the anode. For biases greater than 300 V, the space charge is almost constant in the whole detector. Time evolution of the electric field for bias 50 V is shown for the time from 10 μs to 100 ms in figure 3.17 and from 100 ms to 10 s in 3.18. The detector without bias is not polarized and has no space charge. Shortly after the bias is applied, the detector starts to polarize, negative space charge forms, and the electric field warps. At around 50 ms, the electric field at the cathode is almost zero, and electron injection is suppressed. This stabilizes the space charge. The space charge for the time from 10 μs to 100 ms is shown in figure 3.19 and from 100 ms to 10 s in figure 3.20, where it can be seen that the space charge spreads from the

cathode towards the anode as the time after the bias is applied increases. In the time range from 100 ms to 10 s, the space charge redistributes itself and stabilizes around 3 s. The redistribution is caused by retrapping of electrons combined with an almost zero electric field under the cathode that limits injection. The time evolution of mean space charge density ρ_{mean} (defined in equation (3.20)) for bias 50 V is shown in figure 3.21, where the initial increase of mean space charge amplitude is visible, followed with redistribution that decreases mean space charge density and saturation around 5 s. CWFs for the DC bias are shown in figure 3.22, where CWF increases as a result of increasing electric field towards the anode. For biases greater than 200 V, the CWFs have distinct transit time, and for lower biases, the electron cloud is highly broadened by the low electric field under the cathode. The time evolution of CWFs for bias 50 V is shown in figure 3.23. Shortly after applying bias 50 V, the current waveform decays only because of charge trapping since the electric field is almost constant in the nearly non-polarized detector. As the time after applying the bias increases, CWFs increase as the effects of the electric field overcome the effect of trapping on CWF shape. The analogical regime where space charge is formed by hole injection from the anode is experimentally demonstrated for CZTS and studied in section 5.3.

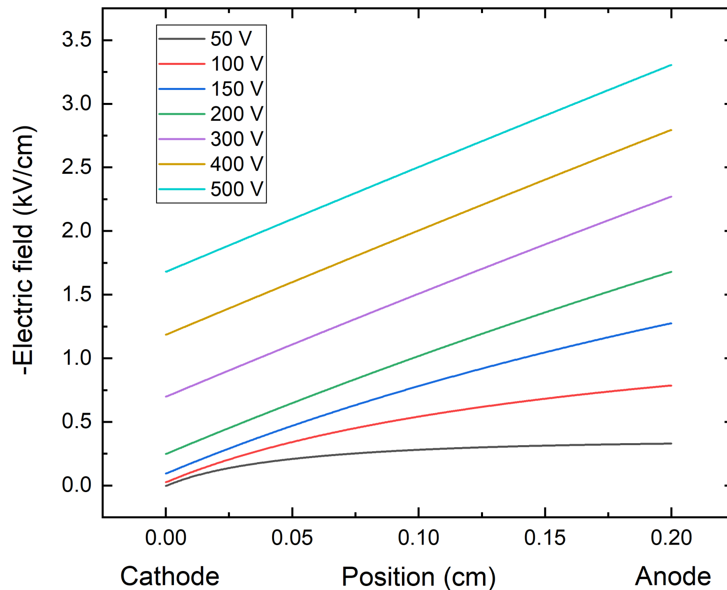

Figure 3.15: Electric field profile for the detector with electron injection under different DC biases.

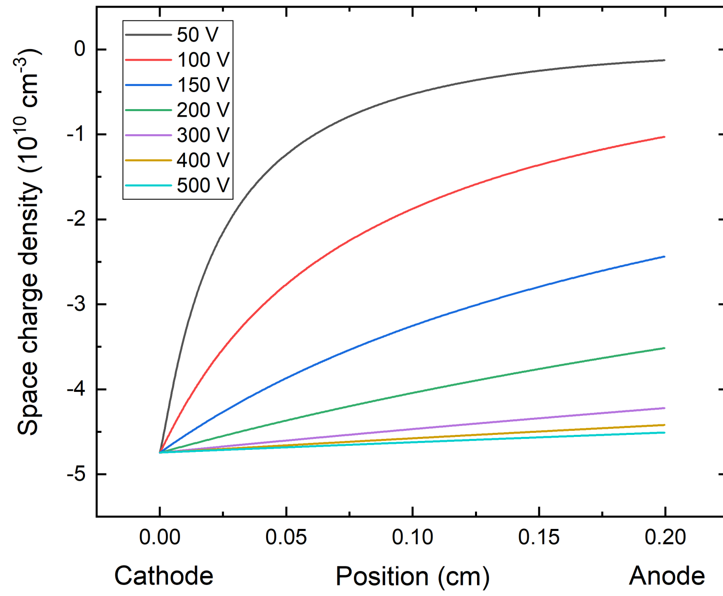

Figure 3.16: Space charge density for the detector with electron injection under different DC biases.

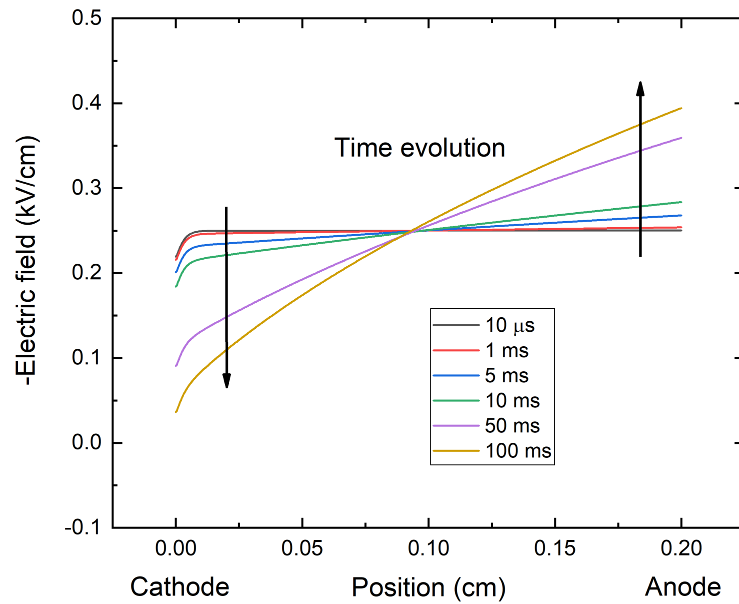

Figure 3.17: Time evolution of electric field profile for the detector with electron injection for bias 50 V from 10 μs to 100 ms.

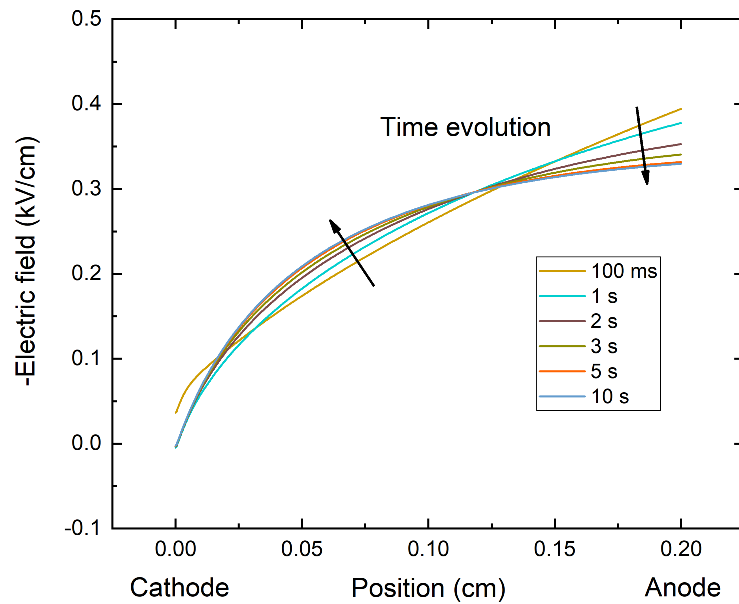

Figure 3.18: Time evolution of electric field profile for the detector with electron injection for bias 50 V from 100 ms to 10 s.

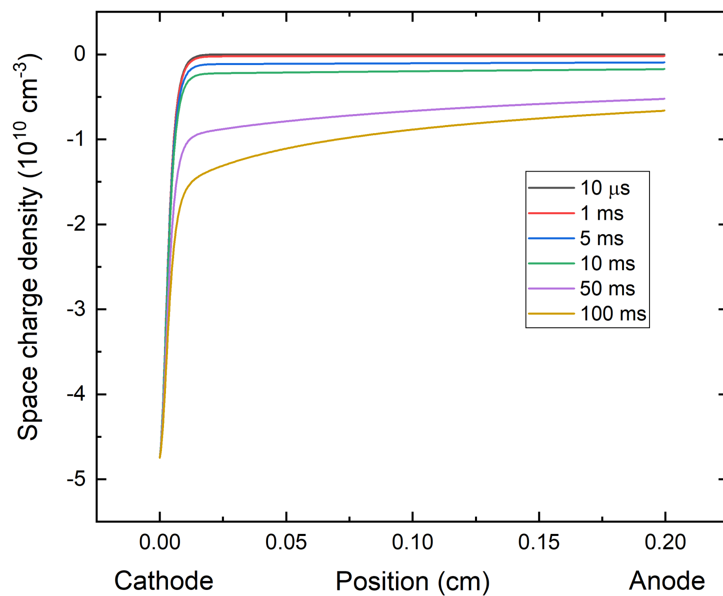

Figure 3.19: Time evolution of space charge density for the detector with electron injection for bias 50 V from 10 μs to 100 ms.

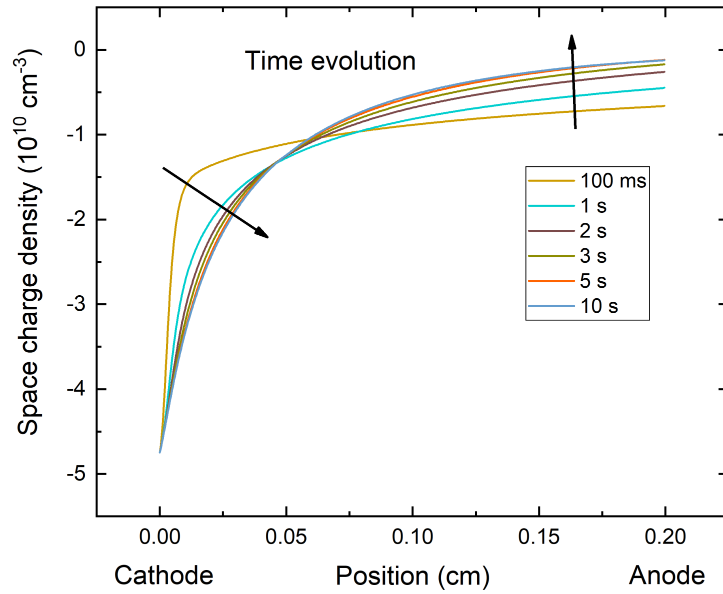

Figure 3.20: Time evolution of space charge density for the detector with electron injection for bias 50 V from 100 ms to 10 s.

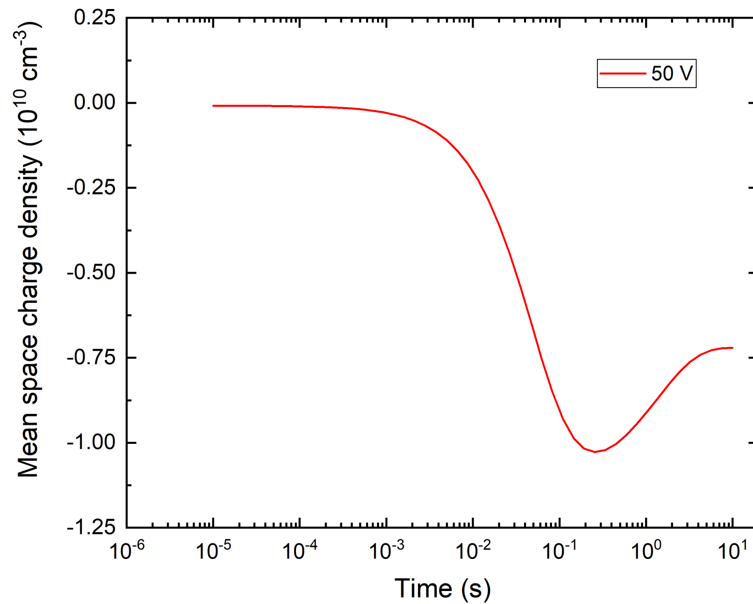

Figure 3.21: Time evolution of the mean space charge density for the detector with electron injection for bias 50 V.

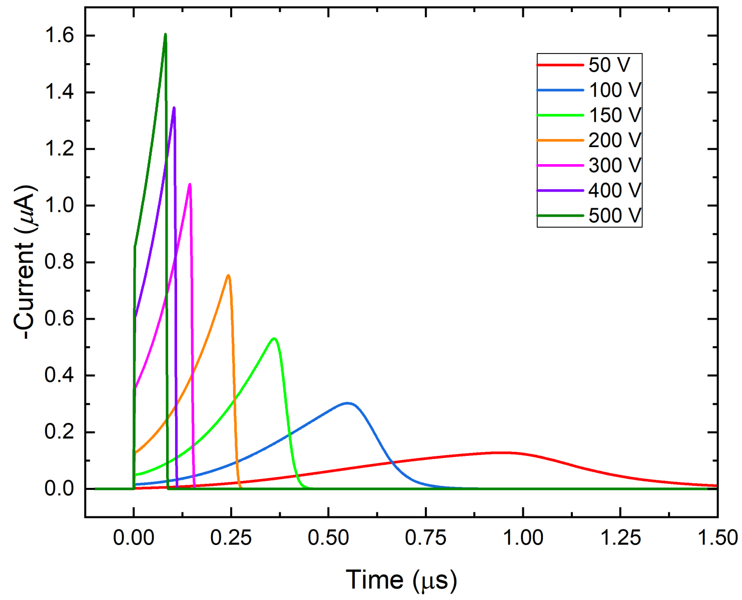

Figure 3.22: CWFs for the detector with electron injection for several DC biases.

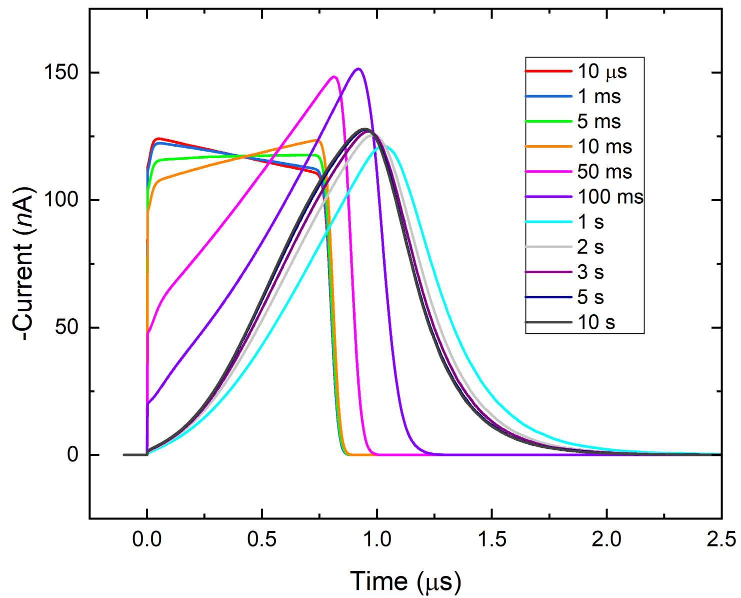

Figure 3.23: Time evolution of CWFs for the detector with electron injection for bias 50 V.

4. Experimental techniques

4.1 Transient Current Technique

The Transient Current Technique (TCT) is the primary experimental technique used in this thesis. It belongs to the family of Time-of-Flight methods based on measuring the current response of the semiconductor detector to the external event, which allows studying of charge transport in semiconductor detectors. In the case of the Laser-induced Transient Current Technique (L-TCT), the external photo-generating source is above band gap laser pulse, which is strongly absorbed and generates electron-hole e-h pairs near under the illuminated electrode [88]. Electron-hole pairs are separated by the electric field generated by applied bias. The generated carriers drift to their corresponding electrodes, moving charge induces current transients based on Shockley-Ramo theorem (see section 2.8). Since L-TCT measurements result in a current waveform, much more information about charge transport can be obtained. The possibility of triggering on a laser pulse significantly decreases noise compared to untriggered sources like an alpha particle because of the repeatable and identical initial conditions of each successive laser pulse. The resulting CWFs are accumulated for pulse processing. Precise triggering allows more sophisticated bias and laser pulse schemes. Evaluated information includes internal electric field, carrier drift mobility, CCE, and parameters of trap levels. The detector has a rectangular shape with two planar opposite electrodes. The basic principle of L-TCT is shown if figure 4.1, where the laser pulse arrives from the left into the center of the illuminated cathode. Holes are immediately collected while electrons drift into bulk. Their movement induces an electric current in the collecting electrode. This electric current is amplified using a current amplifier and measured on a digital sampling oscilloscope. The laser pulse intensity is chosen as low as possible to have a small photogenerated charge that does not significantly change the electric field profile and acts as a probe. We can also use additional illumination, which is shown in figure 4.1 with red LED, which can either be turned off or used to illuminate the cathode, anode, or both to further study detector polarization.

The experimental setup used in this thesis comprises above band-gap pulsed laser diode (660 nm wavelength, 300 mW maximum pulse peak power, 1 ns pulse width as FWHM), which is powered by Picosecond Lab pulse generator with repetition rate (1 Hz – 100 kHz), high-frequency voltage amplifier (L–3 Narda–Miteq AM–1607–3000) and ultrafast digital sampling oscilloscope (LeCroy WaveRunner 640Zi, 40 Gs/s, resolution up to 11 bits, 4 GHz bandwidth, DC input impedance). We use a red LED with 660 nm wavelength for the continuous additional illumination. For more detail on setup, see [89]. An in-house made bias switching unit generates bias pulses, which are synchronized with laser pulse using function generator (AFG3252, sampling rate 2 GS/s). In our configuration, the bias is applied to the illuminated electrode, and depending on polarity, we can study either electron or hole CWFs. Laser pulse delay (LPD) after the rise time of bias pulse can be varied, which allows observing the formation of space charge inside the detector. Depolarization time (DT), that is, the time when no bias is applied to the detector, is needed for depolarization of the detector. Bias pulse

width (BPW) is short enough to allow depolarization and identical conditions for every period. The dynamics of the space charge formation is derived through the Gauss's law. Assuming the charge neutrality of the sample's bulk at the thermodynamic equilibrium, the short LPD assures that there is not enough time for the development of the space charge in the detector within the single bias pulse. Simultaneously, the residual space charge that could appear during the pulse is drained away at the DT period and the memory effect induced by the cross-talk between bias pulses is suppressed.

The scheme of the laser pulse and bias pulse relative position is shown in figure 4.2. The transfer function of the used electronic circuit systematically distorts measured current waveforms. The deconvolution procedure is used to obtain the original current waveforms. Details of the deconvolution procedure are discussed in [89].

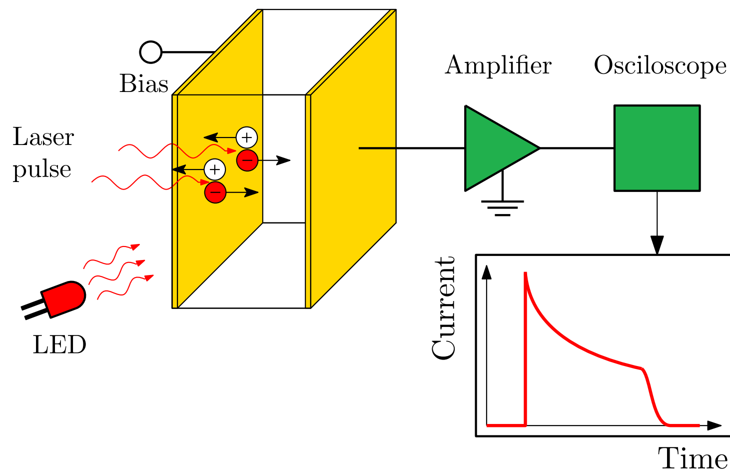

Figure 4.1: Scheme of the L-TCT setup.

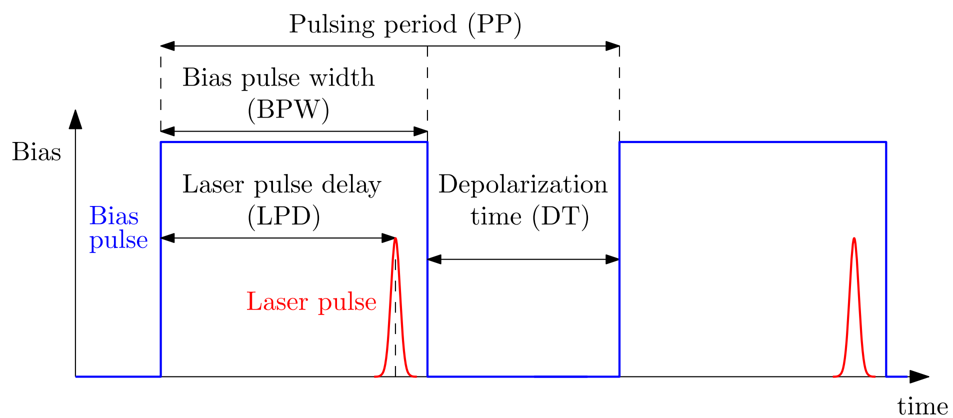

Figure 4.2: Scheme of the bias pulsing.

4.2 Spectroscopic measurements

Spectroscopic measurements allow us to directly study the performance of detector charge collection efficiency and spectral resolution. Radiation detectors can operate in several regimes, of which the most often is the pulse mode. In this regime, the detector records each quantum of radiation which generates e-h pairs inside the detector bulk [57]. Pulse processing comprises the accumulation of many events that are amplified, shaped, and analyzed. Incoming radiation quanta induce a current in the detector, which is integrated into the charge, which is amplified in charge sensitive pre-amplifier and produces voltage step V_{max} proportional to the charge. The voltage step is reshaped and further amplified by shaping amplifier, which converts the voltage step with variation δV into Gaussian with its center V_{max} with the full width at half maximum FWHM $= \delta V$. The output of the shaping amplifier is processed in a multi-channel analyzer (MCA) and recorded in a computer. The scheme of the spectroscopic measurement for a detector with two planar opposite electrodes is shown in figure 4.3. The experimental setup consists of a vacuum chamber (to prevent loss of energy of radiation source for alpha particles), an in-house created pre-amplifier based on Amptek A250 pre-amplifier, shaping amplifier Ortec 671, multi-channel analyzer Ortec MCA easy, voltage source Iseg SHQ 122M and computer with an in-house created program for complex spectra evaluation. The detector is placed inside the vacuum chamber with the radiation source pointing at the cathode. Spectroscopic measurements are evaluated using the Hecht equation (see section 2.11 and equation (2.69)).

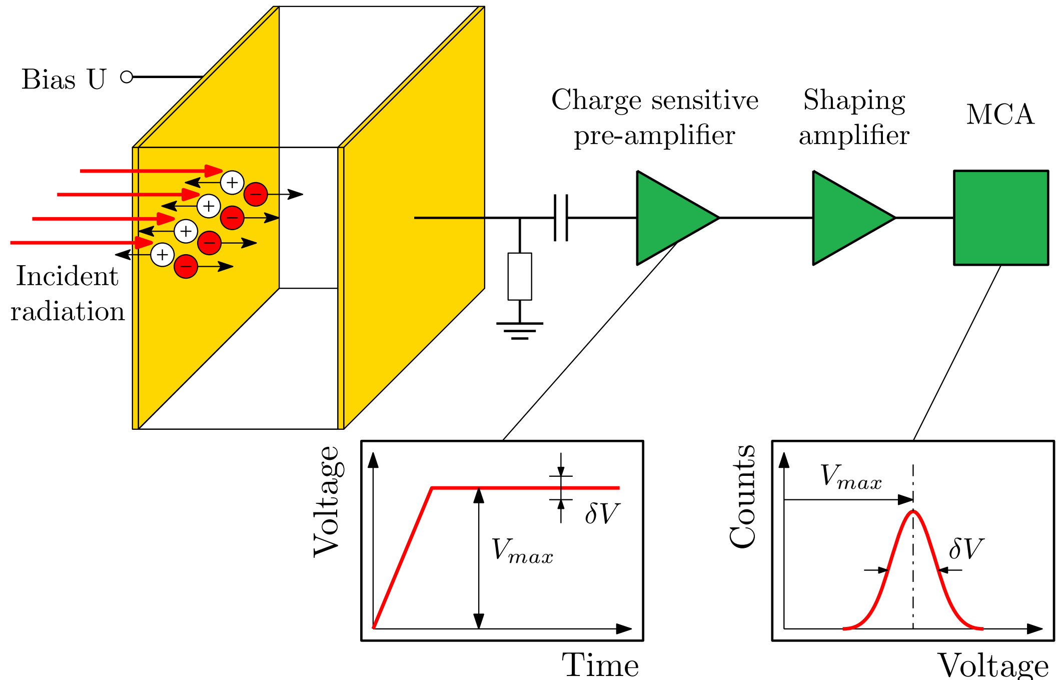

Figure 4.3: Scheme of the setup for radiation spectra measurement [90].

5. Results and discussion

5.1 GaAs

In this section, we investigate GaAs:Cr sensors by L-TCT at pulsed and DC biasing. We focus on the evolution of CWFs in the time interval 0.1–5 ms after switching on the bias. Pulsed bias allowed us to suppress the space charge formation and to study charge trapping effects on the current waveforms, thus enabling easier evaluation of the electron drift mobility carrier trapping and detrapping times. The proposed procedure for determining the basic characteristics of the detectors using L-TCT is based on our long-term experience with the development of this technique and the characterization of a number of SI CdZnTe and perovskite samples [89, 91, 92, 93].

Observed effects are successfully explained by the model of spatially variable hole conductivity induced by Cr diffusion. Simultaneously, we evaluate the electron lifetime, electron drift mobility, charge collection efficiency, the evolution of the internal electric field, and space charge formation. CWFs are analyzed by MC simulations (see section 3.3). Specific profile of the electric field, the spreading of drifting cloud of electrons by diffusion, and surface recombination are newly involved in the simulations. Carrier trapping and detrapping are described by appropriate spatially and temporary constant trapping time τ_T and detrapping time τ_D (see subsection 2.6.2). The presented model consistently describes all observed phenomena and their conformity with experimental data.

Three planar detectors with the dimension 5 mm $\times$ 5 mm and sample thickness $L = 0.5$ mm and one Hall bar sample with the dimensions 3 mm $\times$ 15 mm $\times$ 0.5 mm were used for detailed characterization of the material by measuring L-TCT and galvanomagnetic properties, respectively. Planar detectors exhibited very similar behavior. Therefore we present results obtained on one selected detector. Samples were cut from the SI GaAs:Cr single crystal wafer, which was prepared at the Tomsk State University in Russia by the Cr in-diffusion to both surfaces of the LEC GaAs wafer [17, 20]. Samples were mechanically polished using 1 μm Al_2O_3 in aqueous suspension, and Au/GaAs/Au contacts were prepared by the evaporation. Room temperature bulk resistivity $\rho_0 = 2 \times 10^9$ Ωcm was deduced from the Hall effect measurement. The negative sign of the Hall coefficient, together with rather low room temperature Hall mobility 1700 cm^2/Vs indicate the mixed type of conductivity [94] and an important role of holes in the charge transport. Such findings are in agreement with previously published data [17].

TOF transient currents were excited through the semitransparent detector's cathode by the pulsed laser diode with the above band-gap light at the wavelength 660 nm, which is absorbed in an attenuation length $l \approx 1$ μm [95] under the cathode. The laser pulse FWHM was ≈ 0.5 ns. A neutral density filter was used for the laser intensity attenuation to suppress the contribution of photo-generated carriers to the electric field warping and the space charge formation. Photo-generated electrons created near the cathode drift under the bias toward the anode and induce the transient current. The output current is amplified by the bipolar high-frequency amplifier and recorded by a digital sampling oscilloscope

(see section 4.1). Holes are immediately collected at the cathode. Their relative contribution to the collected charge calculated according to the Shockley-Ramo theorem (see section 2.8) for the planar sample as $l/(L-l) \approx 0.002$ is very low, and the effect of holes may be thus neglected. Evolution and shape of all CWFs were analyzed using MC simulations.

5.1.1 Results

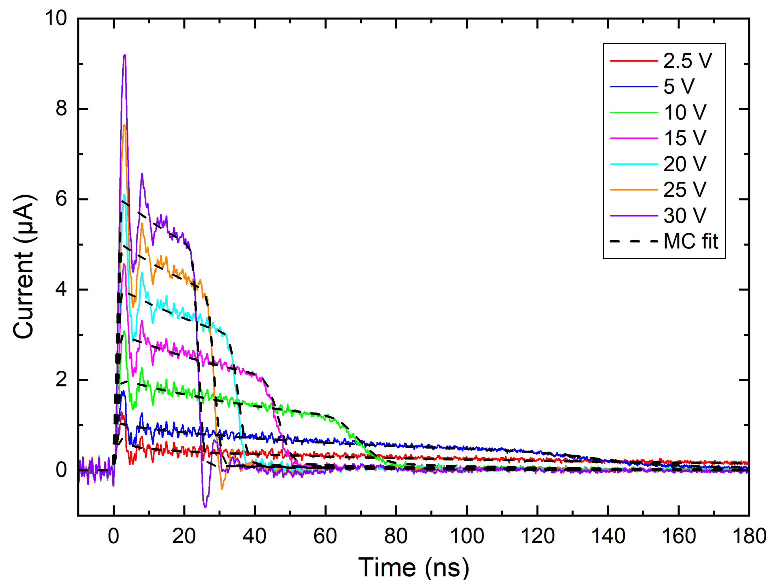

Figure 5.1: Bias dependence of electron current waveforms measured by the L-TCT at pulsed bias according the scheme in figure 4.2. Dashed lines represent the MC fit with the model of the constant internal electric field.

Figure 5.1 shows bias dependence of electron CWFs measured in the planar GaAs:Cr detector using pulse biased L-TCT, where pulsed bias parameters LPD = 80 μs, BPW = 10 ms and DT = 10 ms were chosen. No visible changes were observed at the CWFs for LPD < 150 μs or $DT > 10$ ms. We can thus consider the detector unpolarized, i.e. with constant electric field distributed within the whole sample shortly after biasing. Consequently, the slope of CWF is affected only by the photo-electron trapping and recombination [37]. The sharp drop of CWFs corresponding to the transit time of electrons drifting toward the anode was determined for the first time in this material. We also observed a weak hole signal using the anode illumination in the pulsed bias conditions, but its structure was too fuzzy that we could not determine transit time and other transport characteristics. The MC fit plotted by dashed lines in figure 5.1 was obtained assuming the constant electric field across the sample and the defect model with two electron traps [83]. We assume one shallow trap characterized by trapping and detrapping time $\tau_{TS} = 250$ ns and $\tau_{DS} = 40$ ns, respectively, and one deep trap with trapping time $\tau_{TD} = 150$ ns and negligible detrapping.

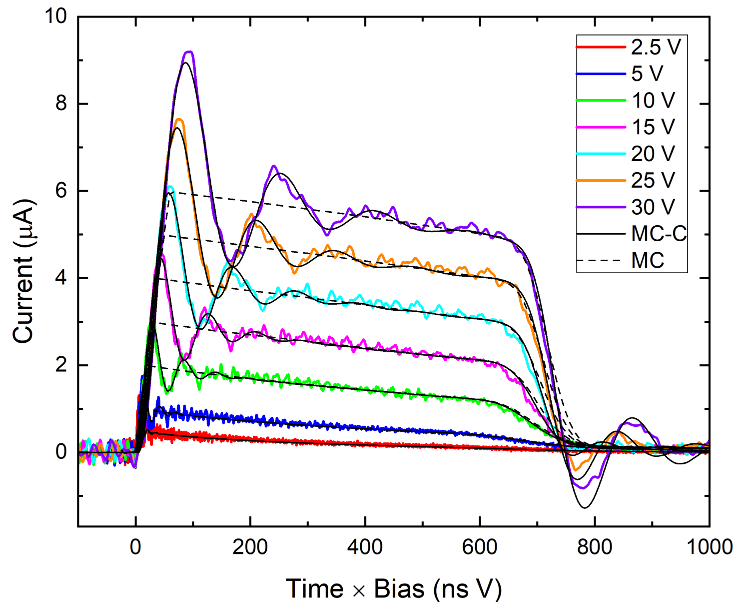

Figure 5.2: Bias dependence of electron current waveforms measured by the L-TCT at pulsed bias and normalized by corresponding bias. Dashed lines represent the MC fit expecting the constant internal electric field. Solid lines plot respective fits after convolution with the function g defined in equation (5.1).

The electron drift mobility evaluated from the MC fit of each CWF at pulse bias conditions resulted $\mu_e = 3650$ cm^2/Vs. Bias dependence of CWF profiles is presented in figure 5.1. Bias dependence of CWFs normalized by corresponding bias is shown in figure 5.2. Such a visualization is particularly useful for the demonstration of linear scaling of the transit time with applied bias and also for an illustrative visualization and comparison of CWFs measured in the wide range of biasing. Dashed lines show the same MC fit as in figure 5.1. Attenuated high-frequency parasitic oscillations apparent at the initial and final stage of CWFs are caused by a response of the electronic circuit to the fast rise and drop of the CWFs [89]. We simulated the respective response function by a substitution RLC circuit inducing underdamped harmonic oscillations defined for the positive time t in the form

$$g(t) = \frac{\omega_0^2 \sin(\omega t)}{\omega} \exp\left(-\frac{t}{\tau_{dm}}\right), \tag{5.1}$$

where $\omega_0 = 1.16 \times 10^9$ s^{-1}, $\tau_{dm} = 4$ ns, and

$$\omega = \sqrt{\omega_0^2 - \frac{1}{\tau_{dm}^2}} = 1.14 \times 10^9 \text{ s}^{-1}. \tag{5.2}$$

The same transfer function (5.1) with given parameters simulating fast oscillations was used at all calculations in this section. The CWFs involving oscillations are then calculated convoluting the MC fit with $g(t)$. The final fits are shown by solid black lines in figure 5.2. We see an excellent agreement of the fit with waveforms at

all biases. The effect of the shallow electron trap level is evident mainly at low bias (2.5–10 V), where it increases and broadens the tail of CWFs around the transit time. Without the shallow trap these waveforms would decrease more rapidly and the fit would worsen. In contrast to CdZnTe [83], where shallow traps with low τ_{TS} and τ_{DS} were reported and carrier drift was delayed by significant trapping, the shallow level defined in this section does not visibly reduce the electron mobility. The trapping time of shallow level is comparable with the transit time even at the lowest biasing and the most of electrons reach the anode without trapping. Although evaluated electron drift mobility is higher than the value presented in [20, 21], it is significantly less than the electron mobility $\mu_{he} = 9400$ cm^2/Vs measured in undoped n-GaAs by the Hall effect measurement [96]. Therefore an existence of the shallow trap with very fast trapping/detrapping on a sub-ns scale can be considered together with an enhanced charged impurity scattering. An important finding is documented in figure 5.3, where identical CWFs presented in figure 5.1 normalized by applied bias are plotted. A nearly equal course of the Current/Bias curves in its transient period proves the linear scaling of the initial current transient with bias in the pulsed bias. This fact testifies to the bias-independent charge drifting through the sample and in consequence to the negligible electron surface recombination at the cathode (see section 2.10). The CWFs measured at the DC bias are presented in figure 5.4 and renormalized to the biased time in figure 5.5. Dashed lines represent the MC fits, solid black lines in figure 5.5 show respective fits after convolution with the function $g(t)$ defined in equation (5.1). We got an unusual shape of CWFs, which we had never observed in other materials or found in literature. We clearly see that regardless of the magnitude of the biasing, CWFs measured at the DC bias increase initially and after reaching the maximum approximately at half of the electron transit time they decrease until the electrons reach the anode. Such observation may be solely interpreted as an electron transport through the sample permeated by an ascending electric field, i.e. formation of the negative space charge region localized in the layer adjacent at the thickness about $L/2$ to the cathode, and by a descending electric field induced by the positive space charge in the part near the anode.

The temporal evolution of CWFs measured at selected biases 10 V and 20 V by L-TCT with different LPD (as defined in figure 4.2) is plotted in figure 5.6. We clearly see that the CWFs evolve continuously in their whole profile, which proves that both positive and negative space charge regions are formed simultaneously. CWF shapes reach the final form at LPD $\approx$ 5 ms.

5.1.2 Model of the space charge formation

The explanation of the parallel formation of both positive and negative space charge regions is a challenging task. Based on our previous investigations of the space charge formation in biased detectors [80] we conclude that obvious models explaining the space charge formation by appropriate contact properties cannot be applied in this material. We need to search for a new model especially to comply with the following results and known properties of SI GaAs:Cr material.

1. We measured significantly lower Hall mobility using Hall effect measurement in contrast to the electron drift mobility evaluated with the L-TCT, which

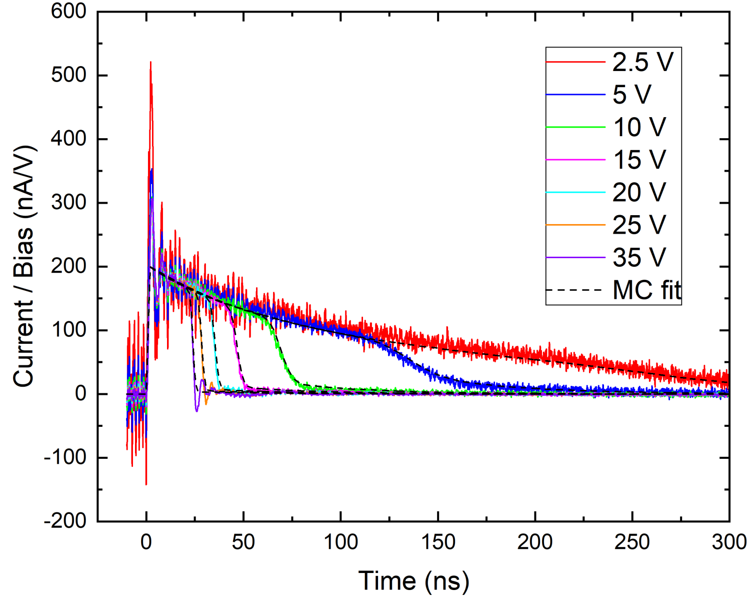

Figure 5.3: Bias dependence of normalized electron current waveforms measured by the L-TCT at pulsed bias. Dashed lines represent the MC fit expecting the constant internal electric field.

testifies on the mixed type of the conductivity of GaAs:Cr and important effect of holes at the transport. Comparable electron and hole conductivity $\sigma_e \approx \sigma_h$ may be assumed.

2. Very weak L-TCT signal of holes was detected reflecting their very short lifetime and a significant hole trapping. Characteristic lifetime of holes $\tau_h < 3$ ns was estimated. Recently, $\tau_h = 1.4$ ns was reported [21] supporting such an expectation.

3. SI GaAs:Cr wafer is prepared by Cr in-diffusion from the Cr layer applied to both surfaces of the wafer. Due to this method, the residual variation of defect structure along the sample thickness can be assumed. Since Cr acts as an acceptor in GaAs:Cr, reduced/enhanced electron/hole density should appear near the surface in contrast to the middle of the detector. In other words, the Fermi energy E_F may be shifted towards the valence band in the subsurface regions relatively to the middle of the detector. Variations at the resistivity similar to those considered here were presented in [17].

At the search for a theory consistently explaining the abovelisted properties we developed a model considering the weak deviation of the hole conductivity along the detector. Since the mechanism of the Cr diffusion and defect compensation is not known in detail in GaAs:Cr yet, we express the course of hole conductivity profiled along the sample thickness by a nearly symmetrical trial function as

follows

$$\sigma(x) = \sigma_0 + \sigma_1 \frac{(x - x_m)^2}{\sqrt{(x - x_m)^2 + \gamma^2}}, \tag{5.3}$$

where σ_0, σ_1, γ, and x_m are model parameters. Anticipating diffusion of Cr occurring from both sides of the wafer, $x_m \approx L/2$ is foreseen. A similar course may be deduced from the profile of resistivity [17]. The cathode is set to $x = 0$ and sample thickness $x = L = 0.5$ mm. Let us note that involving holes in the concept is important due to their short lifetime and consequently a fast interaction with principal trap levels by the trapping and detrapping. The fast exchange of holes between the valence band and hole trap assures the local equilibrium between the band and trap, which is critical for the validity of the concept of variable conductivity in this model. Considering the mean free path of holes < 7 μm, which appears sufficiently short in the 500 μm thick sample. Estimating the hole mobility ≈ 200 cm^2/Vs and maximum electric field ≈ 1 kV/cm, we obtain the lifetime of holes < 3 ns. Evidently, shorter hole lifetime is better for the validity of the approach. Fast electrons with the extended lifetime could not cause observed formation of abruptly changing positive and negative space charge.

Equation (5.3) is combined with Ohm's law

$$j = \sigma \mathcal{E} \tag{5.4}$$

Gauss's law

$$\frac{\partial \mathcal{E}}{\partial x} = \frac{e\rho}{\varepsilon} \tag{5.5}$$

and continuity equation

$$\frac{\partial \rho}{\partial t} = -\frac{1}{e}\frac{\partial j}{\partial x}. \tag{5.6}$$

The principle of the model consists in the charging of the hole trap induced by the variable conductivity and nonequilibrium hole distribution in biased sample.

Equation (5.3) represents only the hole conductivity, which is thus lower than the total conductivity involving also electrons. Equations (5.3)–(5.5) were substituted into equation (5.6), which was numerically time-integrated for given $\sigma(x)$. $\mathcal{E}(x)$ was calculated by the integration of equation (5.5) after each integration step with the boundary condition preserving the bias

$$U = -\int_0^L \mathcal{E}(x)\mathrm{d}x. \tag{5.7}$$

Basic properties of GaAs used at the calculations were taken from [96] and we used the hole mobility $\mu_h = 171$ cm^2/Vs [19]. Acquired time-dependent $\mathcal{E}(x)$ has entered in the MC simulation of experimental CWFs presented in figure 5.4 whilst the trapping/detrapping time of electron traps remained the same as obtained from the fit at pulsed bias shown in figure 5.1. The self-consistent loop of the electric field calculations and MC simulations was repeated until the optimum fit was obtained. All CWFs measured at applied bias ranging in the interval 2.5-30 V, LPD in the interval 80 μs $-$ 5 ms and illuminating alternatively both sides of the sample were fitted. The unique set of parameters was retrieved from the fitting of electron CWFs as follows: $\sigma_0 = 2.2 \times 10^{-10}$ Ω^{-1}cm^{-1}, $\sigma_1 = 1.3 \times 10^{-8}$ Ω^{-1}cm^{-2}, $\gamma = 0.1$ mm and $x_m = 0.225$ mm. The example

of the CWF time-evolution in sample biased at 20 V is plotted in figure 5.7. Dashed lines represent the MC fits using the electric field profile calculated by the above given model and solid black lines show respective fits after convolution with the function $g(t)$ defined in equation (5.1). It is seen that the linearly shaped CWF measured after biasing, identical to those plotted in figure 5.1, gradually evolves to the DC shaped CWF with the distinct maximum in the center. Internal electric field profile in the detector is presented in the inset, where arrows show the direction of the electric field evolution. Let us note that all numerical calculations and fits were performed with rather low number of optimized parameters characterizing the electron (de)trapping τ_{TS}, τ_{DS}, and τ_{TD} and the conductivity profile defined in equation (5.3). The bias dependence of the internal electric field profile representing the theoretical fit of DC CWFs is shown in figure 5.8. We may see an enhanced profiling of the field at increased bias symmetrically modulated by the variable conductivity $\sigma(x)$ shown in figure 5.8 as well. Except the sign, the modulation is independent of the polarity of bias, which entails the same character of CWFs measured from both side of the sample. Considering obtained results, the conductivity profile reaches its minimum at $x_m = 0.225$ mm, where $\sigma(x_m) = \sigma_0 = 2.2 \times 10^{-10}$ Ω^{-1}cm^{-1} and maximum at the surface $\sigma(0) = 4.4 \times 10^{-10}$ Ω^{-1}cm^{-1}; $\sigma(L) = 5.2 \times 10^{-10}$ Ω^{-1}cm^{-1}. Respective position of Fermi energy $E_F(x_m) = E_V + 0.689$ eV, $E_F(0) = E_V + 0.672$ eV, and $E_F(L) = E_V + 0.668$ eV. The hole and electron densities range from 8×10^6 cm^{-3} to 1.8×10^7 cm^{-3} and from 6×10^4 cm^{-3} to 1.4×10^5 cm^{-3}, respectively, which is consistent with negative sign of the Hall coefficient with reduced measured Hall mobility effected by mixed transport. Estimating the hole mobility ≈ 200 cm^2/Vs and maximum electric field ≈ 1 kV/cm, we deduce the lifetime of holes < 3 ns corresponding to the mean free path of holes < 7 μm, which appears sufficiently short in the 500 μm thick sample. Evidently, the shorter hole lifetime is better for the validity of the approach. The steady state space charge density distribution deduced through equation (5.5) from the electric field profile presented in figure 5.8 is shown in figure 5.9. The principle of the positive charging stems from the weak injection of holes from the anode related with the larger hole conductivity and density in that region. Oppositely, the negative charge appears in the region adjacent to the cathode where the holes are depleted due to relatively lower conductivity in the middle of the sample, which inhibits the hole current. It is worth pointing out to the fact that only two parameters σ_0 and σ_1 allowed us to describe both the velocity of the space charge formation and the final magnitude of the space charge. Simultaneously, the fitted average hole conductivity of the sample $< \sigma \geq 3.2 \times 10^{-10}$ Ω^{-1}cm^{-1} is slightly lower than the experimentally determined conductivity 5×10^{-10} Ω^{-1}cm^{-1}, which is in agreement with the model prediction above.

5.1.3 Charge collection efficiency

The bias dependence of the collected charge evaluated by the time-integration of CWFs in both bias conditions presented in figures 5.1 and 5.5, is shown together with the single carrier Hecht equation fits (see section 2.11) in figure 5.10. We evaluated the electron mobility-lifetime products $(\mu_e\tau_e)_{Pulse} = 5.5 \times 10^{-4}$ cm^2/V and $(\mu_e\tau_e)_{DC} = 5.2 \times 10^{-4}$ cm^2/V from the pulse and DC biased CWFs, respec-

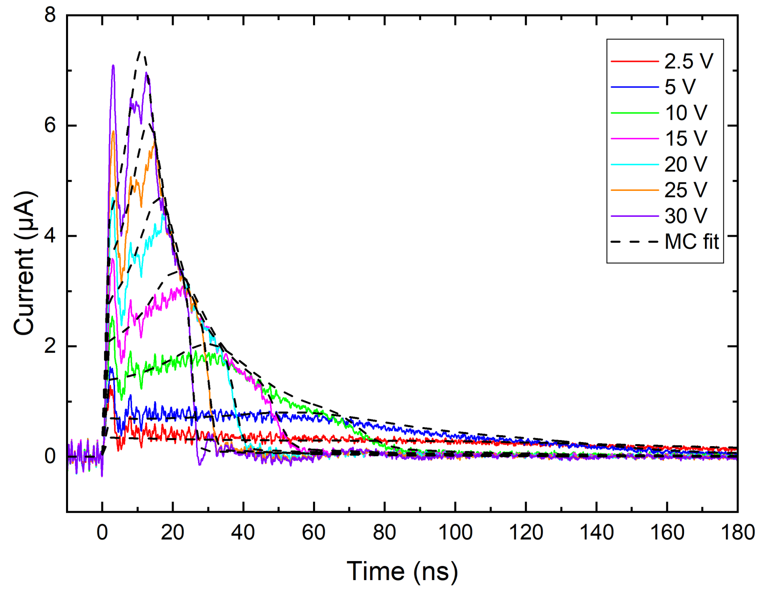

Figure 5.4: Electron current waveforms measured by the L-TCT at DC bias. Dashed lines represent the MC fit calculated according the model defined in subsection 5.1.2

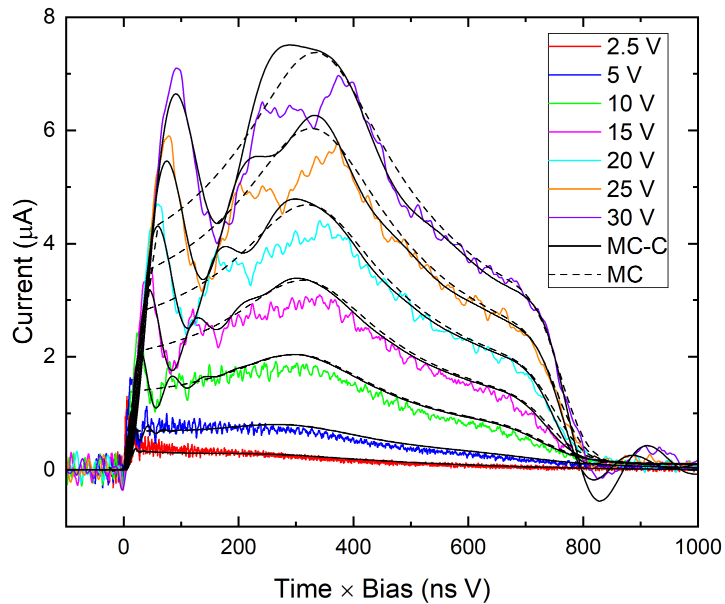

Figure 5.5: Pulsed bias dependence of the electron CWFs. The dashed lines represent the MC fit.

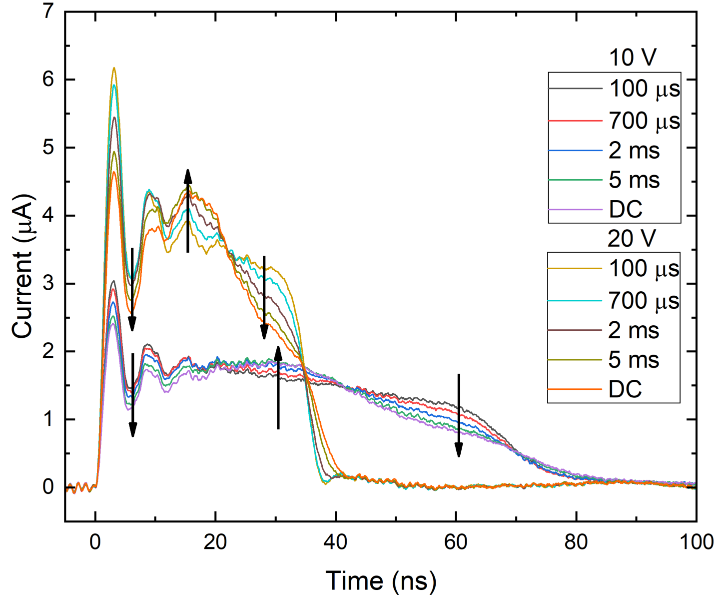

Figure 5.6: Electron CWF dependence on the laser pulse delay for 10 V and 20 V measured by the L-TCT at pulsed and DC bias. Arrows show the direction of the waveform evolution.

tively. The mobility-lifetime product in pulsed regime $(\mu_e\tau_e)_{Pulse}$ is equal to the product of μ_e = 3650 cm^2/Vs and τ_{TD} = 150 ns obtained by the MC simulation. Let us note that the shallow electron trap does not induce real losses to the drifting charge and it does not affect the charge collection. Consequently, the electron lifetime is equal to τ_{TD}. With respect to the very low surface recombination, $(\mu_e\tau_e)_{Pulse}$ represents the right value of $\mu_e\tau_e$ unaffected by the space charge formation. Slightly lower value of $(\mu_e\tau_e)_{DC}$ is caused by the electric field warping in DC conditions due to the space charge formation in the detector and subsequently by extended transit time. For a comparison, applying the pulse height spectrum analysis using alpha particles we obtained $(\mu_e\tau_e)_\alpha = 1.4\ \times 10^{-5}$ cm^2/V. The large difference between $(\mu_e\tau_e)_{Pulse}$ and $(\mu_e\tau_e)_\alpha$ is caused by a strong plasma effect inducing strong loss of photogenerated electrons and the charge collection depression especially at low biases. Similar lower $(\mu_e\tau_e)_\alpha$ value was also measured in [28] with the same interpretation.

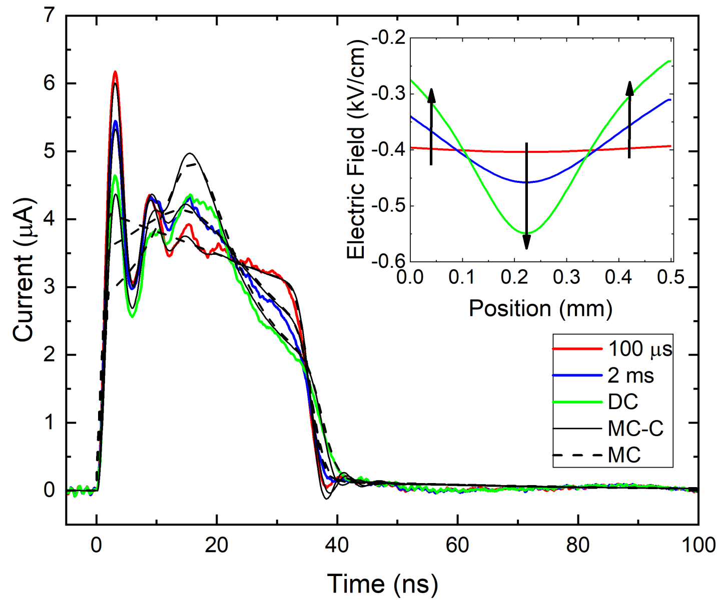

Figure 5.7: Electron CWF dependence on the laser pulse delay for 20 V measured by the L-TCT at pulsed and DC bias. Dashed lines represent the MC fit calculated according the model defined in the subsection 5.1.2. Solid lines plot respective fits after convolution with the function g defined in equation (5.1). The internal electric field profile in the detector is presented in the inset, where arrows show the direction of the electric field evolution.

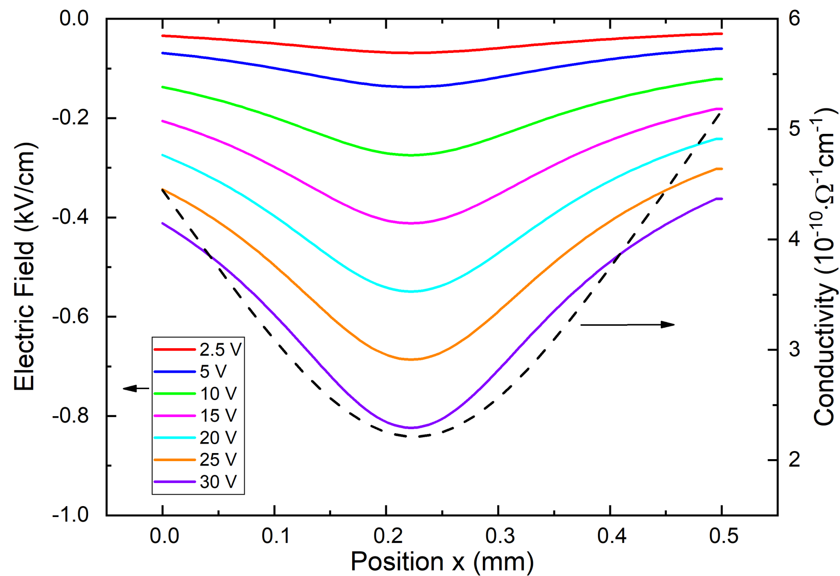

Figure 5.8: Bias dependence of the internal electric field profile at the DC bias. Dashed line shows the profile of fitted conductivity.

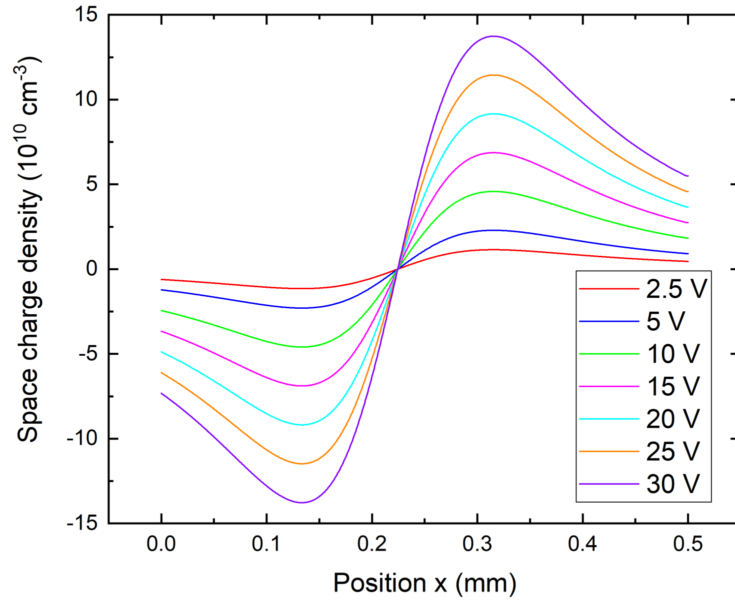

Figure 5.9: Bias dependence of the space charge density profile at the DC bias.

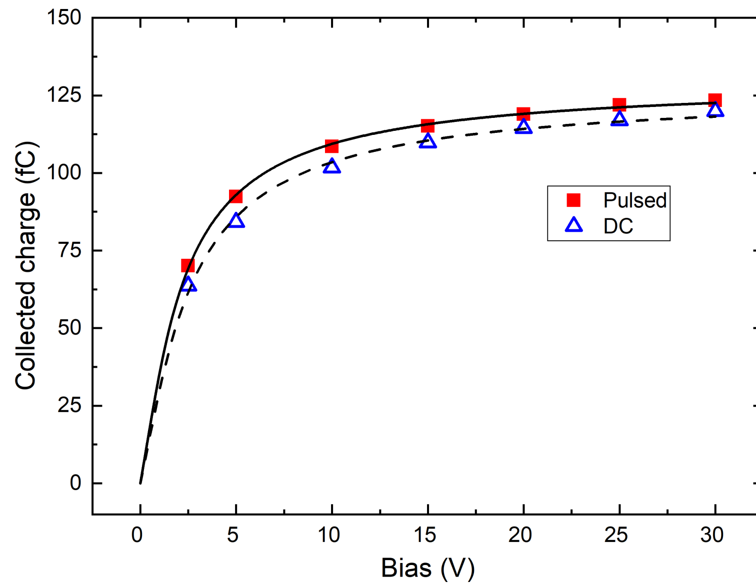

Figure 5.10: Bias dependence of collected charge evaluated by the time-integration of CWFs at the pulse and DC bias conditions. Solid and dashed lines represent the single carrier Hecht equation fits.

5.1.4 Section conclusion

In this section, we measured electron current transients in GaAs:Cr sensor using L-TCT in pulsed and DC bias. We observed the gradual formation of negative and positive space charge within 5 ms. Electron lifetime $\tau_e = 150$ ns and electron drift mobility $\mu_d = 3650$ cm^2/Vs were evaluated from the MC simulations. Pulsed bias application eliminated internal electric field distortion. L-TCT allowed the determination of the internal electric field profile, aiding growth technology optimization. It provides a non-destructive method with better precision than commonly used techniques for studying charge transport and internal electric properties in GaAs:Cr. We showed that GaAs:Cr is a suitable material for radiation detection. Results of this section were published in [16].

5.2 CdZnTe

In this section, the charge transport in CZT detector under X-ray high flux is studied. One of the most important requirements for radiation sensors used in high-flux photon counting applications is their ability to operate in an intense and rapidly changing X-ray environment. These sensors need to sufficiently sustain high fluxes of incoming X-rays of the order of 600 Mcps/mm^2 while maintaining a short enough charge collection time and high temporal stability [97]. Due to the low mobility of holes compared to that of electrons and substantial hole trapping, traditionally, the use of CdTe and CdZnTe materials under these intense irradiation environments has been limited [98, 99]. Suffering from severe X-ray dynamic polarization because of electric field distortion and collapse, historical high-Z sensors were unable to operate under relatively low X-ray flux levels. In recent years, however, these issues have been studied extensively, and significant gains in sensor performance have been achieved [37, 100]. These advancements were mainly due to improvements in crystal growth (by suppressing the density of the deep hole traps) and fabrication quality (by minimizing the fabrication-induced surface states). In particular, important progress in the charge transport properties and uniformity has been made. High electron mobility–lifetime products of electrons $\mu_e\tau_e$ greater than 10^{-2} cm^2/V were achieved [101]. Simulations of semiconductor radiation detectors were studied in [71, 85, 86, 102, 103] to obtain charge transport properties. Charge transport in pixelated detectors was studied in [104, 105, 106], where the effects of charge sharing and material quality on detector performance were investigated.

High-flux sensors typically require an operating bias U of the order of 1000 V. Assuming that the typical value for the electron mobility is $\mu_e = 1000$ cm^2/Vs, then for a high voltage bias of $U = 1000$ V, the electric field for a $L = 2$ mm thick detector is $\mathcal{E} = 5$ kV/cm, which corresponds to the electron transit time through the whole detector thickness of 40 ns. This high electric field might cause some long-term reliability concerns; therefore, it would be desirable to reduce its value. In addition, the requirement of generating high-voltage U causes limitations for portable scanning equipment. It is, therefore, important to study the minimum electric field required for proper sensor operation. The main problems arising due to a reduced electric field are the slowing down of the drift velocity and the extension of the transit time. Reducing the electric field leads to a decrease in the amount of collected charge and the count numbers obtained.

In this section, we simulate the charge transport inside the sensor, evaluate the properties of carrier traps and demonstrate the effects caused by a reduced electric field. We define the critical bias U_c as producing sufficient collection efficiency to operate under high X-ray flux and characterize the sensing quality of the sensor operating under such conditions. The simulations fit the experimental data measured on commercial detector at Redlen Technologies, Inc. The simulations allowed us to obtain additional insights into the physical effects on the detector under low electric field. The existing literature does not cover this topic.

5.2.1 Experiment

At Redlen Technologies, Inc. several high-flux sensors with various pixel pitches and 2 mm thickness were fabricated and experimentally analyzed using a variety of characterization techniques using PICTS (Photo-Induced Current Transient Spectroscopy), Corema resistivity measurements, DLTS (Deep Level Transient Spectroscopy), and the Pockels technique. It was found that the Pockels effect, which builds on the linear electro-optic effect where the refractive index of a medium is modified in proportion to the applied electric field strength, was particularly useful in measuring the electric field under various high-voltage conditions. In this section a semi-insulating commercial-grade CdZnTe detector with the dimensions of $10 \times 10 \times 2$ mm^3 with 330 μm pitch used in spectral Computed Tomography high-flux applications is studied. The CdZnTe sensor used in this study reaches the highest count rate performance known in the X-ray detection of High-Z materials, achieving rates over 1000 Mcps/mm^2 [107]. The detector has two opposite electrodes: the cathode is planar, and the anode is pixelated [108]. The detector is characterized using the Pockels technique [109, 110, 111], from which the electric field profile is obtained for several applied biases in the dark and under different X-ray fluxes. A standard X-ray tube set-up with a kVp of 120 kVp is used [112]. The respective X-ray spectrum and attenuation coefficient of CdZnTe are shown in Figure 5.11 [113, 29]. The scheme of the detector with incoming X-rays from the cathode side is shown in Figure 5.12, where the typical electric field profile of a polarized detector is outlined.

The attenuation coefficient of X-ray $\alpha(E)$ is fitted in the interval 10 keV – 120 keV by a fitting function, as follows:

$$\alpha(E) = \Big[808 \times 10^{2.65} + 114.6(E48K)^{2.65}\,\Theta(E - E48K) + \\ +94.7(E52K)^{2.65}\,\Theta(E - E52K)\Big]/E^{2.65}, \tag{5.8}$$

where $\Theta(E)$ is Heaviside step function (see section 2.4). $E48K = 26.7112$ keV and $E52K = 31.8138$ keV are taken from [113].

Detector performance was evaluated using a photon-counting Application Specific Integrated Circuit (ASIC) that is used in the detector module for Spectral Computed Tomography. The ASIC has 864 (24×36) identical channels. Each channel has a typical charge sensitive amplifier (CSA) with a feedback capacitor. The output of the CSA is amplified by the shape amplifier and compared in the comparator to the set threshold(s). When the signal crosses pre-defined threshold levels (for example, 16 keV), the clock starts, and the circuits samples for the sampling time $t_s = 16$ ns of the collected charge. If the charge is saturated in this period, the correct value is obtained. If saturation is not reached, the circuit reads a lower value, creating an energy error. This feature is called a ballistic deficit.

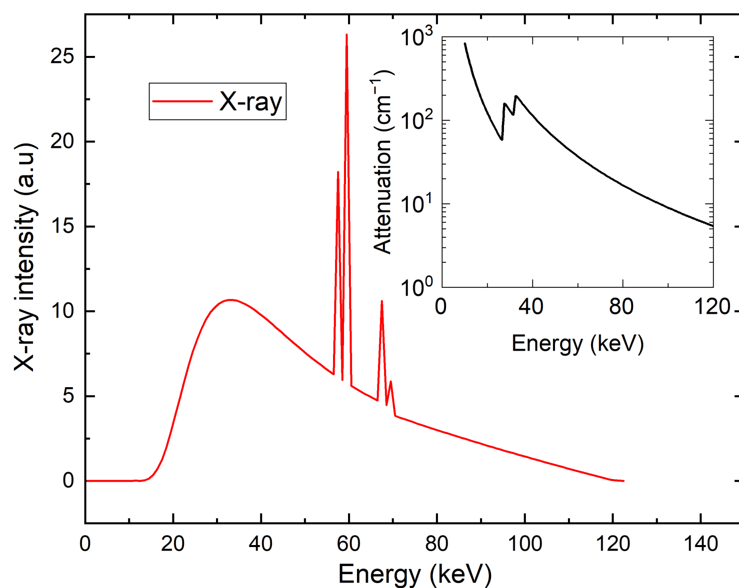

Figure 5.11: X-ray spectrum (red) with attenuation coefficient in CdZnTe (inset).

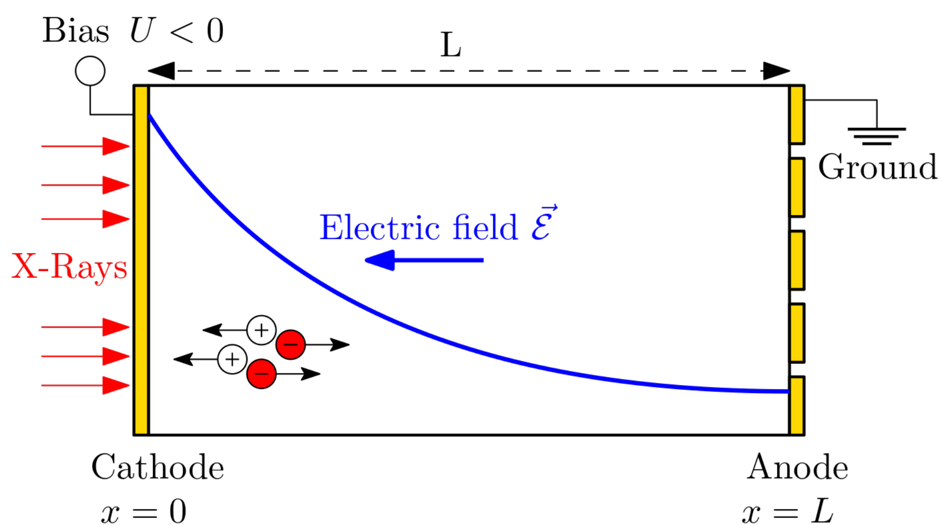

Figure 5.12: Schematic view of the electric field distribution in a detector with a positive space charge.

5.2.2 Simulation of the detector performance at low bias

Detector polarization induced by hole trapping under high-flux X-ray excitation leads to a significant reduction in the electric field near the pixelated anode. An extended charge collection time amplifies the ballistic deficit and limits the maximum accessible X-ray flux that can be distinguished in spectrally sensitive electronics. An extended transit time also constrains high-flux applications, leading to pileups and the loss of energy resolution. In our case, the transit time is still short enough to minimize the charge sharing between the pixels due to diffusion broadening. Considering that the transit time t_r is shorter than 200 ns for a bias of > 200 V, we estimate the diffusion broadening $\Delta x \approx \sqrt{D_e \tau_e} < 20$ μm, which is much less than the pixel pitch of 330 μm. Thus, we do not add the correction to the charge sharing here, i.e., the signal of only one pixel is considered. In this section, we model space charge effects due to high-flux X-ray irradiation with the spectrum plotted in figure 5.11. In the charge transport model used for the charge collection calculation, we only consider the drift current of electrons and describe the current waveform $I(t)$ in one pixel in a pixelated detector with the electric field profile using Shockley-Ramo theorem (see section 2.8) with the following formula:

$$I(t) = Q(t)\mu_e \mathcal{E}(x(t)) E_W(x(t)) \tag{5.9}$$

where μ_e is electron drift mobility, $\mathcal{E}(x)$ is the electric field at the depth x, and $E_W(x)$ is the weighting field calculated for the pixelated detector according to [67]. Drifting photogenerated charge $Q(t) = Q_0 \exp(-t/\tau_e)$ is attenuated with the electron lifetime te that is taken to be constant, i.e., the space charge is considered to be independent, for simplicity. The weighting field against the middle of the pixel is considered. The electric field is obtained through the fitting of the Pockels effect data.

Starting with equation (5.9), the numerical treatment is performed according to the following steps.

1. The position of the drifting charge excited at the cathode $x(t)$ is calculated by integrating the following kinetic equation:

$$\int_0^{x(t)} \frac{\mathrm{d}x'}{\mathcal{E}(x')} = \mu_e t. \tag{5.10}$$

2. Normalized charge $\tilde{q}_0(t)$ excited at the cathode and collected in time t, considering the attenuation of the collected charge due to the RC time τ_{RC} is calculated by integrating the following equation:

$$\frac{\mathrm{d}\tilde{q}_0(t)}{\mathrm{d}t} = -\frac{\tilde{q}_0(t)}{\tau_{RC}} + \frac{I(t)}{Q_0}. \tag{5.11}$$

The RC time is usually much longer than the transit time, and the first term on the right-hand side of equation (5.11) may be neglected.

3. Utilizing the linearity of equation (5.11), we may conveniently generalize $\tilde{q_0}(t)$ to the case of the charge collection of the normalized charge excited in the detector's interior that may be expressed as follows:

$$\tilde{q}(t, t_d) = \left[\tilde{q}_0(t) - \tilde{q}_0(t_d) \exp\left(-\frac{t - t_d}{\tau_{RC}}\right)\right] \exp\left(\frac{t_d}{\tau_e}\right) \Theta(t - t_d). \tag{5.12}$$

t_d is the drift time representing the drift delay of the charge excited at the cathode to the depth d in the detector where X-ray photon absorption has occurred. t_d is linked to d by equation (5.10). The scaling of the drift of the charge through the detector by the drift time appeared to be useful in the calculations. This achievement enables us to significantly simplify the enumeration when the calculation of the collected charge following the excitation wherever in the bulk may be derived from the collected charge excited near the cathode without the additional solution of differential equation (5.11).

4. We simulate the processing of the collected charge by the electronic circuit. This circuit is characterized by the threshold energy $E_t = 16$ keV at which the charge sampling starts, and the sampling time t_s, defining the time window of the charge collection. The process is simulated in two steps. At first, the collected charge expressed as $Q_0\tilde{q}(t, t_d)$ is monitored, waiting for the time at which it exceeds the energy threshold. Subsequently, the collected charge $q_c(t_d) = Q_0\tilde{q}(t + t_s, t_d)$ is evaluated.

5. Having $q_c(t_d)$, we may start with the construction of the spectra. The normalized spectrum $S_m(ch, E_X)$, indexed by a channel number ch and excited with a monochromatic X-ray photon with energy E_X, is obtained by the sum of the contributions to the spectrum excited by the photon absorbed in a specific depth of the detector. We proceed with the following loop in i

$$S_m^{(i)}(ch_i, E_X) = S_m^{(i-1)}(ch_i, E_X) + \alpha(E_X)\exp\left(-\alpha(E_X)x(t_{di})\right)\frac{\Delta x_i}{\Delta t}, \quad (5.13)$$

where the channel number ch_i is defined by the collected charge

$$ch_i = \lfloor \frac{q_c(t_{di})}{\Delta Q} + \frac{1}{2} \rfloor, \quad (5.14)$$

where lower brackets represent the floor function that returns the integer part to yield ch_i. The index i scales the drift time t_{di} through the detector thickness, and ΔQ defines the width of one channel and $\Delta x_i = x(t_{di}) - x(t_{d(i-1)})$. In real calculations, to obtain smooth curves, we divide the energy axis into many more channels than used in the experiments, i.e., ΔQ is sufficiently small. The channel is assigned to the apparent photon energy

$$E = \frac{ch\Delta Q E_X}{Q_0} = ch\Delta E_X, \quad (5.15)$$

which can be simplified by defining the channel energy width $\Delta E_X = \Delta Q E_X / Q_0$. This option is further used in calculations, allowing us to join photoexcited charge with energy units.

6. The last step of the treatment is the construction of the full X-ray spectrum $S(E)$. It is calculated by integrating the contributions of photons at a specific energy weighted with the corresponding radiation intensity. The final formula reads as follows:

$$S(E) = \int S_m(ch, E_X) I_0(E_X) \mathrm{d}E_X, \quad (5.16)$$

where E and ch are interconnected by equation (5.15).

5.2.3 Discussion

To simulate the charge transport and the space charge formation inside the detector, we numerically solved the drift–diffusion equation coupled with Poisson's equation [80]. This allowed us to obtain the profiles of space charge, electric field, and energy level occupancies. Since the polarization phenomena are caused, in our case, by high flux irradiation, we disregarded electric-contacts-induced polarization [80, 100, 110]. We used Ohmic contacts that cause zero band bending under contacts in simulation to prevent detector charging in the dark. Possible deviation of the contacts from an Ohmic character does not affect the model unless the injection current approaches the value of the photocurrent. Obviously, the use of a strongly injecting contact would be improper because an enhanced injected current would induce an enormous noise, making the detector useless. The simulations were performed on a sensor with a thickness of $L = 2$ mm. Electron mobility $\mu_e = 1000$ cm^2/Vs and hole mobility $\mu_h = 80$ cm^2/Vs are consistent with common values measured in CdZnTe [114].

To simulate charge transport inside detector, we numerically solved the DDE coupled with Poisson's equation [100, 101]. This allowed us to obtain profiles of space charge, electric field, and energy level occupancies. Since the polarization phenomena are caused by the high flux irradiation, we used ohmic contacts that cause no band bending under contacts in simulation to prevent detector charging without X-ray flux. Simulations are done on sensor with thickness $L = 2$ mm. Electron mobility $\mu_e = 1000$ cm^2/Vs and hole mobility $\mu_h = 80$ cm^2/Vs are consistent with common values measured in CdZnTe [71].

Typical electric field profiles measured using Pockels effect in the dark (no X-ray) and 16 Mcps/mm^2 and 80 Mcps/mm^2 high-flux X-ray irradiation are shown in figure 5.13; the simulated electric field profiles are shown in figure 5.14. As expected, the electric field is uniform under dark conditions, but it degrades near the anode under high-flux excitation. The simulated electric field profiles show good agreement with the experiment, validating the used defect model (figure 5.13).

X-ray excitation intensity representing the rate of (e-h) pairs generation inside the sample is calculated according to the following formula:

$$I_{ext}(x) = \frac{1}{E_b} \int I_{xray}(E)\alpha(E)E \exp\left(-\alpha(E)x\right) \mathrm{d}E, \tag{5.17}$$

where I_{xray} is X-ray photon flux density, E is the energy of the X-ray photon, and $E_b = 4.5$ eV is the average energy of the formation of (e-h) pairs. The respective excitation intensity I_{exc} plotted in figure 5.15 shows dominant excitation under the cathode and a fast decrease toward the anode.

The defect model fitting the electric field profile consists of one electron and one hole deep trap whose parameters are defined in the defect scheme in figure 5.16. The Fermi level was fixed in midgap $E_F = E_C - 0.775$ eV. Since we performed only steady-state experiments at a constant temperature, capture cross-cannot be determined. As discussed in [87] steady-state experiments do not offer a way to determine the capture cross-section of the traps.

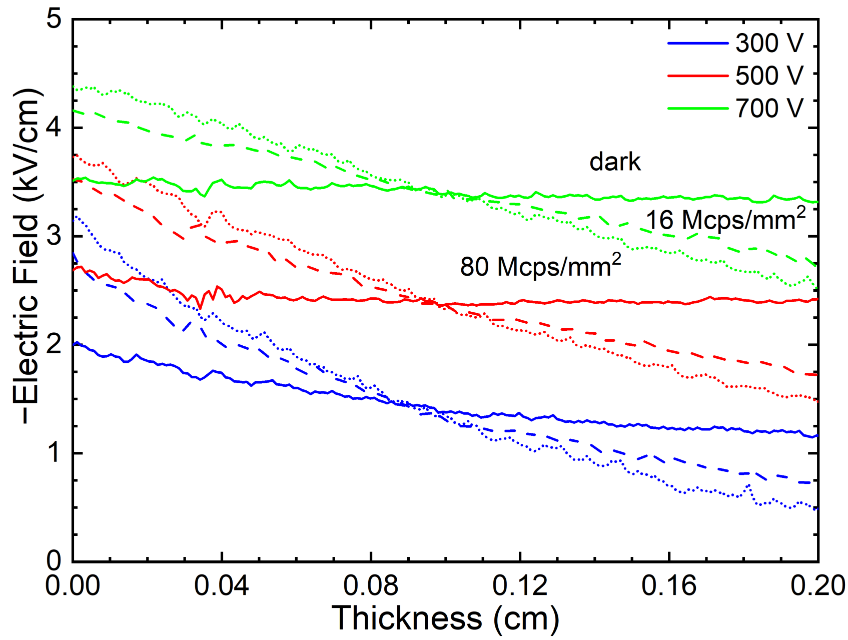

Figure 5.13: Measured electric field profiles in a 2-mm-thick CZT sensor; solid lines represent electric field with no incoming X-ray (dark mode), dashed lines are for X-ray 16 Mcps/mm^2, dotted lines are for X-ray 80 Mcps/mm^2, blue, red, and green color mark 300 V, 500 V, and 700 V bias, respectively.

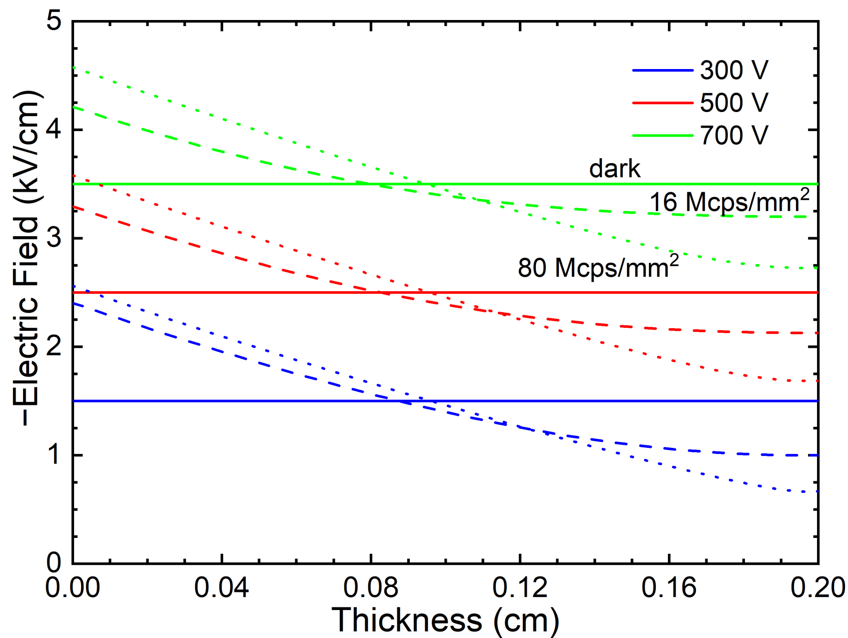

Figure 5.14: Numerical simulation of field profiles in a 2-mm-thick CZT sensor; solid lines represent electric field with no incoming X-ray (dark mode), dashed lines are for X-ray 16 Mcps/mm^2, dotted lines are for X-ray 80 Mcps/mm^2, blue, red, and green color mark 300 V, 500 V, and 700 V bias, respectively.

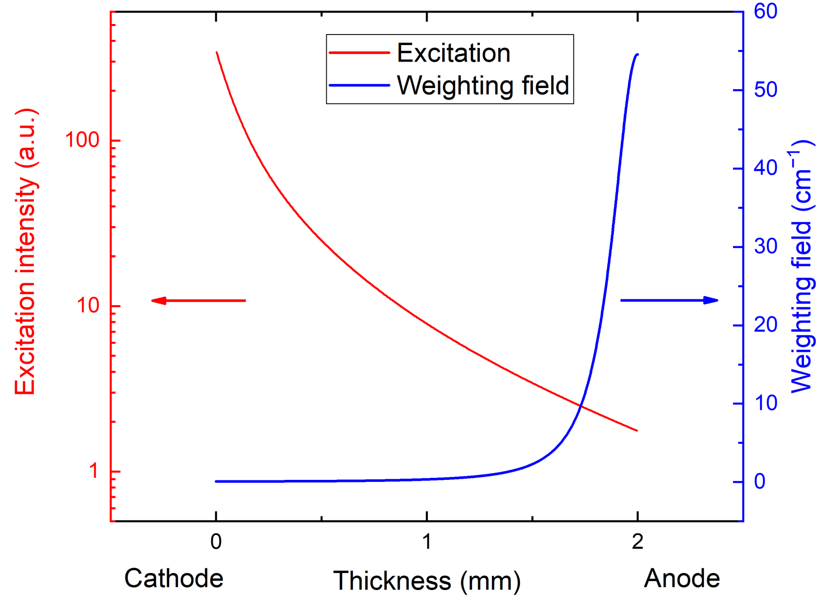

Figure 5.15: Profile of X-ray excitation, which shows dominant excitation under cathode with fast decrease toward anode. Weighting field was calculated according [67] in the middle of the pixel with 330 μm pitch.

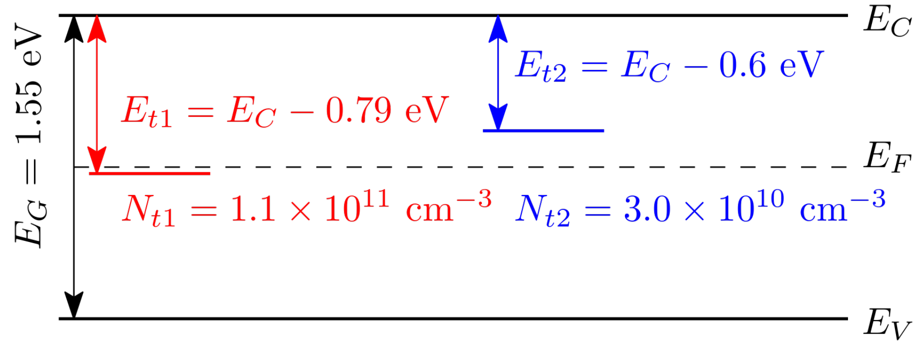

Figure 5.16: Scheme of energy levels with parameters determined by the fit of electric field. Hole trap is red; electron trap is blue.

The corresponding space charge density is shown in figure 5.17. While the hole trapping in the hole trap causes the positive space charge and the tilt of the electric field throughout the sample, the presence of the electron trap causes a gradual decrease in the positive space charge along the sample thickness and even negative space charge formation near the anode.

Subsequent measurements were performed using a standard X-ray tube with a 120 kVp setup at a photon flux of 20 Mcps/mm^2. The counts vs. bias were measured at a count rate of 20 Mcps/mm^2, as shown for one representative pixel in figure 5.18. The counts for $U < U_c$ are approximated using a straight line, and the point at which maximum counts were achieved is considered to be $U_c \approx 265$ V.

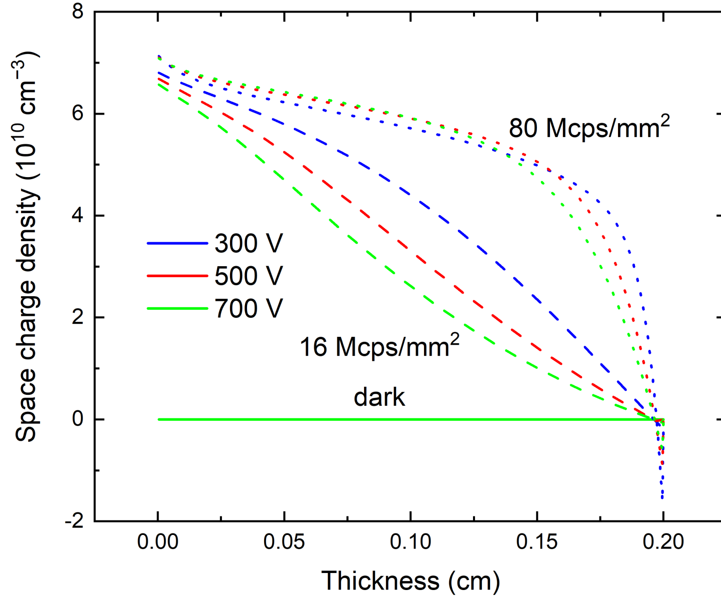

Figure 5.17: Calculated space charge density from the numerical simulation. In the dark regime, there is no space charge in the sample.

This procedure was repeated for each pixel, and the distribution of U_c is shown in figure 5.19. The decrease in measured counts at low bias is not mainly caused by carrier trapping but by the ballistic deficit of low energy X-ray photons, which do not cross the threshold level, frequent pileups, and charge sharing between pixels [104], which is accentuated at the low electric field near the pixelated anode.

In figure 5.20, we show the current waveforms calculated using equation (5.9) with the electric field obtained from the numerical simulation with the X-ray photon absorbed close to the cathode, and the use of the weighting field is plotted in figure 5.15. As is common in pixelated detectors, the weighting field is low near the cathode and rapidly increases near the anode due to specific pixel sensitivity. This feature allows us to eliminate holes from the calculations since only a small number of holes is generated near the anode in the area with the large value of the weighing field. Simultaneously, the low mobility of holes yields a low contribution to the charge collection at the chosen short sampling time.

The current waveforms in figure 5.20 were simulated with near-cathode absorption, this does not affect the result since the weighting field is small there, and only electrons that drift near the anode contribute to the signal. This is demonstrated in figure 5.21, where the collected charges for photons absorbed near the cathode (red) and deep inside the detector 1.44 mm (blue) are shown. These curves are synchronized in time so that the arrival of charge to the anode occurs at the same time, 146 ns, regardless of the depth of the charge creation. The lower detected counts in figure 5.18 at low bias are due to the long transit time compared to the sampling time. Carrier losses due to the limited lifetime have a minor effect in this case since the drift time remains much shorter than the lifetime, even at the considered low bias. In the case of zero space charge, the

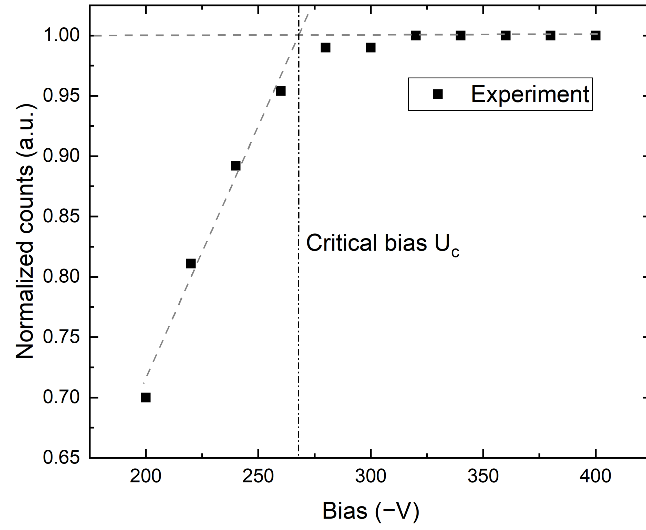

Figure 5.18: Measured counts in 2-mm-thick CZT sensor under X-ray conditions with a count rate of 20 Mcps/mm^2 for a typical pixel. Procedure to extract critical bias U_c is shown at the intersection of linear fit for bias $U < U_c$ with the horizontal line at maximum CCE.

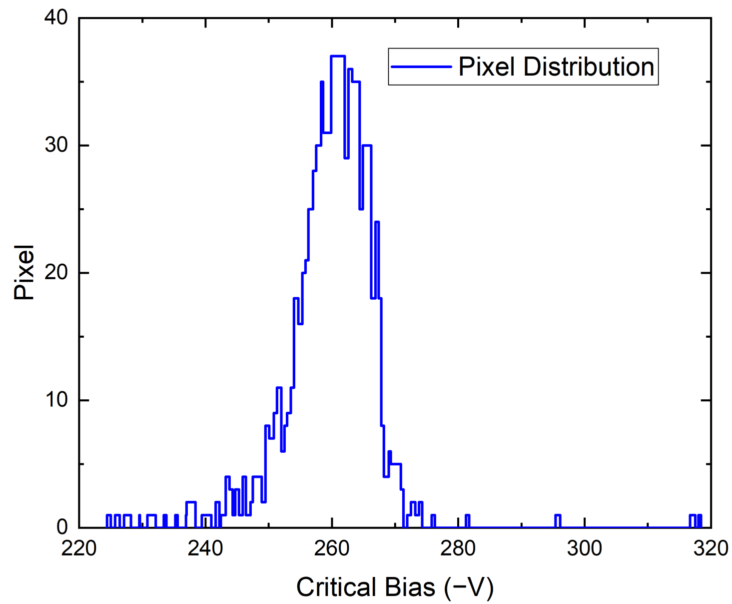

Figure 5.19: Distribution of U_c values for all pixels.

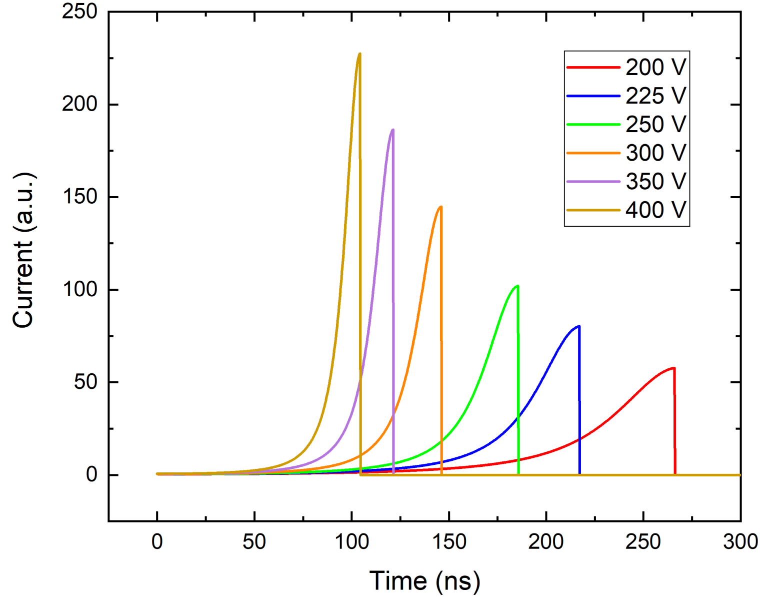

Figure 5.20: Simulated current waveforms for different biases and 20 Mcps/mm^2 X-ray.

shoulder at the count number in figure 5.18 would be shifted significantly to the lower bias, and the segment of the respective curve would be flat in the plotted region.

Based on the critical bias shown in figure 5.18, we have chosen a bias of 300 V as the characteristic value of low bias considered for the utilization of the detector for X-ray spectroscopy. We calculated the X-ray spectrum detected by the detector simulated by the theory presented in items 1–6 in subsection 5.2.2, assuming that the detector polarization is due to the high-flux X-rays at 20 Mcps/mm^2 and common parameters characterizing the circuit $\tau_{RC} = 1$ μs, which, in our case, is much longer than the sampling time of $t_s = 16$ ns, and its effect is negligible. The corresponding spectrum, together with the original spectrum, is plotted in figure 5.22. We may identify two distinct regions in the spectrum. While the low-energy part fits the original spectrum very well, the high-energy counts are collected at nearly the same energy of about 45 keV, which manifests as the large peak in that region. The effect is induced by the ballistic deficit, which is caused by the slow charge collection, which is not completed during the 16-ns sampling time.

The details of the charge collection are demonstrated in figure 5.23, where the collections of the charge induced by the photons with three different energies are depicted. The red curve represents the relative collected charge whose shape remains the same at all photon energies. The charge collection by the electronics is critically affected by the relative position of the threshold marked with horizontal lines representing a threshold of 16 keV. The first case (A) represents the photon with an energy smaller than the threshold of 16 keV. Since the collected charge curve is lower than the threshold, no sampling event occurs, and the charge is

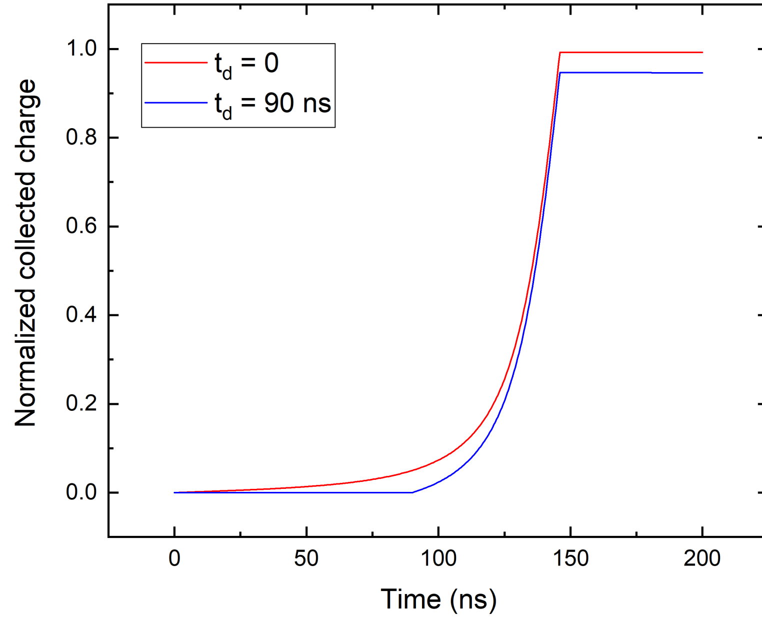

Figure 5.21: Comparison of the collected charge of X-ray photon absorbed near the cathode (red), and deep inside the detector, 1.44 mm (blue). $U = 300$ V.

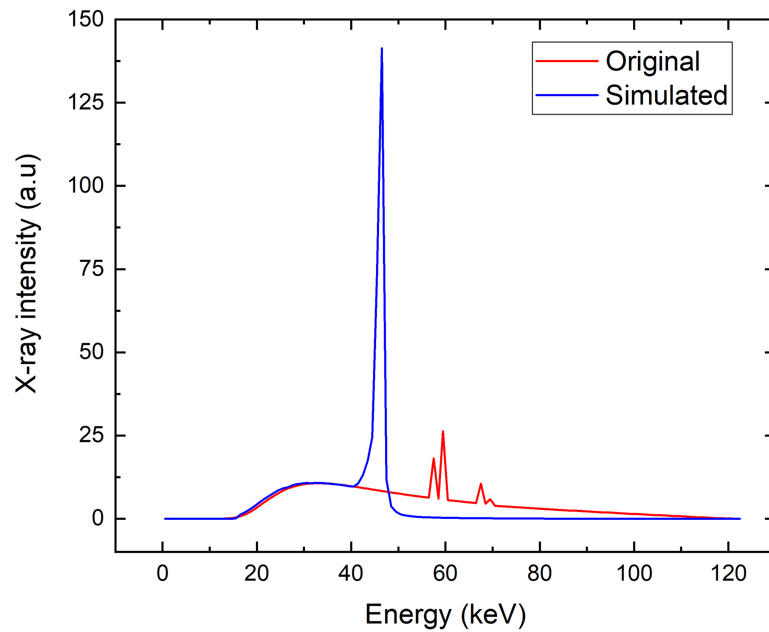

Figure 5.22: X-ray spectrum simulated for common parameters characterizing the electronic circuit, $t_s = 16$ ns (blue). The original X-ray spectrum is plotted for comparison (red).

not recognized by the electronics. Inasmuch as the used X-ray spectrum shows very low intensity below 16 keV, this defect does not manifest in the calculated spectrum shown in figure 5.22. Case (B) represents the photon with energy larger than the threshold. As soon as the collected charge is greater than the threshold, the trigger starts and samples for the sampling time t_s (blue bar), after which the charge is collected (marked with x). Since the collection terminates after the transit time, the spectral profile is nearly linear and without the ballistic deficit being only slightly reduced in terms of energy due to the RC time, which, in our case, is much longer than the sampling time, and its effect is negligible. Case (C) represents the high-energy X-ray photons with energy much larger than the threshold. The threshold is crossed early in the rising part of the curve, and collection after the sampling time occurs before saturation. This results in collection before the electron reaches the anode, and ballistic deficits appear. This results in a low-quality spectrum. This fact is well documented in figure 5.24, where we show the charge collection efficiency of the X-ray photon absorbed near the cathode. The collected charge dependency on the excited charge is calculated using equation (5.15). We marked three energy regions in figure 5.24 showing significant deviations from the optimum curve. The first region, with energy less than about 16 keV, does not contribute to charge collection. The reason is the energy threshold of 16 keV, which is not overcome by these photons (this corresponds to the photon energy marked with (A) in figure 5.24). The second region of 16–45 keV shows a nearly linear profile, which is only slightly reduced relative to the optimum. These photons are collected, showing correspondingly reduced collected charge (the collection of photons, marked with (B), from this region, is shown in figure 5.23). The third region is for high-energy photons with an energy greater than 45 keV. These photons reveal incomplete collection resulting from the large ballistic deficit. The collection of photons from this region, marked with (C), is shown in figure 5.23. The ideal full-charge collection is shown in figure 5.24 with a straight red line starting from the initial coordinates.

To obtain a better spectrum with the same low bias of 300 V, the sampling time should be appropriately extended. We followed such a scheme and calculated the X-ray spectrum in the presented model, extending the sampling time to 32 ns. The spectrum calculated under such conditions is plotted in figure 5.25. It is evident that the spectrum is much better in this case. The weak deviation from the original spectrum is mainly due to the neglected holes, and the finite lifetime of electrons that was used is 20 μs in these simulations.

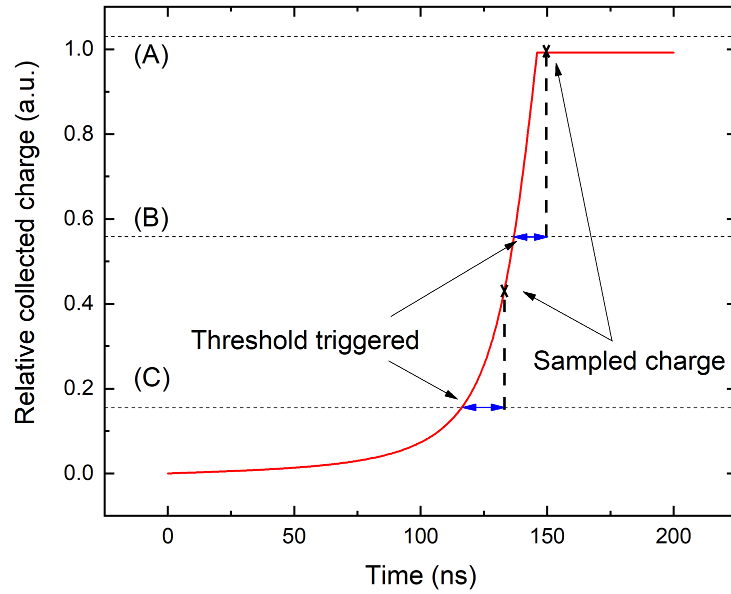

Figure 5.23: Analysis of sampled charge depending on photon energy. In case (A), the photon energy is lower than the threshold and the charge is not detected. In case (B, C), the threshold is triggered and the charge is sampled.

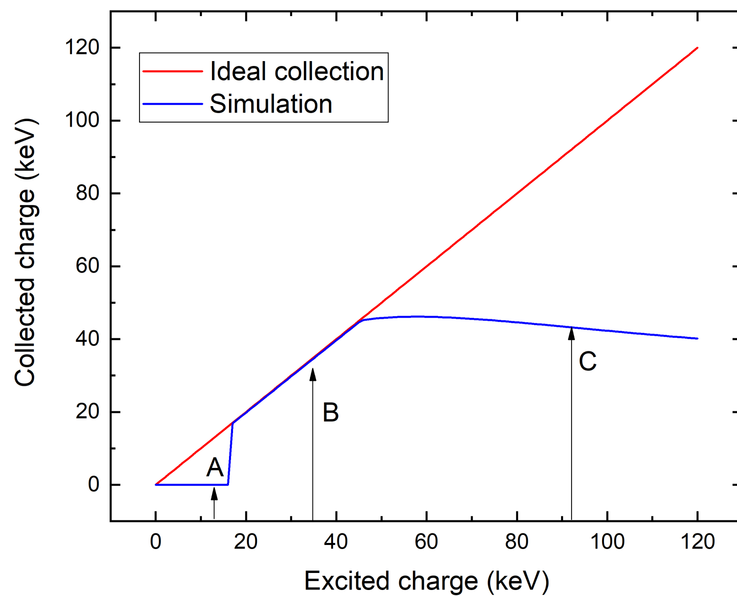

Figure 5.24: Dependence of the collected charge on the excited charge by X-ray photon absorbed near the cathode (blue) compared with the ideal full collection plotted with a straight line (red). Labels point to the threshold levels shown in figure 5.23.

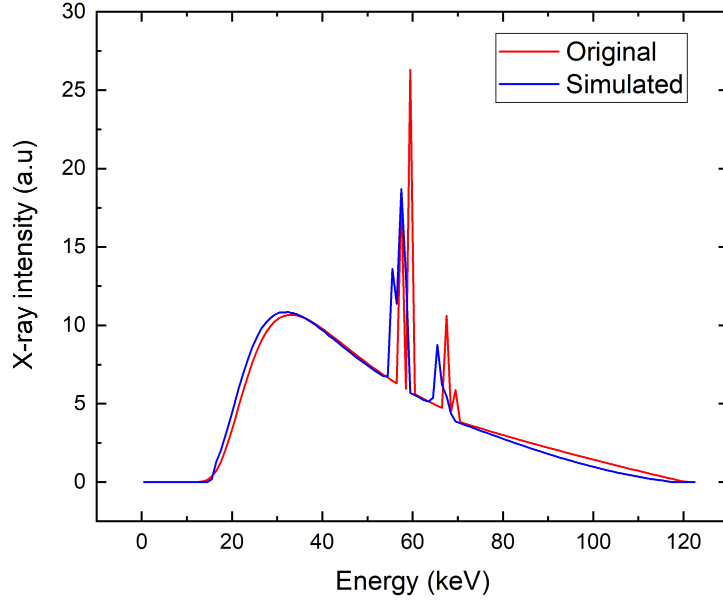

Figure 5.25: X-ray spectrum simulated for extended $t_s = 32$ ns (blue). The original X-ray spectrum is plotted for comparison (red).

5.2.4 Section conclusion

In this section, we studied polarization in CdZnTe radiation detectors induced by high-flux X-ray excitation. The electric field, measured using the Pockels effect, was modeled using a defect model solving drift-diffusion and Poisson's equations. We developed a procedure to determine the minimal bias for optimal counting performance acceptable for spectroscopy applications. A minimum bias of 300 V was found suitable for a 2-mm-thick detector in high-flux X-ray spectroscopy. Our numerical model predicted counting and spectroscopic behavior, showing X-ray spectrum warping due to delayed transit time caused by detector polarization. Decreased counts at low bias resulted from low-energy X-ray photons not reaching the threshold level, frequent pileups, and charge sharing. This model serves as a useful diagnostic tool for sensor characterization. We showed that CdZnTe has a good detection quality even at high-flux X-ray excitation. Results of this section were published in [115].

5.3 CdZnTeSe

In this section, the charge transport in the CZTS detector under pulsed and DC bias is studied using L-TCT. We observe a positive space charge that could be eliminated using pulsed bias. Charge transport parameters are obtained by Monte Carlo simulations of electron and hole transient currents. In this section, semi-insulating p-type CZTS sample with resistivity 1.1×10^{10} Ωcm, dimensions 6.9 mm × 5 mm × 1.7 mm, and selenium and zinc concentration of 4% and 10%, respectively, was studied by L-TCT. The CZTS single crystal was grown by the Traveling Heater Method at Brookhaven National Laboratory. The source CZT and CdSe materials of 6N purity were used for the CZTS synthesis and growth. The bandgap energy at room temperature is Eg ≈ 1.52 eV [116]. Two planar electrical contacts were prepared by electroless deposition of gold from a 1% gold chloride methanol-based solution [117]. It has been previously shown that gold forms a quasi-ohmic contact on CZT material [118], and it was successfully applied for CZTS detectors as well [119, 120].

The sample was characterized using L-TCT in combination with a pulsed bias, which allowed us to suppress the space charge formation and to study charge trapping effects on the current waveforms, thus enabling easier evaluation of the electron (hole) drift mobility carrier trapping and detrapping times [16, 83]. Electron (hole) current waveforms were measured by illuminating a semi-transparent cathode (anode) using a laser pulse with an above bandgap wavelength at 660 nm, which is absorbed in less than 1 μm under the illuminated electrode [121]. Illuminating the cathode/anode, the photogenerated holes/electrons are immediately collected on the exposed electrode, while the carriers with the opposite charge drift toward the other electrode and induce a transient current described by the Shockley-Ramo theorem (see section 2.8). The signal is amplified and recorded by a digital sampling oscilloscope (see section 4.1). A neutral density filter is used to ensure that the photogenerated charge is small enough not to affect the electric field inside the detector. Typically, a transient charge of hundreds of fC is used. The laser and bias pulse positions are synchronized as shown in figure 4.2 and characterized by a laser pulse delay (LPD), bias pulse width (BPW), depolarization time (DT), and pulsing period (PP) [16]. The laser pulse width has an FWHM of 2 ns. Decreasing the LPD to the micro-second time scale, the space charge formation induced by the carrier injection or depletion induced by non-ohmic contacts can be suppressed. This option simplifies the MC simulations offering the possibility to directly determine the lifetime of drifting carriers from the slope of the CWF [16, 37, 35].

For the numerical simulation, we combined two approaches routinely used by researchers to simulate charge-transport phenomena in semiconductors. That is, the solution of the DDE coupled with Poisson's equation was combined with the SRH model depicting the carrier (de)trapping. We used a custom code [87, 80], which allows us to conduct comprehensive simulations of all phenomena occurring in planar samples (see section 3.2). Nevertheless, the approach involves an extensive inclusion of spatial derivatives, which are time-consuming when called upon for calculating the transient currents. We thus combined our code with the MC method described in section 3.3. Here, we embed the electric field profile and recombination level occupancy calculated at specific conditions as defined by

the bias, delay time after biasing, etc. by DDE. MC is then used to calculate the current transient. The combination of both techniques makes the numerical treatment much more efficient and significantly reduces the computation run-time.

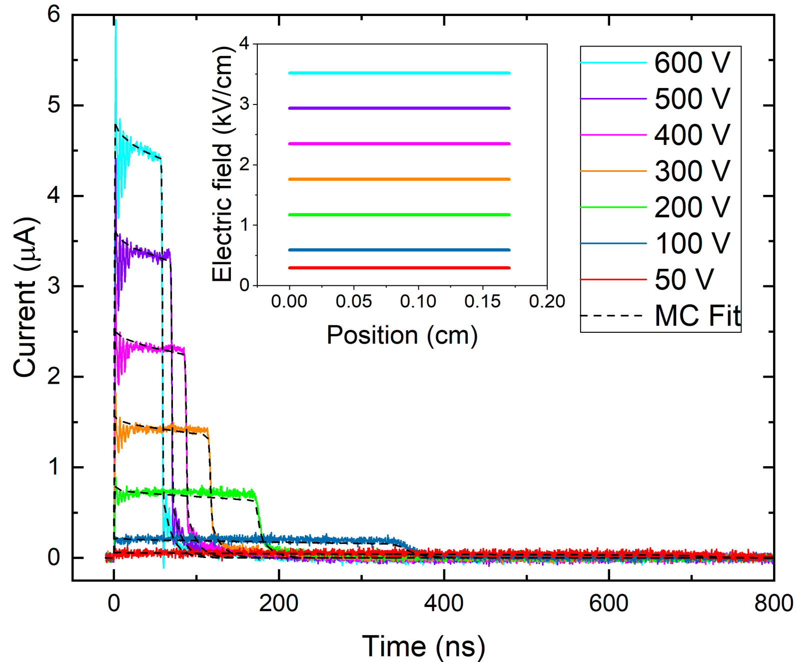

Figure 5.26: Pulsed bias dependence of the electron CWFs. The dashed lines represent the MC fit.

5.3.1 Results

The bias dependence of the electron and hole CWFs using a pulsed bias with pulsing parameters LPD = 80 us, BPW = 200 ms, and DT = 800 ms is shown in figure 5.26 and 5.28, respectively. Figure 5.27 and 5.29 show CWF normalized by respective bias. The LPD was chosen short enough to eliminate the space charge formation, and DT was long enough to suppress the memory effects between consecutive bias pulses. The detector is fully depolarized after each pulse period. No visible changes of the CWF shape were observed with an LPD from 80 μs up to 500 μs. We thus consider the detector unpolarized at each bias with a constant electric field for LPD = 80 μs. Without any space charge the transit time scales with bias and when CWFs time are multiplied by corresponding bias, their falling edge overlaps (see figures 5.27 and 5.29), which also verifies that no space charge is present. It is important to point out that the noise in figures 5.27 and 5.29 is more visible for lower biases because of the current normalization by corresponding bias. Fast oscillations apparent at the start of the electron waveforms in figure 5.27 and others in this section are generated by the adjoint

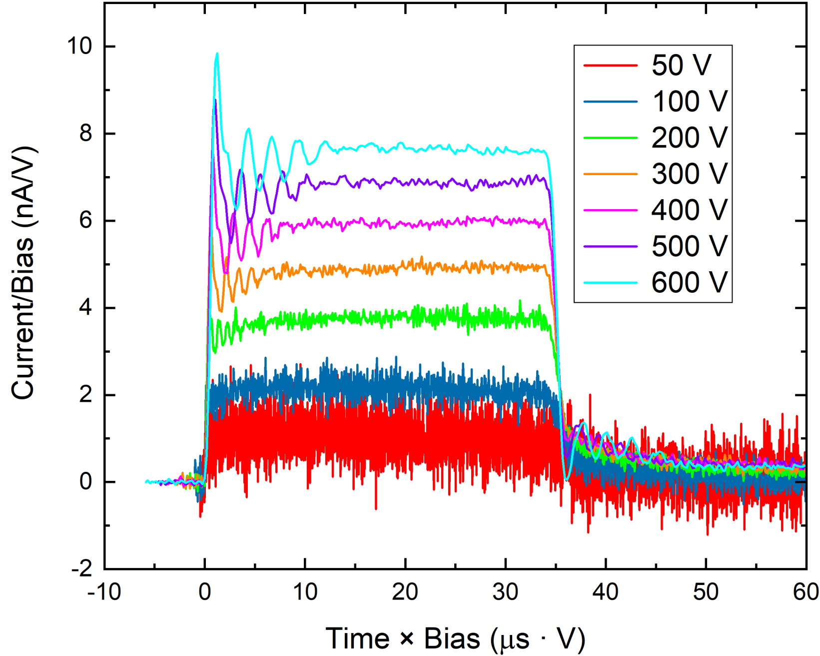

Figure 5.27: Pulsed bias dependence of the electron CWFs normalized by respective bias.

electronics. We do not study this feature in detail here. The relevant study is in section 5.1. The black dashed lines in figures 5.26 and 5.28 as well as in all consecutive figures are the MC fits, which are discussed later in the text.

Figure 5.30 shows the bias dependence of the electron CWFs for illumination of the cathode using a DC bias with laser pulsing period of 1 s. The dashed lines represent the MC simulations. Before measuring CWFs the detector became fully polarized in less than one second and retained a stable space charge during the measurements. The inset in figure 5.30 shows the bias dependence of the electric field profile within the detector, which reveals a strong electric field dependence on position inside the detector with a nearly zero electric field under the anode. Figure 5.31 shows the evolution of the electron CWFs under a -400 V pulsed bias using an LPD ranging from 80 μs up to 200 ms and PP = 1 s. The corresponding MC simulation is shown by the dashed line. Current waveforms were also measured in the range of laser pulse delay 80 μs–500 μs. Since no visible change was observed using an LPD < 500 μs, the data are not shown in figures 5.31 and 5.33. We found that the detector remains fully depolarized in the LPD interval of 80 $\mu s - 500$ μs with no apparent space-charge formation, and the CWFs are only slightly damped due to the charge trapping. CZTS material shows long-term stability in the range of pulsed and DC biases used in our experiments. No material change was observed after many hours of applied DC bias, and repeatable results for the L-TCT experiments were measured. The main difference between DC and pulsed bias is the DT, which allows the elimination of the space charge. By using short BPW and long DT, the detector polarization can be prevented. The mea-

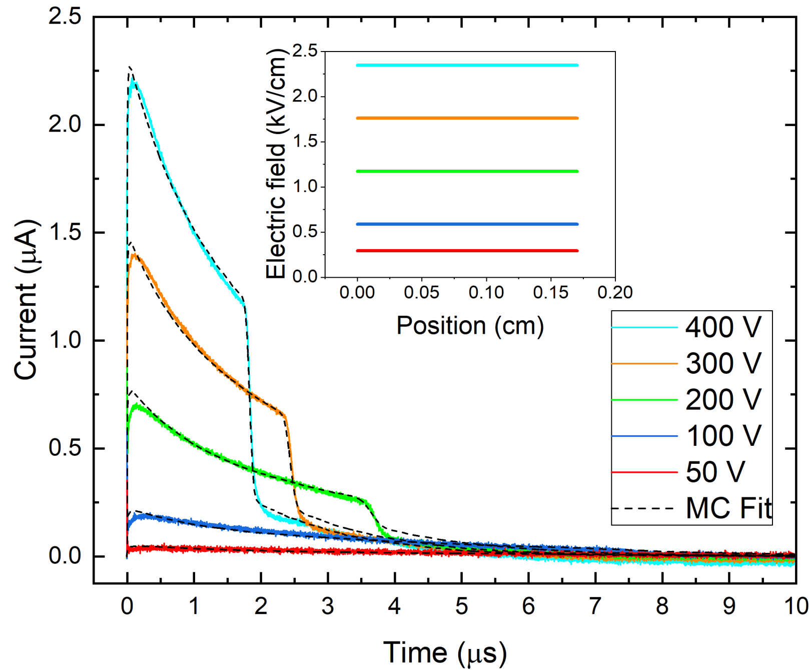

Figure 5.28: Pulsed bias dependence of the hole current waveforms. The dashed lines represent the MC fit.

surements with DC and pulsed bias are otherwise the same. The space-charge formation is caused by the redistribution of charge on the energy levels, and a repeatable result of the L-TCT experiment was measured after many hours of applied DC bias. The detector reveals gradual polarization for an LPD > 500 μs, which causes the corresponding tilting of the CWF. The polarization saturates around LPD $= 200$ ms when the electric field reaches almost zero value under the illuminated anode. The inset in figure 5.31 shows the LPD dependence of the electric field profile obtained by MC simulations, which correlates with the space charge formation.

Analogous experiments illuminating the anode were performed to measure the CWF for holes. Figure 5.32 shows the DC bias dependence of the hole CWF with a laser pulsing period of 1 s, and the inset in figure 5.32 shows the electric field obtained from MC simulations. The hole cloud generated under the illuminated anode drifts at the beginning through the area with a relatively low electric field, which amplifies the surface recombination due to the low drift velocity (see equation 2.64). The low electric field is also responsible for the carrier cloud broadening, which creates the wide tail of the CWF. Figure 5.33 shows the evolution of the hole CWFs under a 400 V pulsed bias using an LPD ranging from 80 μs up to 200 ms and PP $= 1$ s. The dashed lines represent MC simulations. The inset in figure 5.33 shows the evolution of the electric field profile dependence on the LPD as obtained by MC simulations. Space charge density corresponding to electric field profile evolution is shown if figure 5.34. We note that the electric field profiles deduced both from the electron and hole L-TCT signals are identical

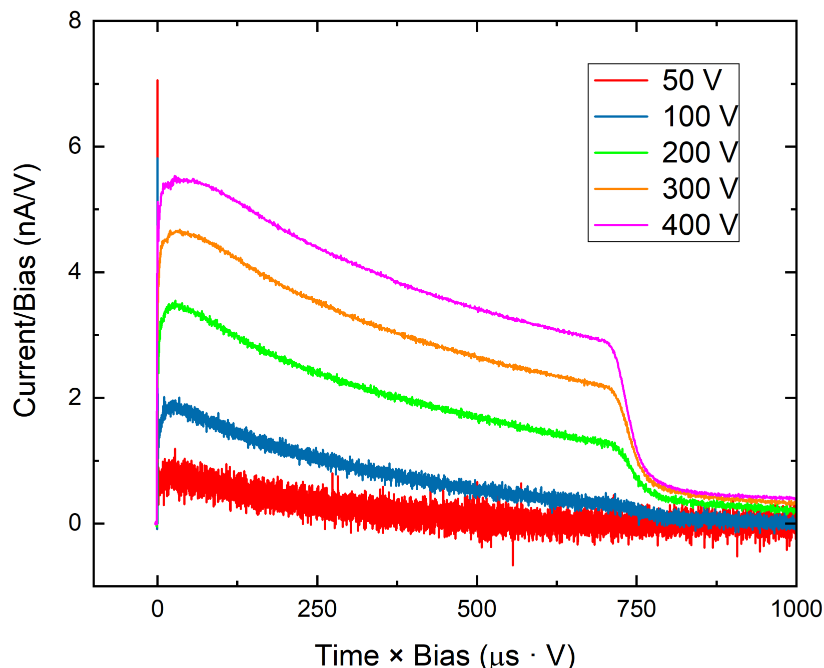

Figure 5.29: Pulsed bias dependence of the hole CWFs normalized by respective bias.

within the experimental error. This observation verifies our model and affirms the validity of the technique for the characterization of transport properties for both carrier types. The nearly constant depth at which the electric field profiles cross (see inset in figures 5.31 and 5.33) stems from the applied bias (-400 V), which requires a fixed value of the electric field integral over the sample thickness. Since the electric field profile is an almost linear function, the profiles intersect at nearly the same point.

5.3.2 Model

To describe the electron and hole charge transport properties in the CZTS sample, a combination of custom MC simulation with a program solving 1D coupled Poisson's equation and DDE were used. The electric field profile and level occupancies were calculated at specific conditions as defined by the bias, delay time after biasing, etc., by DDE and inserted into the MC simulation, which was then used to calculate the current waveforms. Three defect levels, which were sufficient to describe all observed effects, were obtained by fits based on the SRH model (see section 2.6). A schematic of the energy levels is shown in figure 5.35. We evaluated one dominant recombination level with energy $E_t = E_C - 0.73$ eV, with a concentration of $N_t = 7.3 \times 10^{11}$ cm^{-3} and with electron and hole capture cross-section $\sigma_e = 3.5 \times 10^{-14}$ cm^2 and $\sigma_h = 6.5 \times 10^{-14}$ cm^2, respectively. The redistribution of charge carriers on this deep level is responsible for space-charge formation inside the detector. In addition, one shallow electron trap and one shal-

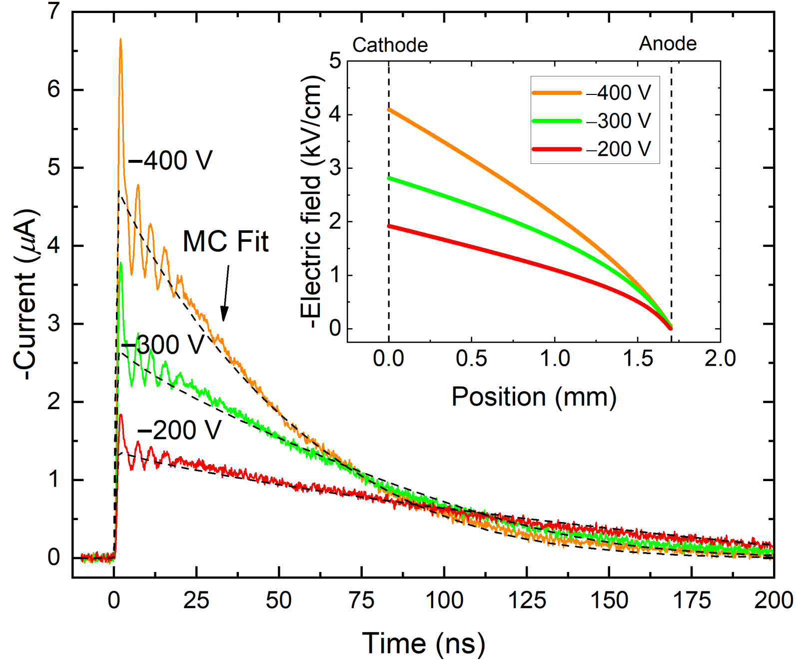

Figure 5.30: DC bias dependence of the electron current waveforms. Inset shows respective electric field profiles. The dashed lines plot the MC fit.

low hole trap were added. Carrier trapping and detrapping processes on shallow levels were characterized by the trapping time τ_T and detrapping time τ_D (see section 2.6). The shallow electron trap is characterized by trapping and detrapping time $\tau_{eTS} = 300$ ns and $\tau_{eDS} = 10$ ns, respectively, and the shallow hole trap is characterized by trapping and detrapping time $\tau_{hTS} = 4$ μs and $\tau_{hDS} = 1.2$ μs. Comparable parameters of shallow traps can be found for CdTe and CdZnTe in ref. [83]. The shallow traps are responsible for the charge delay and widening of the CWF fall edge. The energy and concentration of these shallow levels cannot be determined using MC simulation, since there is not enough information conveyed from the L-TCT data, and only the trapping and detrapping times can be determined. We used the Fermi level position in the bulk $E_F = E_C - 0.73$ eV corresponding to the measured sample resistivity of 1.1×10^{10} Ωcm. The contact properties are defined within the drift-diffusion model [87] by the fitted band bending $V_B = 90$ meV evoking the electron (hole) depletion (injection), respectively. In our case, the hole injection is caused by the type of electrical contact. We take advantage of the hole injection to determine parameters for the deep recombination level. By using different contact preparation techniques or contact material, the hole injection can be decreased, and the space charge can be decreased. The search for the ideal contact preparation technology optimizing the Schottky barrier is beyond the scope of this thesis. The Fermi level at the surface is then fixed on both sides at. The electron and hole drift mobility obtained from MC simulations is $\mu_e = 830$ cm^2/Vs and $\mu_h = 40$ cm^2/Vs, respectively, and electron and hole lifetime connected with the recombination center are

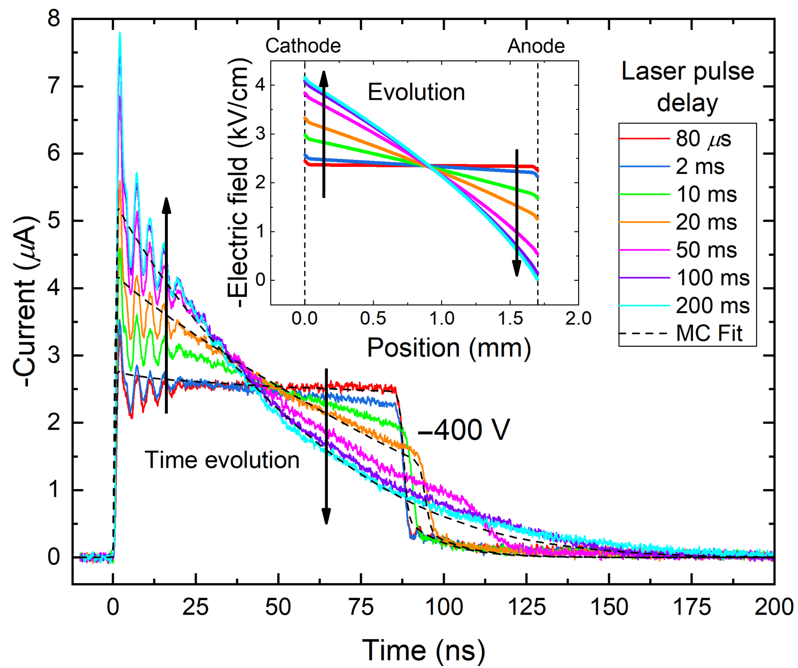

Figure 5.31: Evolution of the electron current waveforms at a pulsed bias of -400 V (arrows show the direction of the electric field evolution) depending on LPD. Inset represents the evolution of the electric field profile within the detector at several different values for the LPD. The dashed lines plot the MC fit.

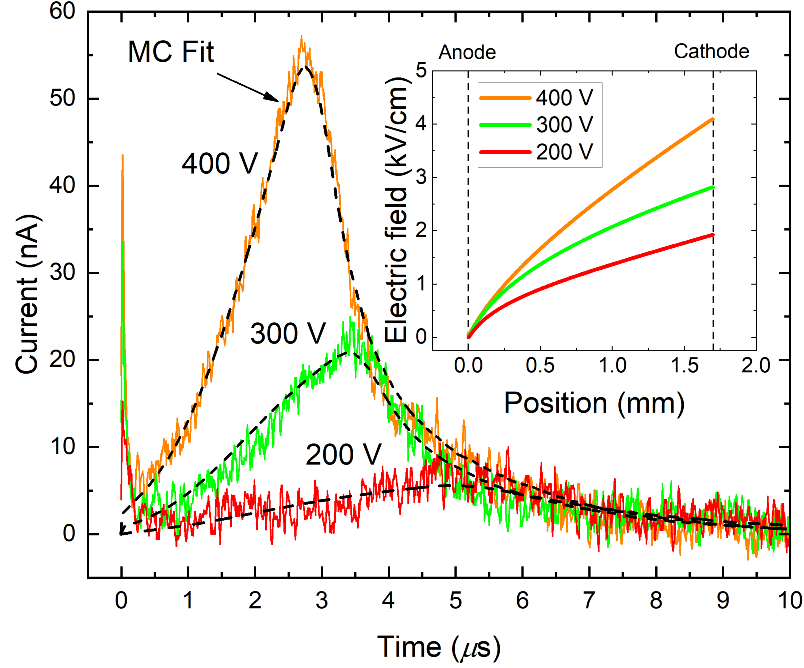

Figure 5.32: DC bias dependence of the measured hole current waveforms. Inset shows respective electric field profiles.

$\tau_e = 2.3$ μs and $\tau_h = 3.6$ μs, respectively. These are similar values of mobilities and lifetimes compared to CZT [83]. The recombination center causes losses of free-drifting charge, leading to decays in the CWF, which are visible in 5.26 and 5.28. Thus the mobility-lifetime product of electrons and holes at pulsed bias is $(\mu\tau)_e = \mu_e \times \tau_e = 1.9 \times 10^{-3}$ cm^2/V and $(\mu\tau)_h = \mu_h \times \tau_h = 1.4 \times 10^{-4}$ cm^2/V, respectively, which is similar to values in ref. [41]. The measured electron $(\mu\tau)_e$ product is relatively high, and together with the high $(\mu\tau)_h$ product for holes, the material is ready for the preparation of radiation detectors for different applications. Enhancement of the mu-tau product is a technological challenge and depends on the improvement of the crystal quality and reduction of native and extrinsic defects. Lowering the concentration of the recombination levels found in this thesis is expected to improve the detector quality.

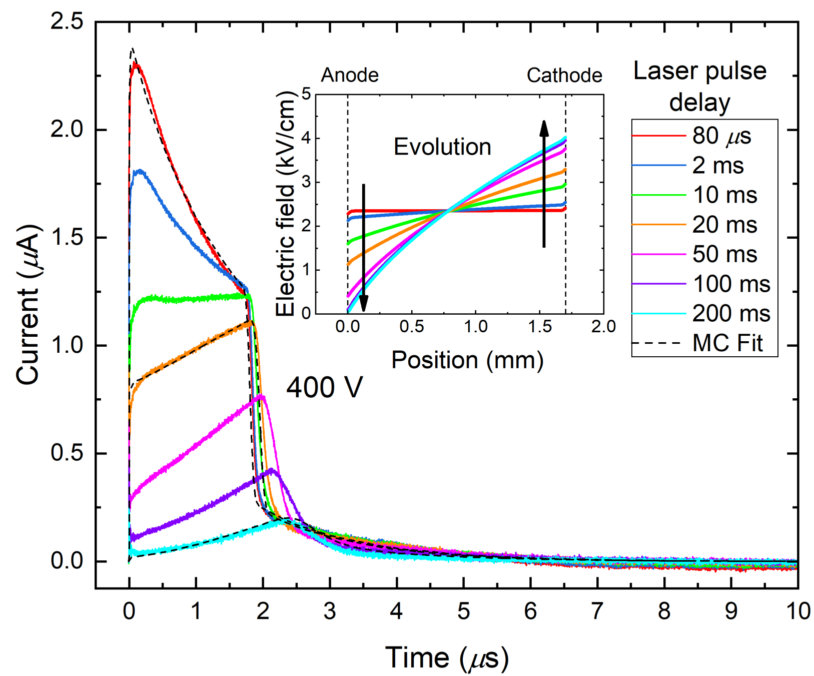

Figure 5.33: Evolution of hole current waveforms at a pulsed bias of 400 V depending on LPD. Inset represents the evolution of the electric field profile within the detector at several different values for the LPD. The dashed lines plot the MC fit.

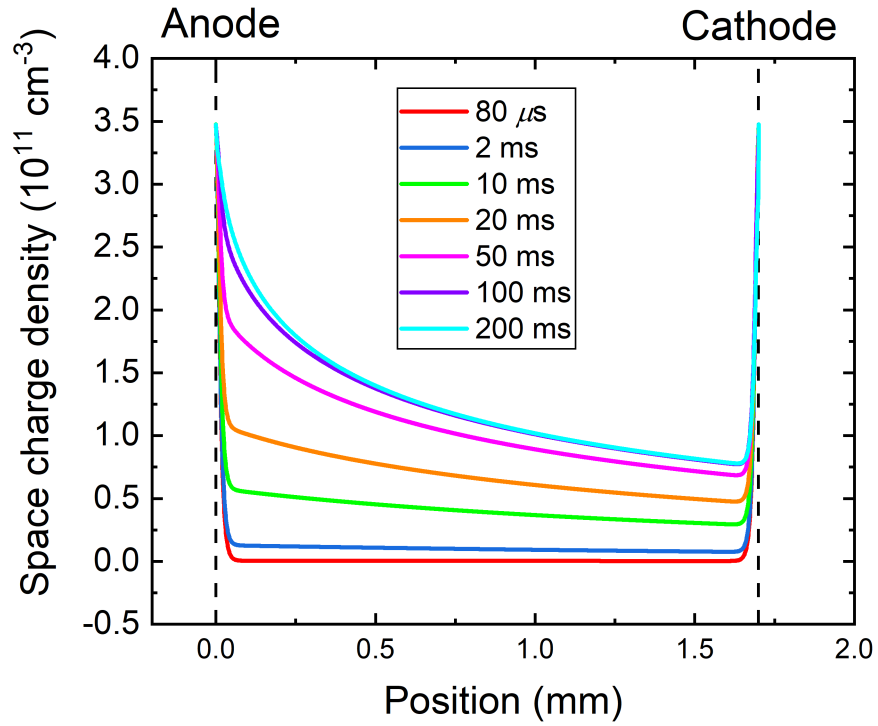

Figure 5.34: Evolution of space charge density at a pulsed bias of 400 V depending on LPD.

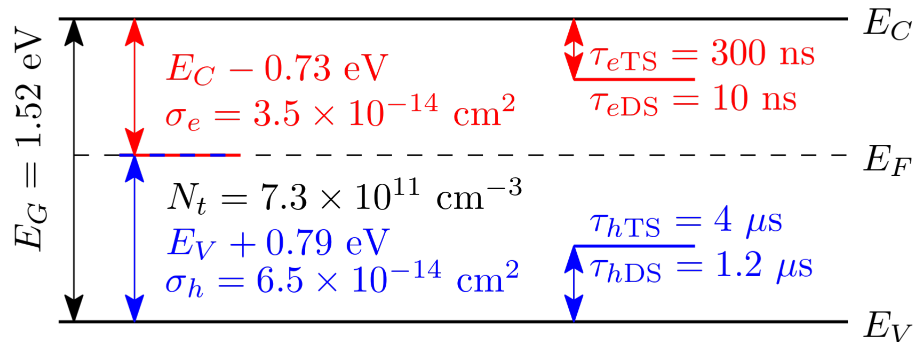

Figure 5.35: Schematic of the obtained energy levels with their parameters determined by numerical simulations of L-TCT waveforms. Red: electron traps. Blue: hole traps. Red-Blue: recombination level.

5.3.3 Spectroscopic measurements

In addition to L-TCT measurements, spectroscopic measurements with the same sample were performed using the setup described in 4.2. The radiation source of α-particles ^{241}Am (Energy of the main line 5480 keV, radioactive activity 8.4 kBq) was used for measurement.

Only the signal of electrons was measured. The collected charge is proportional to the channel's position with maximum counts. Measured α-spectra are shown in figure 5.36. In the inset, the position of the maximum of each spectrum is plotted against the corresponding bias. This dependence is fitted by the Hecht equation (2.69). The Hecht equation correctly describes measured dependence with typical saturation of collected charge. From Hecht equation we get $(\mu\tau)_e = 2.0 \times 10^{-3}$ cm^2/V, which matches the $(\mu\tau)_e$ obtained from L-TCT.

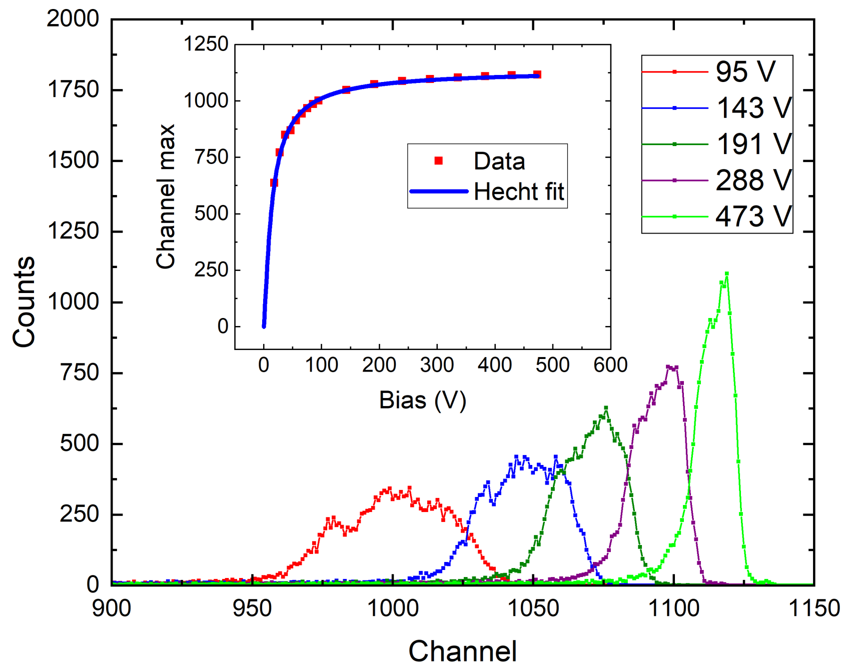

Figure 5.36: Pulse height spectra of α-source ^{241}Am. Inset: Bias dependence of collected charge and Hecht equation fit.

5.3.4 Discussion

The positive space charge formation in this sample comes from a weak injection of holes from the anode that creates a positive space charge by trapping on the hole recombination center distributed throughout the whole sample. Subsequently, the positive space charge starts to shield the electric field and damps the hole injection, forming a feedback loop that keeps the electric field almost zero near the anode. The steady-state is assured by balancing the hole injection boosting the space charge formation, and screening of the electric field at the anode, which

damps the process of charging. The principle of electric field screening is independent of the applied bias so that the space charge is implicitly adjusted to a value sufficient to nearly screen the bias. The model consistently describes all data collected in the range of bias 50 V – 600 V used in our experiments. The process of the positive space charge formation stabilizes the anode screening at a time scale of 10 – 100 ms when the hole injection attenuates. This is observed as a saturation in the electric field evolution (see the insets of figures 5.31 and 5.33).

The presence of the space charge at DC bias prevents the standard evaluation of $\mu\tau$ product using Hecht equation fit [72]. Likewise, a more advanced procedure [72] incorporating the electric field profile inside the sample (see section 2.11) cannot be used since it builds on the charge transport mediated by purely drift current. In the hole injection regime, the electric field changes the sign and is almost zero under the anode in the DC bias due to the band bending combined with the positive space charge. Subsequently, integrals defining the CCE in respective formulas diverge. A significant contribution of diffusion current is demonstrated in figure 5.37, where the decomposition of electron and hole current into drift and diffusion components for a detector under 200 V DC bias is shown. The diffusion current prevails under the anode and decreases into the bulk where the drift component dominates. We note that both total electron and total hole current densities are not constant in the bulk due to the electron-hole recombination through the recombination level.

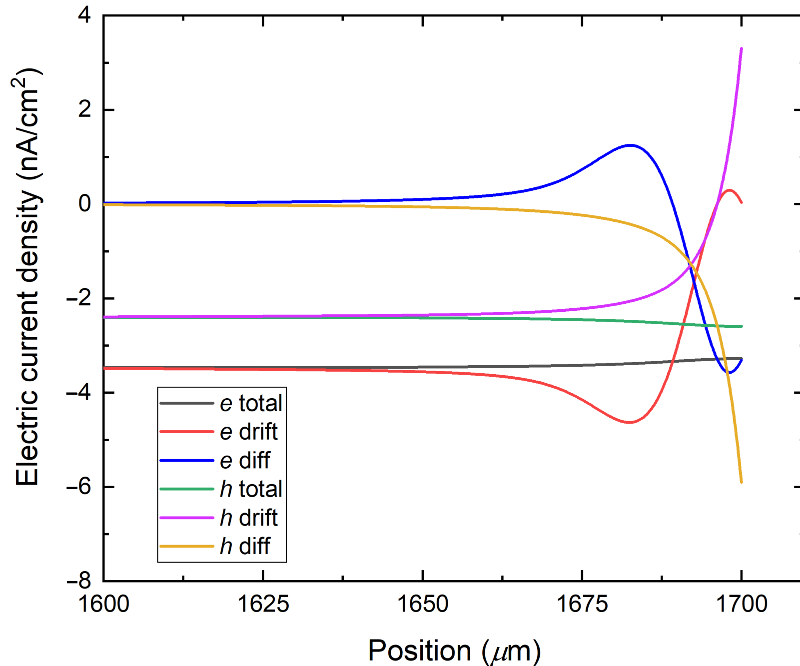

Figure 5.37: Decomposition of electron and hole currents into drift and diffusion components for the detector under DC bias at 200 V. The anode is on the right-hand side.

MC simulation was used to obtain electric field profile and transport parameters such as charge carrier mobility and trapping and detrapping time from the L-TCT experiment. L-TCT measurements with the pulsed bias, allows us to get the mobility and lifetime of electrons and holes separately. The electric field profile is also obtained, which is not accessible using the Hecht equation. The evaluation of transport parameters in a depolarized sample allows us to get material properties without the interference of space charge effects, which complicates the evaluation and affects the lifetime. In the case of positive space charge, the lifetime of holes is increased because of the filling of hole trap states by the hole injection. Oppositely, the lifetime of electrons decreases because of the depletion of electron trap states. In the case of recombination level considered in our model, both features occur in parallel. This phenomenon is demonstrated in figure 5.38, where the profiles of lifetime of electrons and holes in pulsed and DC bias 400 V are shown. In the pulsed bias, the lifetime is constant in the bulk and decreases for electrons and increases for holes near electrodes due to band bending. In DC bias, significant redistribution of charge carriers on recombination level causes a large increase of the lifetime of holes caused by saturation of the recombination level by injected holes and thus increases the hole lifetime by an order of magnitude compared to pulsed bias. Namely under the anode, there is a decrease of the lifetime of electrons caused by electron depletion from the recombination level. Since the depletion of electrons is not strong enough to completely negate the effects of the recombination level, the decrease of the electron lifetime is relatively small compared to the increase of hole lifetime. Lifetime depends on the location in the sample and on the applied bias. In the case of a negative space charge incurred by an electron injection from the cathode, the effect would be the opposite.

Significant SR was found using MC simulations for both electrons and holes. SR is caused by the presence of surface traps/recombination centers, which is difficult to evaluate by the L-TCT technique due to the short time that charge carriers spend in the thin layer under the surface. Here, the corresponding contribution to the current waveform is not visible. Thus, the effective parameter used to describe the surface imperfections collectively is surface recombination velocity s which defines the charge carrier losses before entering from the surface layer into the bulk (see section 2.10). In our case, the surface recombination velocity is independent of the laser intensity for all ranges used in this thesis. It is, however, dependent on the surface treatment, aging, handling and other surface-related conditions. Following is the discussion of theory of SR described in section 2.10. As it is apparent from equation (2.64), in the case of negligible surface recombination where $s \ll \mu U/L$, the onset of CWFs divided by respective bias $I(t=0)/U$ should start from the same bias-independent value. Alternatively, in the case of distinct surface recombination, $I(t=0)/U$ depends on the bias. This feature is seen in figure 5.27 and 5.29 where the CWFs of electrons and holes normalized by respective bias are shown. Distinct starts of the Current/Bias CWFs are clearly seen, proving the presence of significant surface recombination at both contacts. Bias dependence of the initial values of electron and hole current waveforms divided by respective bias taken from figures 5.27 and 5.29 are shown in figure 5.39. Fit using equation (2.64) is shown with red line for electrons and blue line for holes. The surface recombination velocity for electrons $s_e = 3.3 \times 10^6$ cm/s and

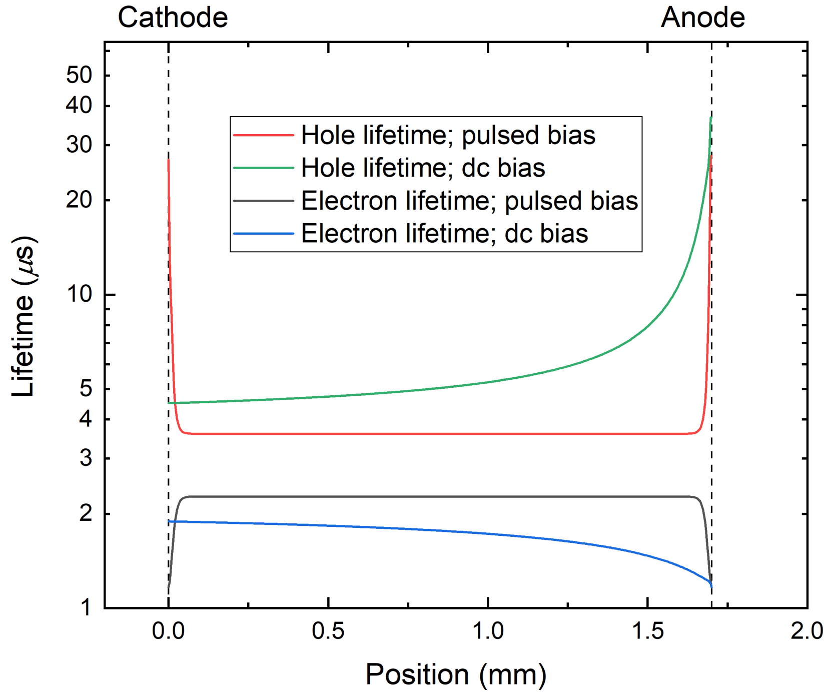

Figure 5.38: Profile of lifetime of electrons and holes under pulsed and DC bias 400 V.

holes $s_h = 9.8 \times 10^4$ cm/s, respectively, was evaluated. This represents an easy method to calculate the surface recombination directly from measured current waveforms without the need for MC simulation. This method serves as a simple way to detect the presence of surface recombination in the detector and helps with the MC simulations of CWF.

It should be noted that the positive space charge formation caused by the injecting anode shows distinct characteristics from the more frequently used model describing the positive space charge formation induced by an electron depletion affected by the blocking cathode [35, 37]. There appears especially an extensive inactive region, essentially a inactive layer, near the anode appearing due to the electric field screening by the excessive positive space charge localized under the cathode. Consequently, the L-TCT signal of holes cannot be measured, unlike in our case where the hole signal is detected. The nature of the defect responsible for the charging is different in the case of electron depletion. While the model presented in this thesis considers hole trapping where the injected holes are stored, depleted electrons induce the positive space charge by the electron trap detrapping of previously deposited electrons. While the hole injection and the rate of polarization are ruled by the Schottky barrier at the anode, the polarization induced by the electron depletion is defined by the electron trap energy expressed relative to the conduction band.

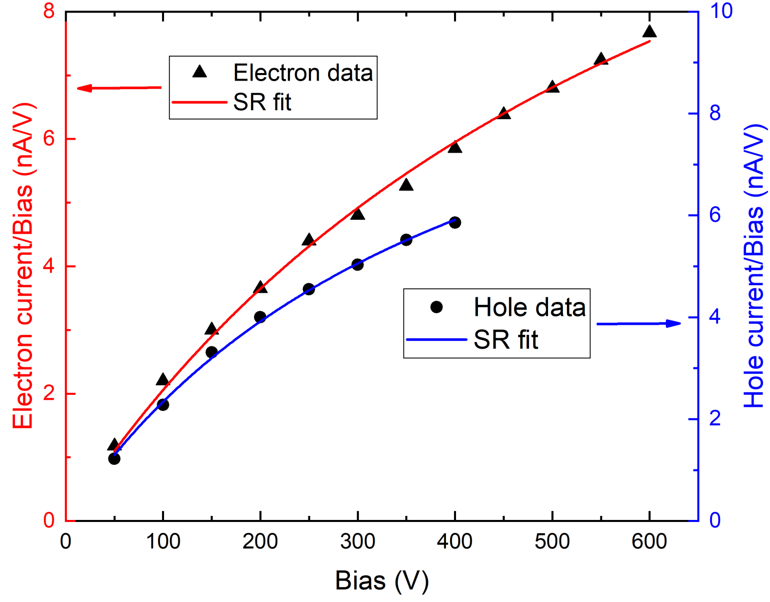

Figure 5.39: Bias dependence of initial values of current waveforms of electrons and holes under pulsed bias. Solid lines represent fit using equation (3), red for electrons and blue for holes.

5.3.5 Section conclusion

In this section, we measured electron and hole current transients in a CdZnTeSe detector using L-TCT under pulsed and DC bias. We developed a theoretical model based on the Shockley-Read-Hall model. We successfully applied it to analyze space charge formation. One dominant recombination level was identified with energy $E_t = E_C - 0.73$ eV, concentration 7.3×10^{11} cm^{-3}, and capture cross-sections $\sigma_e = 3.5 \times 10^{-14}$ cm^2 and $\sigma_h = 6.5 \times 10^{-14}$ cm^2 for electrons and holes, respectively. Monte Carlo simulations provided electron and hole transport parameters, including drift mobility, surface recombination velocity, and lifetime. We observed position-dependent lifetime variation in the detector due to hole injection under DC bias. The CdZnTeSe semiconductor exhibited good electron and hole transport properties, making it suitable for X-ray and gamma-ray detector fabrication. Results of this section were published in [71].

6. Conclusion

This thesis centers on the comprehensive investigation of charge transport phenomena in semiconducting radiation detectors, aiming to extend and improve existing techniques and methods.

In the theoretical part, the overview of the transport equations, generation-recombination model, and electrical contacts is described. Important terms which are used in numerical simulations and experimental measurements are defined. Theoretical current waveforms for the detector with deep trap and surface recombination are analyzed. In the chapter about numerical simulations, the solved equations are presented together with numerical methods to solve them. MC simulations and their combination with the numerical solution of coupled Poisson's equation together with the drift-diffusion equation are described. The stability of MC simulation with examples of MC simulation is presented.

In the experimental part, GaAs, CdZnTe, and CdZnTeSe are studied using several experimental techniques. This chapter is divided into three parts corresponding to the studied semiconductor material.

In the first part, we measured electron current transients in GaAs:Cr sensor using L-TCT in pulsed and DC bias and determined the time evolution of the space charge formation. At the time scale of 5 ms, we observed the simultaneous gradual formation of both the negative space charge localized near the cathode and the positive space charge near the anode. Electron lifetime $\tau_e = 150$ ns and electron drift mobility $\mu_d = 3650$ cm^2/Vs were evaluated from the MC simulations. All experimental results have been consistently explained by the model of variable hole conductivity caused by chromium in-diffusion. For the elimination of the internal electric field distortion, pulsed bias application was used. We also showed that using L-TCT, the internal electric field profile can be determined, giving direct feedback for the optimization of the growth technology. We demonstrated that L-TCT represents the non-destructive method for testing charge transport and internal electric properties in GaAs:Cr with much better precision than may be reached by other commonly used techniques. A similar approach may also be used for the investigation of other SI detector-grade materials.

In the second part, we studied the polarization phenomena in the CdZnTe radiation detector induced by high-flux X-ray excitation. The electric field warping measured using the Pockels effect was modeled with a defect model solving coupled drift-diffusion and Poisson's equation. We have developed a procedure to find minimal bias with optimal counting performance, which is still acceptable for spectroscopic applications, allowing for simpler electronic circuits and the easier portability of detector devices. We have defined the minimum bias of 300 V as still being acceptable for the application of a 2-mm-thick detector in X-ray spectroscopy at high-flux 20 Mcps/mm^2 excitation and analyzed its performance. We have developed a numerical model that predicts counting and spectroscopic behavior in a polarized detector. We have shown that the warping of the X-ray spectrum comes from the delayed transit time caused by detector polarization compared to the sampling time of the counting electronics. We have proven such a feature by calculating the spectrum with an extended sampling time of 32 ns. The decrease in measured counts at low bias is not mainly caused by carrier trap-

ping but by the ballistic deficit of low-energy X-ray photons, which do not cross the threshold level, frequent pileups, and charge sharing between pixels accentuated at the low electric field near the pixelated anode. The presented model may be used as a simple diagnostic tool in sensor characterization.

In the third part, we measured the electron and hole current transients in a CdZnTeSe detector using an L-TCT for pulsed and DC bias. A theoretical model of the space charge formation based on the Shockley-Read-Hall model was developed and successfully applied, assuming positive space charge formation due to the hole injection combined with the existence of the recombination level. We identified one dominant recombination level with energy of $E_t = E_C - 0.73$ eV, concentration 7.3×10^{11} cm^{-3}, electron and hole capture cross-section of $\sigma_e = 3.5 \times 10^{-14}$ cm^2 and $\sigma_h = 6.5 \times 10^{-14}$ cm^2, respectively, together with one shallow electron trap characterized by trapping and detrapping time $\tau_{eTS} = 300$ ns and $\tau_{eDS} = 10$ ns, respectively and one shallow hole trap characterized by trapping and detrapping time $\tau_{hTS} = 4$ μs and $\tau_{hDS} = 1.2$ μs. From Monte Carlo simulations, we obtained electron and hole transport parameters such as electron and hole drift mobility $\mu_e = 830$ cm^2/Vs and $\mu_h = 40$ cm^2/Vs, the electron and hole surface recombination velocity $s_e = 3.3 \times 10^6$ cm/s and $s_h = 9.8 \times 10^4$ cm/s, and the lifetime of electrons and holes at pulsed bias $\tau_e = 2.3$ μs us and $\tau_h = 3.6$ μs, respectively. Significant position dependence of the lifetime of electrons and holes inside the detector in DC bias due to hole injection is observed. We also proposed a simple technique for evaluating surface recombination directly from measured current waveforms without the need for numerical simulation. Good material quality is represented by the electron and hole mobility-lifetime product evaluated at pulsed bias $(\mu\tau)_e = \mu_e \times \tau_e = 1.9 \times 10^{-3}$ cm^2/V and $(\mu\tau)_h = \mu_h \times \tau_h = 1.4 \times 10^{-4}$ cm^2/V, respectively. We identified an identical electric field profile evaluated from the electron and hole transient currents, which validate the experimental methods used in this study. We showed that CdZnTeSe semiconductor has good electron and hole transport properties, and the single crystals are suitable for X-ray and gamma-ray detector fabrication.

These experimental results, together with numerical simulations and presented models, prove that MC simulations combined with the numerical solution of coupled Poisson's equation and drift-diffusion equation represent a powerful technique in determining the charge transport properties of semiconductors. Further improvements would include laser mapping of the detector surface and thus revealing the electric field profile inside the detector bulk. Extending 1D simulations into 3D would allow us to study inhomogeneities in semiconductor detectors.

Bibliography

[1] E. Velmre. Thomas Johann Seebeck (1770–1831). *Estonian Journal of Engineering*, (13):276–282, 2007.

[2] F. Laeri, U. Simon, M. Wark, and F. Schuth. *Host-Guest-Systems Based on Nanoporous Crystals.* Wiley & Sons, Incorporated, John, 2006.

[3] E. H. Hall. On a New Action of the Magnet on Electric Currents. *American Journal of Mathematics*, 2(3):287, sep 1879.

[4] I. Falconer. J. J. Thomson and the discovery of the electron. *Physics Education*, 32(4):226–231, jul 1997.

[5] A. Einstein. Über einen die erzeugung und verwandlung des lichtes betreffenden heuristischen gesichtspunkt. *Annalen der Physik*, 322(6):132–148, 1905.

[6] F. Bloch. Uber die Quantenmechanik der Elektronen in Kristallgittern. *Zeitschrift fur Physik*, 52(7-8):555–600, jul 1929.

[7] A. H. Wilson. *Semi-Conductors and Metals An Introduction to the Electron Theory of Metals.* Cambridge University Press, 2011.

[8] W. Schottky. On the Origin of the Super-Heterodyne Method. *Proceedings of the IRE*, 14(5):695–698, oct 1926.

[9] S. O. Kasap. *Principles of Electronic Materials and Devices.* McGraw-Hill Education, 2017.

[10] T. E. Schlesinger, J. E. Toney, H. Yoon, E. Y. Lee, B. A. Brunett, L. Franks, and R. B. James. Cadmium zinc telluride and its use as a nuclear radiation detector material. *Materials Science and Engineering: R: Reports*, 32(4-5):103–189, apr 2001.

[11] J. S. Blakemore. Semiconducting and other major properties of gallium arsenide. *Journal of Applied Physics*, 53(10):R123–R181, oct 1982.

[12] D. De Nobel. *Phase Equilibria and Semiconducting Properties of Cadmium Telluride.* 1958.

[13] A. J. Strauss. The physical properties of cadmium telluride. *Revue de Physique Appliquée*, 12(2):167–184, 1977.

[14] S. J. Moss and A. Ledwith. *Chemistry of the Semiconductor Industry.* Springer Netherlands, February 1989.

[15] M. C. Veale, S. J. Bell, D. D. Duarte, M. J. French, A. Schneider, P. Seller, M. D. Wilson, A. D. Lozinskaya, V. A. Novikov, O. P. Tolbanov, A. Tyazhev, and A. N. Zarubin. Chromium compensated gallium arsenide detectors for X-ray and gamma-ray spectroscopic imaging. *Nuclear Instruments and Methods in Physics Research Section A: Accelerators, Spectrometers, Detectors and Associated Equipment*, 752:6–14, jul 2014.

[16] E. Belas, R. Grill, J. Pipek, P. Praus, J. Bok, A. Musiienko, P. Moravec, O. Tolbanov, A. Tyazhev, and A. Zarubin. Space charge formation in chromium compensated GaAs radiation detectors. *Journal of Physics D: Applied Physics*, 53(47):475102, aug 2020.

[17] A. V. Tyazhev, D. L. Budnitsky, O. B. Koretskay, V. A. Novikov, L. S. Okaevich, A. I. Potapov, O. P. Tolbanov, and A. P. Vorobiev. GaAs radiation imaging detectors with an active layer thickness up to 1mm. *Nuclear Instruments and Methods in Physics Research Section A: Accelerators, Spectrometers, Detectors and Associated Equipment*, 509(1-3):34–39, aug 2003.

[18] G. I. Ayzenshtat, D. L. Budnitsky, O. B. Koretskaya, V. A. Novikov, L. S. Okaevich, A. I. Potapov, O. P. Tolbanov, A. V. Tyazhev, and A. P. Vorobiev. GaAs resistor structures for x-ray imaging detectors. *Nuclear Instruments and Methods in Physics Research Section A: Accelerators, Spectrometers, Detectors and Associated Equipment*, 487(1-2):96–101, jul 2002.

[19] J. Becker, M.W. Tate, K.S. Shanks, H.T. Philipp, J.T. Weiss, P. Purohit, D. Chamberlain, and S.M. Gruner. Characterization of chromium compensated GaAs as an x-ray sensor material for charge-integrating pixel array detectors. *Journal of Instrumentation*, 13(01):P01007–P01007, jan 2018.

[20] I. Chsherbakov, I. Kolesnikova, A. Lozinskaya, T. Mihaylov, V. Novikov, A. Shemeryankina, O. Tolbanov, A. Tyazhev, and A. Zarubin. Electron mobility-lifetime and resistivity mapping of GaAs:cr wafers. *Journal of Instrumentation*, 12(02):C02016–C02016, feb 2017.

[21] D. Greiffenberg, M. Andrä, R. Barten, A. Bergamaschi, P. Busca, M. Brückner, S. Chiriotti Alvarez, I. Chsherbakov, R. Dinapoli, P. Fajardo, E. Fröjdh, C. Lopez-Cuenca, A. Lozinskaya, M. Meyer, D. Mezza, A. Mozzanica, S. Redford, M. Ruat, C. Ruder, B. Schmitt, X. Shi, D. Thattil, G. Tinti, O. Tolbanov, A. Tyazhev, S. Vetter, A. Zarubin, and J. Zhang. Characterization of GaAs:cr sensors using the charge-integrating JUNGFRAU readout chip. *Journal of Instrumentation*, 14(05):P05020–P05020, may 2019.

[22] D. S. McGregor, R. A. Rojeski, G. F. Knoll, F. L. Terry, J. East, and Y. Eisen. Evidence for field enhanced electron capture by EL2 centers in semi-insulating GaAs and the effect on GaAs radiation detectors. *Journal of Applied Physics*, 75(12):7910–7915, jun 1994.

[23] T. Kubicki, K. Lübelsmeyer, J. Ortmanns, D. Pandoulas, O. Syben, M. Toporowsky, and W.J. Xiao. Calculation of the electric field in GaAs particle detectors. *Nuclear Instruments and Methods in Physics Research Section A: Accelerators, Spectrometers, Detectors and Associated Equipment*, 345(3):468–473, jul 1994.

[24] A. Cola, F. Quaranta, L. Vasanelli, C. Canali, A. Cavallini, F. Nava, and M.E. Fantacci. A study of the trap influence on the performance of semi-insulating GaAs detectors. *Nuclear Instruments and Methods in Physics*

Research Section A: Accelerators, Spectrometers, Detectors and Associated Equipment, 395(3):349–354, aug 1997.

[25] M. L. Williams and I. J. Donnelly. An investigation of electric field behaviour in semi-insulating GaAs using current pulses. *Journal of Physics D: Applied Physics*, 29(7):1997–2003, jul 1996.

[26] E. Bertolucci, M. Conti, G. Mettivier, M. Quattrocchi, P. Russo, A. Cola, F. Quaranta, L. Vasanelli, M.G. Bisogni, U. Bottigli, and M.E. Fantacci. Investigation on semi-insulating GaAs detectors using laser-induced current pulses. *Nuclear Instruments and Methods in Physics Research Section A: Accelerators, Spectrometers, Detectors and Associated Equipment*, 458(1-2):158–163, feb 2001.

[27] P. Russo and G. Mettivier. Characterization of 600um-thick SI-GaAs detectors for medical imaging. *Nuclear Instruments and Methods in Physics Research Section A: Accelerators, Spectrometers, Detectors and Associated Equipment*, 466(1):79–86, jun 2001.

[28] A. Tyazhev, V. Novikov, O. Tolbanov, A. Zarubin, M. Fiederle, and E. Hamann. Investigation of the current-voltage characteristics, the electric field distribution and the charge collection efficiency in x-ray sensors based on chromium compensated gallium arsenide. In Arnold Burger, Larry Franks, Ralph B. James, and Michael Fiederle, editors, *Hard X-Ray, Gamma-Ray, and Neutron Detector Physics XVI*. SPIE, sep 2014.

[29] S. D. Sordo, L. Abbene, E. Caroli, A. M. Mancini, A. Zappettini, and P. Ubertini. Progress in the Development of CdTe and CdZnTe Semiconductor Radiation Detectors for Astrophysical and Medical Applications. *Sensors*, 9(5):3491–3526, may 2009.

[30] A. E. Bolotnikov, G. S. Camarda, E. Chen, S. Cheng, Y. Cui, R. Gul, R. Gallagher, V. Dedic, G. De Geronimo, L. Ocampo Giraldo, J. Fried, A. Hossain, J. M. MacKenzie, P. Sellin, S. Taherion, E. Vernon, G. Yang, U. El-hanany, and R. B. James. CdZnTe position-sensitive drift detectors with thicknesses up to 5 cm. *Applied Physics Letters*, 108(9):093504, feb 2016.

[31] K. Kim, A. E. Bolotnikov, G. S. Camarda, A. Hossain, and R. B. James. Overcoming zn segregation in CdZnTe with the temperature gradient annealing. *Journal of Crystal Growth*, 442:98–101, may 2016.

[32] A. E. Bolotnikov, S. Babalola, G. S. Camarda, Y. Cui, R. Gul, S. U. Egarievwe, P. M. Fochuk, M. Fuerstnau, J. Horace, A. Hossain, F. Jones, K. H. Kim, O. V. Kopach, B. McCall, L. Marchini, B. Raghothamachar, R. Taggart, G. Yang, L. Xu, and R. B. James. Correlations between crystal defects and performance of CdZnTe detectors. *IEEE Transactions on Nuclear Science*, 58(4):1972–1980, aug 2011.

[33] P. Rudolph. Non-stoichiometry related defects at the melt growth of semiconductor compound crystals – a review. *Crystal Research and Technology*, 38(78):542–554, jul 2003.

[34] A. Raulo, G. Hennard, M. Sowinska, R. B. James, A. Fauler, J. Freier, A. Held, and M. Fiederle. Effects of annealing on bulk properties of CdTe detectors. *IEEE Transactions on Nuclear Science*, 60(5):3815–3823, oct 2013.

[35] Š. Uxa, E. Belas, R. Grill, P. Praus, and R. B. James. Determination of Electric-Field Profile in CdTe and CdZnTe Detectors Using Transient-Current Technique. *IEEE Transactions on Nuclear Science*, 59(5):2402–2408, oct 2012.

[36] Š. Uxa, R. Grill, and E. Belas. Evaluation of the mobility-lifetime product in CdTe and CdZnTe detectors by the transient-current technique. *Journal of Applied Physics*, 114(9):094511, sep 2013.

[37] A. Musiienko, R. Grill, J. Pekárek, E. Belas, P. Praus, J. Pipek, V. Dědič, and H. Elhadidy. Characterization of polarizing semiconductor radiation detectors by laser-induced transient currents. *Applied Physics Letters*, 111(8):082103, aug 2017.

[38] M. Rejhon, J. Franc, V. Dědič, J. Pekárek, U. N. Roy, R. Grill, and R. B. James. Influence of deep levels on the electrical transport properties of CdZnTeSe detectors. *Journal of Applied Physics*, 124(23):235702, dec 2018.

[39] R. Gul, U. N. Roy, G. S. Camarda, A. Hossain, G. Yang, P. Vanier, V. Lordi, J. Varley, and R. B. James. A comparison of point defects in Cd1-xZnxTe1-ySey crystals grown by Bridgman and traveling heater methods. *Journal of Applied Physics*, 121(12):125705, mar 2017.

[40] U. N. Roy, A. E. Bolotnikov, G. S. Camarda, Y. Cui, A. Hossain, K. Lee, W. Lee, R. Tappero, G. Yang, R. Gul, and R. B. James. High compositional homogeneity of CdTexSe1-x crystals grown by the bridgman method. *APL Materials*, 3(2):026102, feb 2015.

[41] U. N. Roy, G. S. Camarda, Y. Cui, and R. B. James. High-resolution virtual frisch grid gamma-ray detectors based on as-grown CdZnTeSe with reduced defects. *Applied Physics Letters*, 114(23):232107, jun 2019.

[42] R. Triboulet and P. Siffert. *CdTe and related compounds*. Elsevier, 2010.

[43] S. U. Egarievwe, U. N. Roy, C. A. Goree, B. A. Harrison, J. Jones, and R. B. James. Ammonium fluoride passivation of CdZnTeSe sensors for applications in nuclear detection and medical imaging. *Sensors*, 19(15):3271, jul 2019.

[44] T. E. Schlesinger and R. B. James. *Semiconductors for Room Temperature Nuclear Detector Applications*, volume 43. of *Semiconductors and Semimetals*. Elsevier Science, September 1995.

[45] T. Takahashi and S. Watanabe. Recent progress in CdTe and CdZnTe detectors. *IEEE Transactions on Nuclear Science*, 48(4):950–959, aug 2001.

[46] N. W. Ashcroft. *Solid state physics*. Holt, Rinehart and Winston, 1976.

[47] P. S. Dutta. Bulk Growth of Crystals of III-V Compound Semiconductors. In *Comprehensive Semiconductor Science and Technology*, pages 36–80. Elsevier, 2011.

[48] A. Castaldini, A. Cavallini, B. Fraboni, P. Fernandez, and J. Piqueras. Deep energy levels in CdTe and CdZnTe. *Journal of Applied Physics*, 83(4):2121–2126, feb 1998.

[49] S. T. Pantelides. Theory of defect complexes. In *Defect Complexes in Semiconductor Structures*, pages 75–84. Springer Berlin Heidelberg, 1983.

[50] U. Roessler. Systematics of semiconductor data. In *New Data and Updates for I-VII, III-V, III-VI and IV-VI Compounds*, pages 1–51. Springer Berlin Heidelberg, 2008.

[51] W. Orellana, E. Menéndez-Proupin, and M. A. Flores. Self-compensation in chlorine-doped CdTe. *Scientific Reports*, 9(1), jun 2019.

[52] G. Mandel. Self-compensation limited conductivity in binary semiconductors. i. theory. *Physical Review*, 134(4A):A1073–A1079, may 1964.

[53] O. Panchuk, A. Savitskiy, P. Fochuk, Y. Nykonyuk, O. Parfenyuk, L. Shcherbak, M. Ilashchuk, L. Yatsunyk, and P. Feychuk. IV group dopant compensation effect in CdTe. *Journal of Crystal Growth*, 197(3):607–611, feb 1999.

[54] W. Shockley and W. T. Read. Statistics of the recombinations of holes and electrons. *Physical Review*, 87(5):835–842, sep 1952.

[55] S. Seto, A. Tanaka, Y. Masa, and M. Kawashima. Chlorine-related photoluminescence lines in high-resistivity cl-doped CdTe. *Journal of Crystal Growth*, 117(1-4):271–275, feb 1992.

[56] J. Pousset, I. Farella, S. Gambino, and A. Cola. Subgap time of flight: A spectroscopic study of deep levels in semi-insulating CdTe:cl. *Journal of Applied Physics*, 119(10):105701, mar 2016.

[57] G. F. Knoll. *Radiation Detection and Measurement*. John Wiley & Sons, August 2010.

[58] C. Hamaguchi. *Basic Semiconductor Physics*. Springer Berlin Heidelberg, 2010.

[59] A. Jüngel. Drift-diffusion equations. In *Transport Equations for Semiconductors*, pages 1–29. Springer Berlin Heidelberg, 2009.

[60] S. M. Sze. *Physics of semiconductor devices*. J. Wiley and Sons, 1969.

[61] D. J. Griffiths. *Introduction to Electrodynamics*. Cambridge University Pr., August 2017.

[62] R. Grill, J. Franc, H. Elhadidy, E. Belas, Š. Uxa, M. Bugar, P. Moravec, and P. Hoschl. Theory of deep level spectroscopy in semi-insulating CdTe. *IEEE Transactions on Nuclear Science*, 59(5):2383–2391, oct 2012.

[63] A. Ruzin. Simulation of schottky and ohmic contacts on CdTe. *Journal of Applied Physics*, 109(1):014509, jan 2011.

[64] W. Shockley. Currents to Conductors Induced by a Moving Point Charge. *Journal of Applied Physics*, 9(10):635–636, oct 1938.

[65] L. Reggiani, editor. *Hot-Electron Transport in Semiconductors*. Springer Berlin Heidelberg, 1985.

[66] Z. He. Review of the shockley–ramo theorem and its application in semiconductor gamma-ray detectors. *Nuclear Instruments and Methods in Physics Research Section A: Accelerators, Spectrometers, Detectors and Associated Equipment*, 463(1-2):250–267, may 2001.

[67] W. Riegler and G. A. Rinella. Point charge potential and weighting field of a pixel or pad in a plane condenser. *Nuclear Instruments and Methods in Physics Research Section A: Accelerators, Spectrometers, Detectors and Associated Equipment*, 767:267–270, dec 2014.

[68] G. Bertolini and A. Coche. *Semiconductor Detectors*. Elsevier Science, 1968.

[69] A. Levi, M. M. Schieber, and Z. Burshtein. Carrier surface recombination in HgI2 photon detectors. *Journal of Applied Physics*, 54(5):2472–2476, may 1983.

[70] K. Suzuki and H. Shiraki. Evaluation of surface recombination velocity of CdTe radiation detectors by time-of-flight measurements. In *2008 IEEE Nuclear Science Symposium Conference Record*. IEEE, oct 2008.

[71] J. Pipek, M. Betušiak, E. Belas, R. Grill, P. Praus, A. Musiienko, J. Pekarek, U. N. Roy, and R. B. James. Charge transport and space-charge formation in Cd1-xZnxTe1-ySey radiation detectors. *Physical Review Applied*, 15(5):054058, may 2021.

[72] R. Matz and M. Weidner. Charge collection efficiency and space charge formation in CdTe gamma and x-ray detectors. *Nuclear Instruments and Methods in Physics Research Section A: Accelerators, Spectrometers, Detectors and Associated Equipment*, 406(2):287–298, apr 1998.

[73] K. Hecht. Zum Mechanismus des lichtelektrischen Primärstromes in isolierenden Kristallen. *Zeitschrift für Physik*, 77(3-4):235–245, mar 1932.

[74] W. van Roosbroeck and W. Shockley. Photon-radiative recombination of electrons and holes in germanium. *Physical Review*, 94(6):1558–1560, jun 1954.

[75] D. Vasileska, S. M. Goodnick, and G. Klimeck. *Computational Electronics Semiclassical and Quantum Device Modeling and Simulation*. Taylor & Francis Group, 2017.

[76] H. K. Gummel. A self-consistent iterative scheme for one-dimensional steady state transistor calculations. *IEEE Transactions on Electron Devices*, 11(10):455–465, oct 1964.

[77] W. H. Press, S. A. Teukolsky, W. T. Vetterling, and B. P. Flannery. *Numerical Recipes 3rd Edition: The Art of Scientific Computing*. Cambridge University Pr., September 2007.

[78] F. Bosisio, S. Micheletti, and R. Sacco. A discretization scheme for an extended drift-diffusion model including trap-assisted phenomena. *Journal of Computational Physics*, 159(2):197–212, apr 2000.

[79] G. Ghislotti, S. Pietralunga, L. Ripamonti, R. Sacco, S. Micheletti, and F. Bosisio. Time-resolved photocurrent and electric field measurements in high resistivity CdTe. *Journal of Applied Physics*, 87(1):322–328, jan 2000.

[80] R. Grill, E. Belas, J. Franc, M. Bugar, Š. Uxa, P. Moravec, and P. Hoschl. Polarization Study of Defect Structure of CdTe Radiation Detectors. *IEEE Transactions on Nuclear Science*, 58(6):3172–3181, dec 2011.

[81] C. Jacoboni and L. Reggiani. The Monte Carlo method for the solution of charge transport in semiconductors with applications to covalent materials. *Reviews of Modern Physics*, 55(3):645–705, jul 1983.

[82] J. Pipek. Charge transport in semiconducting radiation detectors. Master's thesis, Charles University, 2018.

[83] K. Suzuki, T. Sawada, and K. Imai. Effect of DC Bias Field on the Time-of-Flight Current Waveforms of CdTe and CdZnTe Detectors. *IEEE Transactions on Nuclear Science*, 58(4):1958–1963, aug 2011.

[84] W. E. Tefft. Trapping Effects in Drift Mobility Experiments. *Journal of Applied Physics*, 38(13):5265–5272, dec 1967.

[85] S. Kasap, K. O. Ramaswami, M. Z. Kabir, and R. Johanson. Corrections to the hecht collection efficiency in photoconductive detectors under large signals: non-uniform electric field due to drifting and trapped unipolar carriers. *Journal of Physics D: Applied Physics*, 52(13):135104, feb 2019.

[86] K. Suzuki, Y. Mishima, T. Masuda, and S. Seto. Simulation of the transient current of radiation detector materials using the constrained profile interpolation method. *Nuclear Instruments and Methods in Physics Research Section A: Accelerators, Spectrometers, Detectors and Associated Equipment*, 971:164128, aug 2020.

[87] K. Ridzonova, E. Belas, R. Grill, J. Pekarek, and P. Praus. Space-charge-limited photocurrents and transient currents in (cd,zn)te radiation detectors. *Physical Review Applied*, 13(6):064054, jun 2020.

[88] C. Canali, M. Martini, G. Ottaviani, A. Alberigi Quaranta, and K. R. Zanio. Characterization of high resistivity CdTe for gamma-ray detectors. *Nuclear Instruments and Methods*, 96(4):561–571, nov 1971.

[89] P. Praus, E. Belas, J. Bok, R. Grill, and J. Pekarek. Laser Induced Transient Current Pulse Shape Formation in (CdZn)Te Detectors. *IEEE Transactions on Nuclear Science*, 63(1):246–251, feb 2016.

[90] C. Szeles. CdZnTe and CdTe materials for x-ray and gamma ray radiation detector applications. *physica status solidi (b)*, 241(3):783–790, mar 2004.

[91] P. Praus, J. Kunc, E. Belas, J. Pekárek, and R. Grill. Charge transport in CdZnTe coplanar grid detectors examined by laser induced transient currents. *Applied Physics Letters*, 109(13):133502, sep 2016.

[92] A. Musiienko, P. Moravec, R. Grill, P. Praus, I. Vasylchenko, J. Pekarek, J. Tisdale, K. Ridzonova, E. Belas, L. Landová, B. Hu, E. Lukosi, and M. Ahmadi. Deep levels, charge transport and mixed conductivity in organometallic halide perovskites. *Energy & Environmental Science*, 12(4):1413–1425, 2019.

[93] A. Musiienko, J. Pipek, P. Praus, M. Brynza, E. Belas, B. Dryzhakov, M. H. Du, M. Ahmadi, and R. Grill. Deciphering the effect of traps on electronic charge transport properties of methylammonium lead tribromide perovskite. *Science Advances*, 6(37), sep 2020.

[94] D. C. Look. The electrical characterization of semi-insulating GaAs: A correlation with mass-spectrographic analysis. *Journal of Applied Physics*, 48(12):5141–5148, dec 1977.

[95] M. D. Sturge. Optical absorption of gallium arsenide between 0.6 and 2.75 eV. *Physical Review*, 127(3):768–773, aug 1962.

[96] S. Adachi. *Properties of Group-IV, III-V and II-VI Semiconductors*. Wiley, feb 2005.

[97] K. Taguchi, I. Blevis, and K. Iniewski. *Spectral Photon Counting Computed Tomography*. Taylor and Francis Group, 2022.

[98] S. Awadalla. *Solid-State Radiation Detectors*. Taylor and Francis Group, 2019.

[99] M. Prokesch, D. S. Bale, and C. Szeles. Fast high-flux response of CdZnTe x-ray detectors by optical manipulation of deep level defect occupations. *IEEE Transactions on Nuclear Science*, 57(4):2397–2399, aug 2010.

[100] I. Vasylchenko, R. Grill, M. Betušiak, E. Belas, P. Praus, P. Moravec, and P. Höschl. In and al schottky contacts comparison on p-type chlorine-doped CdTe. *Sensors*, 21(8):2783, apr 2021.

[101] J. J. McCoy, S. Kakkireni, Z. H. Gilvey, S. K. Swain, A. E. Bolotnikov, and K. G. Lynn. Overcoming mobility lifetime product limitations in vertical bridgman production of cadmium zinc telluride detectors. *Journal of Electronic Materials*, 48(7):4226–4234, apr 2019.

[102] P. Zambon. Dead time model for x-ray photon counting detectors with retrigger capability. *Nuclear Instruments and Methods in Physics Research Section A: Accelerators, Spectrometers, Detectors and Associated Equipment*, 994:165087, apr 2021.

[103] M. Bettelli, N. S. Amadè, D. Calestani, B. Garavelli, P. Pozzi, D. Macera, L. Zanotti, C. A. Gonano, M. C. Veale, and A. Zappettini. A first principle method to simulate the spectral response of CdZnTe-based x- and gamma-ray detectors. *Nuclear Instruments and Methods in Physics Research Section A: Accelerators, Spectrometers, Detectors and Associated Equipment*, 960:163663, apr 2020.

[104] I. Vasylchenko, R. Grill, E. Belas, P. Praus, and A. Musiienko. Charge sharing in (CdZn)te pixel detector characterized by laser-induced transient currents. *Sensors*, 20(1):85, dec 2019.

[105] Y. Kim, T. Lee, and W. Lee. Radiation measurement and imaging using 3d position sensitive pixelated CZT detector. *Nuclear Engineering and Technology*, 51(5):1417–1427, aug 2019.

[106] A. Buttacavoli, F. Principato, G. Gerardi, D. Cascio, G. Raso, M. Bettelli, A. Zappettini, P. Seller, M. C. Veale, and L. Abbene. Incomplete charge collection at inter-pixel gap in low- and high-flux cadmium zinc telluride pixel detectors. *Sensors*, 22(4):1441, feb 2022.

[107] O. Baussens, C. Ponchut, M. Ruat, M. Bettelli, S. Zanettini, and A. Zappettini. Characterization of high-flux cdznte withoptimized electrodes for 4th generation synchrotrons. In *n Proceedings of the 23rd International Workshop on Radiation ImagingDetectors*, 2022.

[108] K. Iniewski, M. Veale, and M. Bazalova-Carter. High-flux czt for new frontiers in computed tomography (ct), non-destructivetesting (ndt) and high-energy physics. In *Proceedings of the IEEE Transactions on Nuclear Science*, 2019.

[109] V. Dědič, J. Franc, M. Rejhon, R. Grill, J. Zázvorka, and P. J. Sellin. De-polarization of a CdZnTe radiation detector by pulsed infrared light. *Applied Physics Letters*, 107(3):032105, jul 2015.

[110] J. Franc, V. Dědič, M. Rejhon, J. Zázvorka, P. Praus, J. Touš, and P. J. Sellin. Control of electric field in CdZnTe radiation detectors by above-bandgap light. *Journal of Applied Physics*, 117(16):165702, apr 2015.

[111] I. Farella, G. Montagna, A. M. Mancini, and A. Cola. Study on instability phenomena in CdTe diode-like detectors. *IEEE Transactions on Nuclear Science*, 56(4):1736–1742, aug 2009.

[112] K. Iniewski. Performance characteristics of 250+ mcps/mm2 czt detector module for spectral computed tomography. In *Proceedings of the 5th Workshop on Medical Applications of Spectroscopic X-ray Detectors*, 2019.

[113] J. H. Hubbell and S. M. Seltzer. Tables of x-ray mass attenuation coefficients and mass energy-absorption coefficients 1 keV to 20 MeV for elements z = 1 to 92 and 48 additional substances of dosimetry interest. Technical report, 1995.

[114] K. Suzuki, S. Seto, T. Sawada, and K. Imai. Carrier transport properties of hpb cdznte and thm cdte:cl. In *Proceedings of the2001 IEEE Nuclear Science Symposium Conference Record (Cat. No.01CH37310)*, 2001.

[115] J. Pipek, R. Grill, M. Betušiak, and K. Iniewski. Modelling polarization effects in a CdZnTe sensor at low bias. *Sensors*, 23(12):5681, jun 2023.

[116] M. Rejhon, V. Dedic, L. Beran, U. N. Roy, J. Franc, and R. B. James. Investigation of deep levels in CdZnTeSe crystal and their effect on the internal electric field of CdZnTeSe gamma-ray detector. *IEEE Transactions on Nuclear Science*, 66(8):1952–1958, aug 2019.

[117] G. Benassi, L. Nasi, M. Bettelli, N. Zambelli, D. Calestani, and A. Zappettini. Strong mechanical adhesion of gold electroless contacts on CdZnTe deposited by alcoholic solutions. *Journal of Instrumentation*, 12(02):P02018–P02018, feb 2017.

[118] A. Musa, J. P. Ponpon, J. J. Grob, M. Hage–Ali, R. Stuck, and P. Siffert. Properties of electroless gold contacts on p-type cadmium telluride. *Journal of Applied Physics*, 54(6):3260–3268, jun 1983.

[119] U. N. Roy, G. S. Camarda, Y. Cui, R. Gul, G. Yang, J. Zazvorka, V. Dedic, J. Franc, and R. B. James. Evaluation of CdZnTeSe as a high-quality gamma-ray spectroscopic material with better compositional homogeneity and reduced defects. *Scientific Reports*, 9(1), may 2019.

[120] S. U. Egarievwe, U. N. Roy, E. O. Agbalagba, B. A. Harrison, C. A. Goree, E. K. Savage, and R. B. James. Optimizing CdZnTeSe frisch-grid nuclear detector for gamma-ray spectroscopy. *IEEE Access*, 8:137530–137539, 2020.

[121] P. Horodyský, R. Grill, and P. Hlídek. Band-edge photoluminescence in CdTe. *physica status solidi (b)*, 243(12):2882–2891, oct 2006.

[122] P. J. Mohr, D. B. Newell, and B. N. Taylor. CODATA recommended values of the fundamental physical constants: 2014. *Journal of Physical and Chemical Reference Data*, 45(4):043102, dec 2016.

List of Figures

1.1 Zinc-blende crystal structure [42]. 6
1.2 Point defects in binary compound semiconductor AB. C_A and C_B are impurity atoms at places of atom A and B. V_A, V_B are vacancies. A_B is antisite defect. $V_A - A_I$ is the Frenkel pair [50]. . 9

2.1 Scheme of the detector with simplification in 1D 16
2.2 The Shockley-Read-Hall model of generation and recombination processes. 20
2.3 Trapping and detrapping. 21
2.4 Band diagram of separated metal (left) and semiconductor (right) for $\Phi_M < \Phi_S$ [60]. 22
2.5 Band diagram of injecting Ohmic contact [60, 63]. 23
2.6 Band diagram of flat-band Ohmic contact [63]. 23
2.7 Band diagram of Schottky contact [60, 63]. 23
2.8 Normalized current waveforms for different values of trapping time 25
2.9 Detector with surface layer and bulk. The surface layer is much thinner than the bulk. Photogenerated charge Q_{00} is initially partially recombined, and only part Q_0 enters the bulk. 27
2.10 Bias dependence of ration of charge entering the bulk from the surface layer for different values of surface recombination velocity. 27
2.11 **Top left**: Current waveforms for the detector without surface recombination. **Top right**: Current waveforms for the detector with surface recombination. **Bottom left**: Current waveforms normalized by respective bias for detector without surface recombination. **Bottom right**: Current waveforms normalized by respective bias for a detector with surface recombination. 28
2.12 The detector scheme with generated charge at position x_0 by incident radiation. 30

3.1 Basic concept of Monte Carlo simulation. 35
3.2 Simulated current waveform of detector with one deep electron trap. 35
3.3 Dependence of MC simulation on the number of super particles. . 37
3.4 Dependence of MC simulation on time step size. It can be seen that time step shorter than 10 ns is needed to simulate CWF correctly. CWF for 50 ns (purple) and 100 ns (lime) have decreased amplitude to better show discrete steps. 38
3.5 Band diagram of electron trap level used in simulation. 39
3.6 Band diagram of the detector with flat-band anode and depleting Schottky cathode. 39
3.7 Band diagram of the detector with flat-band anode and injecting Ohmic cathode. 39
3.8 Electric field profile for detector with electron depletion under different DC biases. 41
3.9 Space charge density for detector with electron depletion under different DC biases. 41

3.10 Time evolution of electric field profile for detector with electron depletion for bias 50 V. 42
3.11 Time evolution of space charge density for detector with electron depletion for bias 50 V. 42
3.12 Time evolution of the mean space charge density for the detector with electron depletion for bias 50 V. 43
3.13 CWFs for detector with electron depletion for several DC biases. . 43
3.14 Time evolution of CWFs for detector with electron depletion for bias 50 V. 44
3.15 Electric field profile for the detector with electron injection under different DC biases. 45
3.16 Space charge density for the detector with electron injection under different DC biases. 46
3.17 Time evolution of electric field profile for the detector with electron injection for bias 50 V from 10 μs to 100 ms. 46
3.18 Time evolution of electric field profile for the detector with electron injection for bias 50 V from 100 ms to 10 s. 47
3.19 Time evolution of space charge density for the detector with electron injection for bias 50 V from 10 μs to 100 ms. 47
3.20 Time evolution of space charge density for the detector with electron injection for bias 50 V from 100 ms to 10 s. 48
3.21 Time evolution of the mean space charge density for the detector with electron injection for bias 50 V. 48
3.22 CWFs for the detector with electron injection for several DC biases. 49
3.23 Time evolution of CWFs for the detector with electron injection for bias 50 V. 49

4.1 Scheme of the L-TCT setup. 51
4.2 Scheme of the bias pulsing 51
4.3 Scheme of the setup for radiation spectra measurement [90]. . . . 52

5.1 Bias dependence of electron current waveforms measured by the L-TCT at pulsed bias according the scheme in figure 4.2. Dashed lines represent the MC fit with the model of the constant internal electric field. 54
5.2 Bias dependence of electron current waveforms measured by the L-TCT at pulsed bias and normalized by corresponding bias. Dashed lines represent the MC fit expecting the constant internal electric field. Solid lines plot respective fits after convolution with the function g defined in equation (5.1). 55
5.3 Bias dependence of normalized electron current waveforms measured by the L-TCT at pulsed bias. Dashed lines represent the MC fit expecting the constant internal electric field. 57
5.4 Electron current waveforms measured by the L-TCT at DC bias. Dashed lines represent the MC fit calculated according the model defined in subsection 5.1.2 60
5.5 Pulsed bias dependence of the electron CWFs. The dashed lines represent the MC fit. 60

5.6 Electron CWF dependence on the laser pulse delay for 10 V and 20 V measured by the L-TCT at pulsed and DC bias. Arrows show the direction of the waveform evolution. 61
5.7 Electron CWF dependence on the laser pulse delay for 20 V measured by the L-TCT at pulsed and DC bias. Dashed lines represent the MC fit calculated according the model defined in the subsection 5.1.2. Solid lines plot respective fits after convolution with the function g defined in equation (5.1). The internal electric field profile in the detector is presented in the inset, where arrows show the direction of the electric field evolution. 62
5.8 Bias dependence of the internal electric field profile at the DC bias. Dashed line shows the profile of fitted conductivity. 62
5.9 Bias dependence of the space charge density profile at the DC bias. 63
5.10 Bias dependence of the collected charge evaluated by the time-integration of CWFs at the pulse and DC bias conditions. 63
5.11 X-ray spectrum (red) with attenuation coefficient in CdZnTe (inset). 67
5.12 Schematic view of the electric field distribution in a detector with a positive space charge. 67
5.13 Measured electric field profiles in a 2-mm-thick CZT sensor; solid lines represent electric field with no incoming X-ray (dark mode), dashed lines are for X-ray 16 Mcps/mm^2, dotted lines are for X-ray 80 Mcps/mm^2, blue, red, and green color mark 300 V, 500 V, and 700 V bias, respectively. 71
5.14 Numerical simulation of field profiles in a 2-mm-thick CZT sensor; solid lines represent electric field with no incoming X-ray (dark mode), dashed lines are for X-ray 16 Mcps/mm^2, dotted lines are for X-ray 80 Mcps/mm^2, blue, red, and green color mark 300 V, 500 V, and 700 V bias, respectively. 71
5.15 Profile of X-ray excitation, which shows dominant excitation under cathode with fast decrease toward anode. Weighting field was calculated according [67] in the middle of the pixel with 330 μm pitch. 72
5.16 Scheme of energy levels with parameters determined by the fit of electric field. Hole trap is red; electron trap is blue. 72
5.17 Calculated space charge density from the numerical simulation. In the dark regime, there is no space charge in the sample. 73
5.18 Measured counts in 2-mm-thick CZT sensor under X-ray conditions with a count rate of 20 Mcps/mm^2 for a typical pixel. Procedure to extract critical bias U_c is shown at the intersection of linear fit for bias $U < U_c$ with the horizontal line at maximum CCE. 74
5.19 Distribution of U_c values for all pixels. 74
5.20 Simulated current waveforms for different biases and 20 Mcps/mm^2 X-ray. 75
5.21 Comparison of the collected charge of X-ray photon absorbed near the cathode (red), and deep inside the detector, 1.44 mm (blue). $U = 300$ V. 76

5.22 X-ray spectrum simulated for common parameters characterizing the electronic circuit, $t_s = 16$ ns (blue). The original X-ray spectrum is plotted for comparison (red). 76
5.23 Analysis of sampled charge depending on photon energy. In case (A), the photon energy is lower than the threshold and the charge is not detected. In case (B, C), the threshold is triggered and the charge is sampled. 78
5.24 Dependence of the collected charge on the excited charge by X-ray photon absorbed near the cathode (blue) compared with the ideal full collection plotted with a straight line (red). Labels point to the threshold levels shown in figure 5.23. 78
5.25 X-ray spectrum simulated for extended $t_s = 32$ ns (blue). The original X-ray spectrum is plotted for comparison (red). 79
5.26 Pulsed bias dependence of the electron CWFs. The dashed lines represent the MC fit. 81
5.27 Pulsed bias dependence of the electron CWFs normalized by respective bias. 82
5.28 Pulsed bias dependence of the hole current waveforms. The dashed lines represent the MC fit. 83
5.29 Pulsed bias dependence of the hole CWFs normalized by respective bias. 84
5.30 DC bias dependence of the electron current waveforms. Inset shows respective electric field profiles. The dashed lines plot the MC fit. 85
5.31 Evolution of the electron current waveforms at a pulsed bias of -400 V (arrows show the direction of the electric field evolution) depending on LPD. Inset represents the evolution of the electric field profile within the detector at several different values for the LPD. The dashed lines plot the MC fit. 86
5.32 DC bias dependence of the measured hole current waveforms. Inset shows respective electric field profiles. 87
5.33 Evolution of hole current waveforms at a pulsed bias of 400 V depending on LPD. Inset represents the evolution of the electric field profile within the detector at several different values for the LPD. The dashed lines plot the MC fit. 88
5.34 Evolution of space charge density at a pulsed bias of 400 V depending on LPD. 89
5.35 Schematic of the obtained energy levels with their parameters determined by numerical simulations of L-TCT waveforms. Red: electron traps. Blue: hole traps. Red-Blue: recombination level. . 89
5.36 Pulse height spectra of α-source ^{241}Am. Inset: Bias dependence of collected charge and Hecht equation fit. 90
5.37 Decomposition of electron and hole currents into drift and diffusion components for the detector under DC bias at 200 V. The anode is on the right-hand side. 91
5.38 Profile of lifetime of electrons and holes under pulsed and DC bias 400 V. 93

5.39 Bias dependence of initial values of current waveforms of electrons and holes under pulsed bias. Solid lines represent fit using equation (3), red for electrons and blue for holes. 94

List of Tables

1.1 Properties of semiconductor materials at room temperature. [11, 29, 43, 44, 45] 7

List of Symbols and Abbreviations

Physical constants

This is a list of physical constants that are used in this thesis [122]

Symbol	Name	Value
e	elementary charge	$1.602\ 176\ 565(35) \times 10^{-19}$ C
ε_0	vacuum permittivity	$8.854\ 187\ 817 \times 10^{-12}$ F · m^{-1}
h	Planck constant	$6.626\ 069\ 57(29) \times 10^{-34}$ J · s
$\hbar$	reduced Planck constant	$1.054\ 571\ 8(17) \times 10^{-34}$ J · s
k_B	Boltzmann constant	$1.380\ 6488(13) \times 10^{-23}$ J · K^{-1}
m_e	electron mass	$9.109\ 382\ 91(40) \times 10^{-31}$ kg

Abbreviations

1D .... one dimensional

α .... absorption coefficient

ASIC .... Application Specific Integrated Circuit

$\vec{B}$ .... magnetic flux density

Cd_i .... Cadmium interstitial

CdTe .... Cadmium Telluride

Cd_{Te} .... Cadmium antisite

CdZnTe/CZT ..... Cadmium Zinc Telluride

CdZnTeSe/CZTS . Cadmium Zinc Telluride Selenide

CSA .... charge sensitive amplifier

DC .... direct current

DDE .... Drift-diffusion equation

D_e .... diffusion coefficient for electrons

$\delta(x)$ .... Dirac delta function

D_h .... diffusion coefficient for hole

DLTS .... Deeplevel Transient Spectroscopy

e .... elementary charge (positive)

$\vec{\mathcal{E}}$ .... electric field intensity

E_0 .... rest energy of electron in vacuum

E_C .... energy of the conduction band edge

E_F .... Fermi level

E_{Fe} .... quasi-Fermi level for electrons

E_{Fh} .... quasi-Fermi level for holes

E_{FM} .... Fermi level of metal

E_{FS} .... Fermi level of semiconductor

E_g .... energy of the band gap

e-h pair .... electron-hole pair

ε_0 .... permittivity of vacuum

ε_r .... relative permittivity

E_t .... energy of the trap in the band-gap

E_V .... energy of the valence band edge

$\vec{F}$ .... Lorentz force

$f_n(E)$ .... Fermi-Dirac distribution for electrons

$f(\vec{r}, \vec{k}, t)$ .... distribution function

FWHM .... Full Width at Half Maximum

GaAs .... Gallium Arsenide

G_e .... electron generation rate

Ge .... Germanium

G_h .... hole generation rate

$\Theta(x)$ .... Heaviside unit step function (see its definition (2.24))

χ .... semiconductor electron affinity

$\chi_{[0,x_1]}(x)$ .... boxcar function (see its definition (2.23))

I .... electric current

I_{bb} .... interband light induced generation rate

I-V .... Current-Voltage

$\vec{j}$ .... total density of electric current

$\vec{j}_e$ .... electron current density

$\vec{j}_h$ .... hole current density

$\vec{k}$ .... momentum vector

k_B .... Boltzmann constant

L .... detector thickness

λ .... wavelength of light

LEC .... liquid encapsulated Czochralski

L-TCT .... Laser-Induced Transient Current Technique

MC .... Monte Carlo

MCA .... Multi-Channel Analyzer

m_e^* .... electron effective mass

m_h^* .... hole effective mass

μ_e .... electron drift mobility

μ_{eff} .... effective electron mobility

μ_h .... hole drift mobility

$(\mu\tau)_e$ .... electron mobility-lifetime product

$(\mu\tau)_h$ .... hole mobility-lifetime product

n .... electron concentration in the conduction band

$\mathcal{N}$ .... number of superparticles in Monte Carlo simulation

N_D^+ .... density of ionized donors

n_{00} .... equilibrium electron concentration in the conduction band

n_1 .... electron density in case of Fermi level being set to center energy E_t

N_A^- .... density of ionized acceptors

N_C .... effective density of states in the conduction band

n_i .... intrinsic carrier density

n_t .... trap occupancy

N_t .... trap concentration

n_{t00} .... equilibrium occupancy of trap level

ν_e .... electron thermal velocity

ν_h .... hole thermal velocity

N_V .... effective density of states in the valence band

p .... hole concentration in the valence band

p_{00} .... equilibrium hole concentration in the valence band

p_1 .... hole density in case of Fermi level being set to center energy E_t

ϕ .... electrostatic potential

Φ_K .... contact potential

Φ_M .... work function of metal

Φ_S .... work function of semiconductor

PL .... Photoluminescence

q .... charge of superparticle

Q .... electric charge

Q_0 .... initial photogenerated charge

$\vec{r}$ .... position vector

ρ .... space charge density

ϱ .... semiconductor resistivity

s_e .... electron surface recombination velocity

S_e .... Seebeck coefficient for electrons

s_h .... hole surface recombination velocity

S_h .... Seebeck coefficient for hole

Si .... Silicon

SI .... semiinsulating

σ .... semiconductor conductivity

σ_e .... electron capture cross-section

σ_h .... hole capture cross-section

SR .... Surface Recombination

SRH .... Shockley-Read-Hall

t .... time

$\mathcal{T}$ .... absolute temperature

τ_D .... detrapping time

τ_{DS}, τ_{DD} .... detrapping time of the shalow resp. deep trap level

τ_e .... electron lifetime

τ_h .... hole lifetime

$\langle\tau_{rel}\rangle$ .... mean value of relaxation time

τ_{rel} .... microscopic relaxation time

τ_T .... trapping time

τ_{TS}, τ_{TD} .... trapping time of the shallow resp. deep trap level

TCT .... Transient Current Technique

TOF .... time-of-flight

t_k .... time of the k-th simulation step

t_r .... transit time

U .... electric bias

U_{bb} .... net band-to-band recombination rate

U_e .... electron recombination rate

U_h .... hole recombination rate

UV .... ultraviolet

$\mathbf{V_{Ca}}$ .... Cadmium vacancy

$\vec{v_g}$ .... group velocity vector

$W(\vec{k}, \vec{k'})$ .... transition probability between the momentum states $\vec{k}$ and $\vec{k'}$

List of publications

Publications

1. J. Pipek, R. Grill, M. Betušiak, and K. Iniewski, Modelling Polarization Effects in a CdZnTe Sensor at Low Bias, Sensors (Basel) 23, 5681 (2023).

2. P. Praus, M. Betušiak, E. Belas, J. Kunc, R. Grill, M. Brynza, and J. Pipek, Charge Transport in Semi Insulating Bulk 4H-Silicon Carbide: Effect of Metallization and Wafer Homogeneity, Results Phys. 43, 106110 (2022).

3. A. Musiienko, J. Čížek, H. Elhadidy, P. Praus, K. Higgins, B. Dryzhakov, A. Kanak, F. Sureau, J. Pipek, E. Belas, M. Betušiak; M. Brynza, E. Lukosi; B. Hu, M. Ahmadi, Origin of Defects and Positron Annihilation in Hybrid and All-Inorganic Perovskites, Chem. Mater. 34, 297 (2022).

4. E. Belas, M. Betušiak, R. Grill, P. Praus, M. Brynza, J. Pipek, and P. Moravec, Space Charge Formation in the High Purity Semi-Insulating Bulk 4H–Silicon Carbide, J. Alloys Compd. 904, 164078 (2022).

5. J. Pipek, M. Betušiak, E. Belas, R. Grill, P. Praus, A. Musiienko, J. Pekarek, U. N. Roy, and R. B. James, Charge Transport and Space-Charge Formation in Cd1-xZnxTe1-ySey Radiation Detectors, Phys. Rev. Appl. 15, (2021).

6. A. Musiienko, D. R. Ceratti, J. Pipek, M. Brynza, H. Elhadidy, E. Belas, M. Betušiak, G. Delport, and P. Praus, Defects in Hybrid Perovskites: The Secret of Efficient Charge Transport, Adv. Funct. Mater. 31, 2104467 (2021).

7. A. Musiienko, J. Pipek, P. Praus, M. Brynza, E. Belas, B. Dryzhakov, M.-H. Du, M. Ahmadi, and R. Grill, Deciphering the Effect of Traps on Electronic Charge Transport Properties of Methylammonium Lead Tribromide Perovskite, Sci. Adv. 6, eabb6393 (2020).

8. E. Belas, R. Grill, J. Pipek, P. Praus, J. Bok, A. Musiienko, P. Moravec, O. Tolbanov, A. Tyazhev, and A. Zarubin, Space Charge Formation in Chromium Compensated GaAs Radiation Detectors, J. Phys. D Appl. Phys. 53, 475102 (2020).

9. J. Zázvorka, J. Pekárek, R. Grill, E. Belas, K. Ridzoňová, J. Pipek, and J. Franc, Inhomogeneous Resistivity and Its Effect on CdZnTe-Based Radiation Detectors Operating at High Radiation Fluxes, J. Phys. D Appl. Phys. 52, 325109 (2019).

10. A. Musiienko, R. Grill, J. Pekárek, E. Belas, P. Praus, J. Pipek, V. Dědič, and H. Elhadidy, Characterization of Polarizing Semiconductor Radiation Detectors by Laser-Induced Transient Currents, Appl. Phys. Lett. 111, 082103 (2017).

Comments

The list above is a summary of my publications during my studies. Publications are mainly focused on semiconductor radiation detectors. The first group consists of articles 1., 5., 9., 10., which study CdZnTe and CdZnTeSe material and its application as an X-ray or gamma-ray detector. The rest of the articles focus on the transport properties of SiC, GaAs, and Perovskites. Here, I would like to comment on my contribution to the thesis publications. I made MC simulations and data analysis for publications 1., 5., 6., 7., 9. I participated in measurements for publications 1., 4., 5., 6., 7., 9. I was the first author of articles 1. and 5., where I was responsible for simulations, data analysis, visualization, manuscript writing, correcting, and proofreading, as well as handling the revisions and re-submission of revised manuscripts up to the acceptance of the manuscripts. I made the measurements, simulations, data analysis, visualization, and participated in writing and analysis of article 8. Publications 1., 5. and 8. are part of this thesis.